MOLECULAR MECHANISMS OF $Ca_V2.2$ CALCIUM CHANNEL REGULATION

SPIRO A. MARANGOUDAKIS

B.S., NORTHEASTERN UNIVERSITY, BOSTON, MA, 2004

A DISSERTATION SUBMITTED IN PARTIAL FULFILLMENT OF THE REQUIREMENTS FOR THE DEGREE OF DOCTOR OF PHILOSOPHY IN THE DIVISION OF BIOLOGY AND MEDICINE AT BROWN UNIVERSITY

PROVIDENCE, RHODE ISLAND

MAY 2011

This dissertation by Spiro Anthony Marangoudakis is accepted in its present form by the division of Biology and Medicine, Department of Molecular Biology, Cell Biology and Biochemistry as satisfying the dissertation requirement for the degree of Doctor of Philosophy.

Date_____ _____
Dr. Diane Lipscombe, Advisor

Recommended to the Graduate Council

Date_____ _____
Dr. Jeffrey Laney, Reader

Date_____ _____
Dr. Rebecca Page, Reader

Date_____ _____
Dr. Robert Reenan, Reader (Chairman)

Date_____ _____
Dr. Katherine Roche, Outside Reader

Approved by the Graduate Council

Date_____ _____
Dr. Peter Weber,
Dean of the Graduate School

Curriculum Vitae

Spiro Anthony Marangoudakis

EDUCATION

Brown University, Providence , Rhode Island: 2005-present

PhD. Candidate: Graduate Program in Molecular Biology, Cell Biology, and Biochemistry

- Course work:
  - Biology of the Eukaryotic Cell (BIOL 205)
  - Analysis of Development (BIOL 231)
  - Topics Developmental Biology (BIOL 232)
  - Molecular Genetics (BIOL 254)
  - Topics in Biochem/Molecular Bio (BIOL 221)
  - Mechanisms of Neurological Disease (BIOL 294)
- Teaching requirement:
  - Teaching assistant for Introduction to Biochemistry (BIOL 28)
- Oral Qualifying exam: September 2007
- Written qualifying exam: November 2007
- MCB Data Club presentation(s): March 2008, March 2009

Northeastern University, Boston, Massachusetts: 2000-2004

B.S. Biology, *Summa Cum Laude*, 2004

PUBLISHED AND SUBMITTED WORKS

Marangoudakis S, Andrade A, Helton TD, Denome S, Castiglioni AJ, Lipscombe D. Ubiquitination and proteasome targeting on N-type $Ca_V2.2$ channels depends on alternative splicing. (Manuscript in revision)

Andrade A, Denome S, Jiang Y-Q, Marangoudakis S, Lipscombe D. (2010). Opioid receptor inhibition of N-type calcium channels and spinal morphine analgesia couple to cell-specific alternative splicing. *Nature Neuroscience.*Oct;13(10):1249-56.

Jakubek L, Marangoudakis S, Raingo J, Liu X, Lipscombe D, Hurt R. (2009). The inhibition of neuronal calcium ion channels by trace levels of yttrium released from carbon nanotubes. *Biomaterials*. Oct;30(31):6351-7.

Book Chapters:

Lipscombe D, Allen S, Gray AC, Marangoudakis S, Raingo J. (2009). Alternative splicing of neuronal Ca_V2 calcium channels. *Structure, Function, and Modulation of Neuronal Voltage-Gated Ion Channels*. Eds. Valentin K. Gribkoff and Leonard K. Kaczmarek (Wiley).

ABSTRACTS

Marangoudakis S, Helton TD, Lipscombe D. (2010). Stathmin 2 regulates N-channel surface expression through a direct protein-protein interaction. 40th Annual Society for Neuroscience conference, San Diego CA.

Marangoudakis S, Andrade A, Helton TD, Denome S, Castiglioni AJ, Lipscombe D. (2010). Isoform-specific ubiquitination of the N-type voltage-gated calcium channel. 5th International conference of SUMO, Ubiquitin, UBL proteins: Implications for Human Diseases, Houston TX.

Jiang Y-Q, Denome S, Marangoudakis S, & Lipscombe D. (2009). Alternative splicing influences N-type calcium channel up-regulation in the spinal cord following peripheral nerve injury. 39th Annual Society for Neuroscience conference, Chicago IL.

Andrade A, Denome S, Marangoudakis S, Lipscombe D. (2009). Exon-substitution in the mouse *Cacna1b* gene reveals the functional consequences of alternative splicing on N-type calcium channels in sensory neurons. 39th Annual Society for Neuroscience conference, Chicago IL.

Marangoudakis S, Helton T, Lipscombe D. (2009). Isoform-specific ubiquitination of the N-type voltage-gated calcium channel. 39th Annual Society for Neuroscience conference, Chicago IL.

Andrade A, Jiang Y-Q, Marangoudakis S, Denome S, & Lipscombe D. (2009). Genetic manipulation of N-type channel isoforms in the pain pathway. Keystone Pain Symposium, Santa Fe, NM.

Lipscombe D, Denome S, Andrade A, Jiang Y-Q, & Marangoudakis S. (2009). Nociceptors Modulate Calcium Channel Activity by Alternative Splicing. Keystone Pain Symposium, Santa Fe, NM.

Lipscombe D, Jakubek LM, Marangoudakis S, Raingo J. & Hurt R. (2008). Single walled carbon nanotubes disable neuronal calcium ion channels through yttrium release. 38th Annual Society for Neuroscience Conference, Washington DC. (Featured in *Nature* News under “Jakubek”)

Marangoudakis S, Lipscombe D. (2008). Novel protein-protein interactions in the tail of the N channel. 38th Annual Society for Neuroscience Conference, Washington DC.

Raingo J, Marangoudakis S, Denome S, Lipscombe D. (2006). Alternative splicing controls voltage-independent inhibition on N-type calcium channels in nociceptors. 36th Annual Society for Neuroscience Conference, Atlanta GA.

HONORS AND AWARDS

NIH NRSA F31 individual predoctoral grant: Isoform specific ubiquitination of the N-type calcium channel (1F31NS066702), 2009
June Rockwell Levy Foundation (travel grant): Supported collaboration with Jon-Paul Bingham Ph.D., University of Hawaii, Manoa, 2009
John G. Peterson Fellowship; Brown University, 2010

OTHER RESEARCH EXPERIENCE

Research Assistant (full-time position) **Sept 2004 - Jul 2005**
One Cell systems, Inc., Cambridge, Massachusetts
Supervisor: Yevgenya Akselband, MD, PhD
Utilized gel micro-drop technology to study human stem cell differentiation

Research Assistant (full-time internship) **Jun 2003 - Dec 2003**
One Cell systems, Inc., Cambridge, Massachusetts
Supervisor: Yevgenya Akselband, MD, PhD
Gel micro-drop single-cell isolation product design and optimization

Research Assistant (full-time internship) **Jun 2002 - Dec 2002**
Millennium Pharmaceuticals, Cambridge, Massachusetts
Supervisor: John Monahan
Alternative splicing research/genetic disease marker validation

Technician (part-time internship) **2000 - 2004**
Northeastern University, Boston, Massachusetts
Electron Microscopy Center
Supervisor: William Fowle
Sample preparation, image analysis, operation of Scanning EM

ADDITIONAL TEACHING/TRAINING

Trainer of several graduate and undergraduate students
Graduate:
- Kristen Pizarro, Neuroscience, 2006

Undergraduate:
- Lamia Khan, 2006
- Stephen Alderhand, 2006
- Jake Kline, 2009
- Andrew Hwang, 2009

PROFESSIONAL AFFILIATIONS

Society for Neuroscience (SfN)
Sigma Xi Scientific Research Society

COLLABORATIONS FORMED/MAINTAINED

Jon-Paul Bingham, PhD., University of Hawaii, Manoa
Robert Hurt, PhD., Brown University, Department of Engineering
Stephen Ikeda, PhD., National Institutes of Health, NIAAA

OTHER RESPONSIBILITIES

Sole webmaster, caretaker, and updater of the Lipscombe Lab website, 2006 - 2011 (http://neuroscience.brown.edu/LipscombeLab/Index.html)

To my parents, Anthony and Niki Marangoudakis.
For having stood by me from the very beginning

Acknowledgements

Dr. Diane Lipscombe, my advisor and mentor, deserves a lot of my praise. I cannot say enough about Diane's intellect, instincts, charm, and all around positive attitude. I always felt welcome to discuss anything that was on my mind, and I was always met with a constant smile and pleasant temperament. My thesis committee: Dr. Robert Reenan, Dr. Jeffrey Laney, Dr. Rebecca Page, and Dr. Katherine Roche, also deserve my thanks. They were always available to answer a question, or for a discussion, and their advice was always spot-on. I would also like to thank a couple members specifically for helping me with some very tight grant application deadlines. Thank you.

I want to thank the past and present members of our laboratory: Sylvia Denome, Arturo Andrade, Cecilia Phillips, Summer Allen, Yu-Qui "Rachel" Jiang, Thomas Helton, Jesica Raingo, Galina Karashchuk, Annette "Nina" Gray, Andrew Castiglioni, as well as visiting scholar Celio Junior, for their ebullient discussions.

I would also like to specifically thank Jesica Raingo for teaching me how to expertly patch clamp while she was *extremely* pregnant. I greatly appreciate the help.

I also must thank Andrew Castiglioni for having beautifully prepared and performed the yeast two-hybrid screen, from which a major project described in this thesis evolved. His attention to detail is unmatched.

My thanks would also be incomplete without thanking Sylvia Denome for making sure that our lab is always running at optimum efficiency, which in-fact was a consideration when I was deciding on a lab to join. A well put-together lab can say a lot about the quality of the people and science within.

I would like to thank my family, including my mother and Father, Niki and Anthony Marangoudakis, as well as my sister and brother, Chrisoula and George. I am also greatly appreciative of my extended family, and my friends whom have been completely supportive since day one.

Last but definitely not least, The National Institutes of Health (NIH) and all the people in our country who have supported its mission and the mission of scientific discovery in general, deserve my thanks. With this support, we as a people are at the forefront of innovation, and our country is a brilliant example of what an enlightened people are capable of.

Preface

$Ca_V2.2$ calcium channels are gatekeepers of cellular calcium entry in neurons and couple electrical excitation to neurotransmitter release. Proper function of these proteins is critical in transducing the signals that support neuronal communication. Many endogenous and exogenous agents inhibit $Ca_V2.2$ channels, leading to abrogation of neuronal signaling. In this thesis I discuss multiple inhibitory events that converge on the $Ca_V2.2$ channel and explore powerful cellular mechanisms that involve pre-mRNA alternative splicing at the e37a and e37b locus. The first project details how alternative splicing and ubiquitination converge on the $Ca_V2.2$ channel to control its activity (Chapter 2). Our work shows that cells control ubiquitin-mediated degradation of $Ca_V2.2$ calcium channels by alternative splicing of mutually exclusive exons e37a and e37b. In the subsequent chapter (Chapter 3) we show how this same site of alternative splicing also regulates inhibition of $Ca_V2.2$ channels mediated through μ-opioid receptors in neurons. I collaborated on this project to determine how altering splicing at e37a/e37b in the mouse gene coding $Ca_V2.2$ (*Cacna1b*) impacts protein expression levels in mouse brains and dorsal root ganglia (Andrade et al., 2010). This work extends from studies performed *in vitro* that showed alternative splicing affects channel inhibition by G proteins (Raingo et al., 2007). In Chapter 4 I highlight how the $Ca_V2.2$ calcium channel can be used as a biosensor to detect contaminants in carbon nanotubes- materials being used in various biological applications. In the final section (Chapter 5) I explore possible cross-talk among cellular mechanisms used to regulate $Ca_V2.2$ channel expression, discuss alternative explanations for our results, and present ideas for more effective therapeutics targeting $Ca_V2.2$.

Table of Contents

CHAPTER 1: INTRODUCTION

CHAPTER 2: N-type $Ca_V2.2$ Channel Ubiquitination and Proteasome Sensitivity Depends on Alternative Splicing

CHAPTER 3: Novel $Ca_V2.2$ Knock-in Mice Reveal Isoform-specific Response to Morphine

CHAPTER 4: The Inhibition of Neuronal Calcium Ion Channels by Trace levels of Yttrium Released from Carbon Nanotubes

CHAPTER 5: DISCUSSION

List of Figures

Figures in Appendix

List of Tables

CHAPTER 1

INTRODUCTION

Part of this thesis chapter (Figure 1.4) has been published in the book chapter: Diane Lipscombe, Summer E. Allen, Annette C. Gray, **Spiro Marangoudakis**, and Jesica Raingo (2009) Alternative splicing of neuronal Ca_V2 calcium channels. *Structure, Function and Modulation of Neuronal Voltage-Gated Ion Channels*. Eds: Leonard K. Kaczmarek and Valentin K. Gribkoff. ISBN: 978-0-471-93013-6, 475 pages. (Wiley)

Voltage-gated Calcium Channels

Voltage-gated calcium channels (VGCCs) are expressed in excitable cells throughout the body. These channels are composed of a central pore-forming subunit ($Ca_V\alpha_1$), as well as accessory proteins $Ca_V\alpha_2\delta$ and $Ca_V\beta$ (and sometimes $Ca_V\gamma$) that affect the biophysics, stability and surface expression of the $Ca_V\alpha_1$ subunit (Figure 1.1A) (Hille, 2001; Dolphin, 2009). Each channel is composed of four highly homologous domains (I-IV), and within each domain there are six transmembrane segments (S1-S6) (Figure 1.1B) (Hille, 2001). Under resting conditions VGCCs are mostly in the closed state. However, when the cell's plasma membrane is depolarized sufficiently, the open probability of VGCCs increases, allowing calcium flux into the cell. There are four voltage sensors contained mostly in the S4 transmembrane helices of each domain that detect small changes in membrane potential (Figure 1.1B). Each S4 has a high content of positively charged amino acids, composed of arginine and lysine residues. The S4 helices are thought to move outward upon depolarization, leading to conformational changes that mediate channel opening (Aggarwal and MacKinnon, 1996; Hille, 2001). In addition, the P-loop structure between S5 and S6 is thought to form the ion-selective pore of the channel (Tedford and Zamponi, 2006). The large intracellular N and C-termini, as well as the intracellular linkers connecting the domains (I-II, II-III, III-IV linkers) mediate much of the modulation to the channel through post-translational modifications and protein-protein interactions. These interactions are discussed later on in this chapter. This thesis describes three projects which concern modulation of calcium channels through the interaction of various protein or ion molecules with the channel.

Voltage-gated calcium channel diversity

A multitude of channel subunits support VGCC diversity. There are four proteins that comprise both $Ca_V\alpha_2\delta$ and $Ca_V\beta$ ($Ca_V\alpha_2\delta_1$ - $Ca_V\alpha_2\delta_4$ and $Ca_V\beta_1$- $Ca_V\beta_4$, respectively), and ten $Ca_V\alpha_1$ pore-forming subunits, grouped into three families (Tedford and Zamponi, 2006). These include the Ca_V1 family ($Ca_V1.1$-$Ca_V1.4$), the Ca_V2 family ($Ca_V2.1$-$Ca_V2.3$), and the Ca_V3 family of VGCCs ($Ca_V3.1$-$Ca_V3.3$) (Ertel et al., 2000). Ca_V2 channels are expressed in neurons and are mostly found presynaptically (Figure 1.2). These channels are responsible for mediating neurotransmitter release from presynaptic nerve terminals in response to membrane depolarization (Hille, 2001). Ca_V2 channels, and some Ca_V1 channels ($Ca_V1.2$) are high-voltage-activated (HVA) and require strong depolarization for activation (Hille, 2001). Other Ca_V1 channels, including $Ca_V1.3$ and possibly $Ca_V1.4$ are opened by intermediate size depolarizations (Xu and Lipscombe, 2001). Members of the Ca_V3 family are generally low-voltage-activated (LVA) and are found in pacemaking cells in the body. Pharmacology can also vary by channel family. Members of the Ca_V2 family are resistant to the classical blocker used to identify Ca_V1 family channels (1,4-dihydropyridine, DHP) and are specifically inhibited by several natural toxins and other molecules which allowed for their early characterization (Hille, 2001). In this thesis I focus on the Ca_V2 family.

The Ca_V2 family of VGCCs

$Ca_V2.1$ channels underlie P-type and Q-type components of neuronal currents. These channels were originally named P-type because of their predominant expression in

Purkinje neurons (Llinas et al., 1989; Stanley and Atrakchi, 1990; Hillman et al., 1991). The P current was isolated by omega-agatoxin GIVA, a channel blocking toxin produced by the funnel web spider *Agelenopsis aperta* (Mintz et al., 1992). Q-type currents were defined based on their lower sensitivity to agatoxin. At the time it was not known that P-type and Q-type currents were products of the same gene (Randall and Tsien, 1995). It is now generally accepted that P-type and Q-type currents arise from the *Cacna1a* gene, and result from alternative splicing, and/or association with different $Ca_V\beta$ subunits (Sather et al., 1993; Stea et al., 1994; Randall and Tsien, 1995; Bourinet et al., 1999; Richards et al., 2007). However, the precise molecular composition of P-type and Q-type currents is still not completely resolved (Lorenzon et al., 1998; Richards et al., 2007).

$Ca_V2.2$ proteins are products of the *Cacna1b* gene, and underlie the N-type component of VGCC currents. These currents and channels were given the name N-type because it was the next available letter in the alphabet after “L”, which was used to describe the first Ca_V1 channel (“L-type”; “M-type” was used to refer to a particular class of potassium channel; D.L. *pers. communication*). (Nowycky et al., 1985; McCleskey et al., 1987; Ertel et al., 2000; Hille, 2001; Barton, 2007). $Ca_V2.2$ channels are efficiently and specifically blocked by toxins produced by at least two species of marine snails in the genus *Conus* (conotoxin MVIIA, *Conus magus*; conotoxin GVIA, *Conus geographus*). These toxins were used to initially isolate and characterize N-type currents and are still used for this purpose (Nowycky et al., 1985; McCleskey et al., 1987). This thesis focuses on the regulation of $Ca_V2.2$ channels.

Finally, the least well understood member of the Ca_V2 family is $Ca_V2.3$. The $Ca_V2.3$ pore forming subunits are products of the *Cacna1e* gene, and are responsible for R-type calcium currents. R-type refers to the "residual" current that is resistant to L-type channel blockers (DHP) and N and P/Q-type channel blocking toxins (Randall and Tsien, 1995). These channels are found in neurons, and although their tissue distribution is not fully mapped, they are known to express in trigeminal ganglion neurons and the cerebellum (Fang et al., 2007).

N-type currents and $Ca_V2.2$ channels

$Ca_V2.2$ calcium channels are enriched at presynaptic nerve terminals and thus their main and best-understood function is to couple electrical excitation to neurotransmitter release (Figure 1.2) (Dunlap et al., 1995). Several groups have found evidence that N-type currents regulate additional cellular functions such as synaptogenesis and gene regulation (Brosenitsch and Katz, 2001; Jones et al., 2001). $Ca_V2.2$ channels are found in most neurons. In some regions of the nervous system, such as dorsal root ganglia (DRG), they make up a majority of the VGCCs (Tedford and Zamponi, 2006).

The human *Cacna1b* gene encoding $Ca_V2.2$ is located at chromosomal position 9q34 and spans ~250 kb in the human genome (Lipscombe and Castiglioni, 2004). This gene contains at least 50 known exons (Figure 1.3) (Lipscombe and Castiglioni, 2004). Several of these exons can be alternatively spliced and the most abundant isoforms are coded by transcripts of ~7,000 nucleotides (Figure 1.3). The resultant proteins are ~260

kDa; their large size makes detailed biochemical studies of $Ca_V2.2$ challenging. Thus, compared to other membrane proteins, including neurotransmitter receptors, we know far less about the biochemical properties of VGCCs in general, and of $Ca_V2.2$ specifically.

As with other VGCCs, $Ca_V2.2$ proteins contain large intracellular linker domains - the largest being the II-III linker. Synaptic and SNARE proteins, which are involved in synaptic vesicle exocytosis, interact with $Ca_V2.2$ channels via the II-III linker in a region termed the synprint (synaptic protein interaction) site (Figure 1.4) (Sheng et al., 1994; Hille, 2001). The intracellular N- and C-termini of $Ca_V2.2$ proteins are also large and support many protein-protein interactions important for channel regulation. Collectively, the N- and C- termini, along with the II-III linker support ~ 90% of the known protein-protein interactions that mediate channel function and alter channel gating and trafficking (Figure 1.4) (Lipscombe et al., 2009). The remaining known interactions are mediated via the I-II linker that binds $Ca_V\beta$ subunits, amongst other partners. Protein interactions with the II-III linker and the C-terminus can be altered by alternative splicing (Figure 1.4). In Chapters 2 and 3 I present data obtained by myself and in collaboration with other lab members, that splice isoforms of $Ca_V2.2$ with differing C-termini are differentially regulated by both G proteins and ubiquitin.

Alternative splicing

After transcription, the precursor messenger RNA (pre-mRNA) transcript contains both protein-coding sequences (exons), and non-coding sequences (introns). During pre-

mRNA processing, introns are removed from the transcript through a process termed "splicing". This occurs before mRNA transcripts are exported from the nucleus. During this process a group of small nuclear RNA proteins (snRPS) form a "spliceosome" complex at specific intronic sites. These sites are determined by *gt* and *ag* dinucleotide sequences found at the 5' and 3' boundaries of introns, respectively (Modrek and Lee, 2002). Splicing is also orchestrated by a central branch point containing an adenine (Modrek and Lee, 2002). These *cis* elements are critical for efficient and effective discrimination of introns and for their removal by the spliceosome complex (Wahl et al., 2009). Occlusion and enhancement of these sites is mediated by RNA binding protein *trans* (splicing) factors which can precipitate exon skipping or exon inclusion, as well as various other effects during pre-mRNA splicing (Wahl et al., 2009). These mechanisms underlie alternative splicing.

Alternative pre-mRNA splicing allows higher organisms to overcome the G-value paradox, which is that higher and lower organisms contain a similar number of protein-coding genes despite their vastly different complexity (Taft et al., 2007). Alternative splicing increases the flexibility of the genome by allowing individual protein coding transcripts to be altered without changing the largely immutable DNA genome of the organism (Taft et al., 2007). Prokaryotes such as bacteria and Achaea do not support alternative splicing, while lower eukaryotes such as yeast support greatly reduced alternative splicing compared to metazoans (Kondrashov and Koonin, 2003; Barton, 2007). The degree of alternative splicing correlates with the size of transcriptomes and proteomes (Taft et al., 2007). In higher organisms alternative splicing is extensive.

Current estimates suggest 95% of all multi-exon human transcripts are alternatively spliced (Calarco et al., 2009).

Alternative splicing in the nervous system

Alternative splicing is extensive in the nervous system of higher order species (Jensen et al., 2000; Lipscombe, 2005; Lin et al., 2010). In the nervous system, alternative splicing provides cells the ability to fine-tune their operating parameters (Jensen et al., 2000; Lipscombe, 2005). One of the most widely cited examples of neuronal alternative splicing involves the Down syndrome cell adhesion molecule gene (*Dscam*). Alternative splicing of this gene's transcripts is especially extensive (Hattori et al., 2008). The *Drosophila Dscam* gene is most often cited due to its potential to form 38,016 splice isoforms (Lee et al., 2010), and *Dscam* is found in both lower and higher organisms, including humans (Hattori et al., 2008; Amano et al., 2009; Shen et al., 2011). DSCAM splice isoforms determine neural wiring specificity through homophilic binding (Hattori et al., 2008). This process involves specific DSCAM protein isoforms binding to other complementary isoforms to form homodimers. This gives neurons the ability to recognize self axonal and dendritic branches from non-self branches during development (Hattori et al., 2008). This mechanism of self and non-self recognition is critical for neuronal self-avoidance, to maximize the receptive field of each neuron. Mice lacking *Dscam* die perinatally (<24hr after birth) due to loss of neuronal synchronicity (Amano et al., 2009).

Alternative splicing is thought to be critical for the acquisition of neuronal identity during cell differentiation. Alternative splicing is essential for the switch from non-neuronal to neuronal state. For example, when the splicing repressor protein (PTBP1, PTB) is expressed, it inhibits the acquisition of neuronal identity. Alternatively, its absence can trigger upregulation of the neuronal form of the PTB protein, nPTB (PTBP2) and a subsequent increase in neuronal-specific alternative splicing (Fairbrother and Lipscombe, 2008). Interestingly, work by three groups (led by Tom Maniatis, Douglas Black, and Christopher Smith) discovered that PTB binds to and regulates alternative splicing of nPTB (Boutz et al., 2007; Makeyev et al., 2007; Spellman et al., 2007; Fairbrother and Lipscombe, 2008). In this process, PTB represses the inclusion of exon 10 in nPTB mRNA. Inclusion of exon 10 is critical for the formation of a functional protein, and its loss leads to a frame-shift in the message, and nonsense mediated decay (NMD) of nPTB mRNA (Makeyev et al., 2007). PTB levels are kept low in neurons by a neuronal-specific micro RNA (miR-124) which binds to and downregulates PTB mRNAs (Makeyev et al., 2007). Thus, the splicing of nPTB is a strong example of how cell-specific isoform expression can affect important cellular processes.

Alternative splicing of ion channels

One of the most important determinants of neuronal function is set by the milieu of plasma membrane ion channels. Channels set the resting membrane potential and control neuronal excitability (Hille, 2001). Alternative splicing is known to add, remove, and alter channel motifs. These structural changes alter channel biophysical properties, affect protein-protein interactions, and regulate post-translational modifications, among

other effects (Lipscombe et al., 2002; Soong et al., 2002; Lipscombe and Castiglioni, 2004; Lipscombe, 2005; Adams et al., 2009). Various types of RNA processing that impact channel function have been documented including, cassette exon insertion/skipping, alternate use of splicing donor/acceptor sites, alternative polyadenylation, and RNA editing.

A classic case of alternative splicing-induced regulation of ion channel function is evident in the calcium-activated potassium channels (*slo*), in chicken auditory cells. Alternative splicing in these channels fine-tunes cellular frequency sensitivity (Fettiplace and Fuchs, 1999; Jones et al., 1999). Analysis of splice isoforms of *slo* along the auditory epithelium shows a graded expression pattern (Fettiplace and Fuchs, 1999; Frucht et al., 2011). Alternative splicing of *slo* is also influenced by membrane depolarization, and thus alternative splicing both influences and responds to cellular stimuli (Xie and Black, 2001). Other channel genes that generate functionally different alternative splice isoforms include K_V3.4, and the NMDA receptor. The K_V3.4a isoform is expressed in fast spiking neurons throughout the body (Baranauskas et al., 2003), and different isoforms of the NMDA receptor regulate neuronal synaptic strength (Mu et al., 2003). $Ca_V\alpha_1$ genes are large and complex, thus it is not surprising that all ten $Ca_V\alpha_1$ genes, and all accessory subunit genes ($Ca_V\alpha_2\delta$ and $Ca_V\beta$), contain several sites of alternative splicing (Lipscombe, 2005). If we assume that each site of alternative splicing is independently regulated, each $Ca_V\alpha_1$ gene has the capacity to generate hundreds, perhaps thousands, of splice isoforms (Lipscombe et al., 2002).

Alternative splicing of $Ca_V2.2$

Our lab and others have studied and described several distinct types of $Ca_V2.2$ pre-mRNA alternative splicing and RNA processing events. These events can involve the inclusion or exclusion of alternative (cassette) exons, alternative 3' splice site acceptor usage, mutually exclusive exon splicing, and alternative polyadenylation (Lin et al., 1997; Schorge et al., 1999; Kaneko et al., 2002; Lipscombe et al., 2002; Maximov and Bezprozvanny, 2002; Lipscombe and Castiglioni, 2004) (Figure 1.5). Of the known splicing events in $Ca_V2.2$, exon inclusion/exclusion is most common (Figure 1.3). Exons 18a, 20, 20a, 24a and 31a were identified in our lab as well as by others to act as cassette exons in the *Cacna1b* gene (Lipscombe et al., 2002; Lipscombe and Castiglioni, 2004).

Exon 18a was identified in rat (Ghasemzadeh et al., 1999; Pan and Lipscombe, 2000), and found to code for a 21 amino acid insertion (FVKQTRGTVSRSSSVSSVNSP). E18a is expressed in peripheral ganglia spinal cord, and midbrain regions, and is less prevalent in adult cortex, hippocampus, and cerebellum (Pan and Lipscombe, 2000). E18a is up-regulated during development and its inclusion protects the channel from cumulative closed-state inactivation (Pan and Lipscombe, 2000; Thaler et al., 2004). The high serine content of e18a suggests that it may be a substrate for protein phosphorylation.

Exon 31a encodes a dipeptide sequence (glutamate-threonine; ET) in the IV S3-S4 extracellular linker of $Ca_V2.2$ channels, in close proximity to the S4 voltage sensor of

domain IV. E31a slows channel activation and deactivation (Lin et al., 1997; Lin et al., 2004; Lipscombe and Castiglioni, 2004). Steric hindrance appears to be the way e31a influences channel gating because a somewhat different (asparagine-proline; NP) dipeptide inserted into the same region of $Ca_V2.1$ channels leads to a similar slowing of channel gating (Lin et al., 1999). Exon 24a has a smaller effect on channel gating and is expressed in the homologous S3-S4 region of domain III in $Ca_V2.2$. It encodes the tetrapeptide sequence (SFMG), and its effects are similar to that of e31 (Figure 1.3).

I identified the alternative exon 20a. This exon lies between exons 20 and 21, and it had not been previously documented. Its insertion would lead to severely truncated and likely non-functional $Ca_V2.2$ channels (Figure 1.5). This truncation occurs because e20a codes an in-frame stop in its last codon (HLKKTCASSESMVSDEKSTVTRNVLFL*; rat, acc# FJ431206). If this exon is translated, the resulting protein would be a hemichannel containing only the first two domains of the $Ca_V2.2$ protein, although we predict that the mRNA may most likely be subject to nonsense mediated decay (Figure 1.3, 1.5) (Chang et al., 2007).

Curiously, another group proposed the presence of a novel splice isoform of $Ca_V2.2$ that would produce a channel that is very similar to the protein predicted from $Ca_V2.2$ mRNA containing exon 20a (Raghib et al., 2001; Page et al., 2004). However, this group did not discern the mechanism of splicing or the presence of a corresponding $Ca_V2.2$ mRNA isoform (Raghib et al., 2001). Dolphin and colleagues showed that expressing a $Ca_V2.2$ hemichannel in a heterologous expression system induces the unfolded protein

response (UPR), including the protein kinase RNA-like endoplasmic reticulum kinase (PERK) pathway (Page et al., 2004). Studies of this UPR-dependent response were carried out in a variety of overexpression systems. We do not know if a similar cellular mechanism regulates expression of hemi-$Ca_V2.2$ protein containing e20a in neurons. We assume that the putative hemichannel of $Ca_V2.2$ produced by e20a-containing transcripts are at relatively low levels due to the presumed instability of the mRNA. At least one other example of a two domain VGCC hemichannel exists. The hemichannel protein is derived from the *Cacna1a* ($Ca_V2.1$) gene (Scott et al., 1998; Arikkath et al., 2002). The hemi-$Ca_V2.1$ protein is not generated by a homologue of e20a, but the similarity between hemichannels of $Ca_V2.1$ and $Ca_V2.2$ may indicate conserved physiological importance.

In addition to exon inclusion/exclusion, alternative splicing of $Ca_V2.2$ pre-mRNAs also involves the use of alternative 3' splice acceptor sites; e10 and e19 into e^a10 and e^a19. At both sites, alternative splicing leads to inclusion of a single codon which adds or removes one amino acid (Figure 1.3, 1.5).

$Ca_V2.2$ mRNAs containing different C-termini have also been identified (Maximov and Bezprozvanny, 2002). An isoform lacking part of the distal region of the C-terminus, normally containing a proline rich and SH3 binding domain, leads to diffuse targeting of $Ca_V2.2$ channels relative to those with a complete, normal length C-terminus. The differential expression pattern of these C-terminal isoforms of $Ca_V2.2$ depends on protein-protein interactions and is detailed in Figure 1.4 (Maximov and Bezprozvanny,

2002). Our group has also shown that alternative polyadenylation in the 3' UTR of $Ca_V2.2$ mRNAs can influence mRNA stability (Figure 1.3, 1.5) (Schorge et al., 1999). In our studies a "long" form of the transcript was discovered with an extended 3' UTR (2.5 kb). This long $Ca_V2.2$ mRNA showed enhanced degradation when compared to the shorter form that contained a 3' UTR of 192 nucleotides (Schorge et al., 1999).

Much of my work has focused on a very interesting site of mutually exclusive splicing that generates $Ca_V2.2$ protein isoforms with different C-termini. Mutually exclusive exons 37a and 37b in the *Cacna1b* gene encode short stretches of protein sequence that differ by 14 amino acids (Figure 1.3, 1.5, 1.6). This region of sequence variation is in the proximal C-terminal region, close to the final transmembrane domain. I show in this thesis that this site of alternative splicing significantly effects channel function, channel surface expression, as well as channel post-translation modifications.

$Ca_V2.2$ exons 37a and 37b

Prior to the discovery of e37a, all $Ca_V2.2$ mRNA-derived sequences isolated from mammalian brain contained e37b. However, using *in silico* genome analysis, Qian "Jen" Pan, a former graduate student in our lab discovered that *Cacna1b* genes of mouse and human contained a second sequence that was highly homologous to, but different from e37b, between e36 and e37b (Figure 1.6). Subsequently, Andrew Castiglioni and Thomas Bell, also former graduate students in the lab, identified $Ca_V2.2$ cDNAs from rat dorsal root ganglia (DRG) that contained both e37a and e37b sequences (Bell et al., 2004). By single cell RT-PCR they showed that e37a sequences were particularly

enriched in nociceptors of DRG, and in subsequent experiments showed that e37a mRNAs are expressed at low levels in the brain (Bell et al., 2004; Castiglioni et al., 2006).

The functional differences between e37a- and e37b-containing $Ca_V2.2$ channels ($Ca_V2.2e[37a]$ and $Ca_V2.2e[37b]$ respectively) were initially discovered in heterologous expression systems. Using embryonic kidney (HEK)-derived tsA201 cells and *Xenopus* oocytes, we showed that despite their similar unitary conductances of ~21 pS, $Ca_V2.2e[37a]$ and $Ca_V2.2e[37b]$ channels have different gating kinetics (Castiglioni et al., 2006). $Ca_V2.2e[37a]$ channels close and inactivate more slowly than $Ca_V2.2e[37b]$ channels (Castiglioni et al., 2006). One of the most striking differences between e37a and e37b channels, however, was a consistent difference in current densities; calcium currents in cells expressing $Ca_V2.2e[37a]$ channels were 60 percent larger compared to $Ca_V2.2e[37b]$ channels (Bell et al., 2004; Castiglioni et al., 2006). Gating currents were correspondingly larger in cells expressing $Ca_V2.2e[37a]$, suggesting that the larger current density associated with $Ca_V2.2e[37a]$ channels reflects greater cell surface expression (Castiglioni et al., 2006). Gating currents result from the outward movement of positively charged amino acids within voltage sensors in the S4 domains relative to the rest of the channel protein (Figure 1.1B). The size of the gating charge is proportional to the number of functional channels of the cell surface. In addition, our lab discovered that $Ca_V2.2e[37a]$ channels are more sensitive to inhibition by G proteins compared to $Ca_V2.2e[37b]$ channels (Raingo et al., 2007).

Regulation of $Ca_V2.2$ channels by G proteins

G proteins form a heterotrimeric complex composed of Gα, Gβ and Gγ proteins. 16 different genes encode Gα proteins (Tedford and Zamponi, 2006). Each contains a GTP binding site, and intrinsic GTPase activity. Gβ and Gγ components are composed of five and 12 subtypes, respectively (Tedford and Zamponi, 2006). The diversity of G proteins allows them to mediate a wide variety of downstream biological effects on a variety of targets. Upon activation of G protein coupled receptors (GPCRs), the Gαβγ complex interacts with the receptor and exchanges GDP for GTP. This triggers dissociation of the trimetric G protein complex into Gα and a Gβγ dimer (Tedford and Zamponi, 2006). Both Gα and Gβγ mediate downstream effects on substrates, including calcium channels (Dolphin, 2003b; Tedford and Zamponi, 2006). The intrinsic GTPase activity of Gα hydrolyzes the bound GTP to GDP which increases its affinity for the free Gβγ dimer, effectively quenching activation (Tedford and Zamponi, 2006). Several labs have shown that G proteins can inhibit VGCCs, specifically presynaptic Ca_V2 channels (Dunlap and Fischbach, 1978; Lipscombe et al., 1989; Dolphin, 2003b).

Neurons use GPCRs as a way to inhibit Ca_V2 channels. Many presynaptic GPCRs are activated by neurotransmitters released following presynaptic VGCC activation. This negative feedback mechanism appears to be designed to blunt calcium entry into presynaptic nerve terminals and to thus downregulate transmitter release after depolarization (Dolphin, 2003b; Tedford and Zamponi, 2006). Several dozen GPCRs inhibit presynaptic calcium channel function, with most known receptors targeting

$Ca_V2.2$ and $Ca_V2.1$ channels (Dolphin, 2003b; Tedford and Zamponi, 2006). $Ca_V2.2$ inhibition is known to be mediated through several GPCRs, including: vasoactive intestinal peptide (VIP) (Zhu and Ikeda, 1994), dopamine D1 and D2 (Kisilevsky et al., 2008; Kisilevsky and Zamponi, 2008), ORL1 (Altier et al., 2006; Tedford and Zamponi, 2006), $GABA_B$ (Campbell et al., 1995), adenosine A1 (Brody and Yue, 2000), muscarinic M1 (Kammermeier et al., 2000), μ-opioid (Polo-Parada and Pilar, 1999) and neurokinin 1 receptors (Kammermeier et al., 2000). Certain receptors, including the D1 and ORL1 downregulate $Ca_V2.2$ channels by internalization (Altier et al., 2006; Kisilevsky et al., 2008) however, most appear to work by inhibiting channel gating through G proteins (Dolphin, 2003b). Typically $Ca_V2.2$ inhibition is separated into 1) voltage-dependent inhibition (VDI), that is reversed by a strong depolarization (~+80 mV) (Bean, 1989; Ikeda, 1991; Hille, 1994), and 2) voltage independent inhibition (VII), a form of inhibition that is largely intact following a strong depolarization (Diverse-Pierluissi and Dunlap, 1993). Many activated GPCRs can induce both VDI and VII pathways simultaneously (Luebke and Dunlap, 1994; Raingo et al., 2007).

VDI of $Ca_V2.2$ involves Gβγ binding to the I-II linker (Dolphin, 2003a) (Figure 1.4). In the presence of a strong depolarization, Gβγ is thought to dissociate from the $Ca_V2.2$ channel. In contrast, the mechanism of VII is less well understood, and this may be because it is not mediated by one standard mechanism. Several different signaling molecules are involved in mediating VII of $Ca_V2.2$ channels, using at least three different $G\alpha$ proteins, and depending specifically on the type of receptor being activated (Dolphin, 2003b; Tedford and Zamponi, 2006). Specifically, phosphorylation-dependent

mechanisms and internalization have been implicated as mechanisms of VII by several groups (Surmeier et al., 1995; Kammermeier et al., 2000; Schiff et al., 2000; Richman et al., 2005; Tedford and Zamponi, 2006).

Our lab has shown that e37a expression in $Ca_V2.2$ channels enhances G protein mediated VII when compared to e37b. We have also found that a tyrosine residue in $Ca_V2.2e[37a]$ (Y1747) is essential for VII through $G_{i/o}$ protein coupled receptors (specifically $GABA_B$ and μ-opioid receptors); this amino acid is a phenylalanine (F1747) in $Ca_V2.2e[37b]$ channels (Figure 1.6, black arrow) (Raingo et al., 2007). This work also showed that VII of $Ca_V2.2e[37a]$ channels requires src tyrosine kinase. We do not know the target of src tyrosine kinase but it is attractive to speculate that it is Y1747. Chapter 3 of this thesis explores these VDI and VII mechanisms in mice engineered to express only $Ca_V2.2e[37a]$, or only $Ca_V2.2e[37b]$ channels (Andrade et al., 2010).

Competing interactions between $Ca_V2.2$, $Ca_V\beta$, and Gβγ regulate channel surface function

Many protein-protein interactions are known to regulate the function of $Ca_V2.2$ channels; in this section I will focus on interactions regulating surface levels of $Ca_V2.2$. Arguably, the two best understood interactions are between $Ca_V2.2$, and the regulatory proteins $Ca_V\beta$ and Gβγ.

All four $Ca_V\beta$ subunits interact with the I-II linker of $Ca_V2.2$ within an 18 amino acid domain termed the “alpha interaction domain” or AID (Figure 1.4) (Pragnell et al., 1994).

The AID interacts with a 41 amino acid sequence in $Ca_V2.2$, termed the “beta interaction domain” or BID (De Waard et al., 1994; De Waard et al., 1996). $Ca_V\beta$ subunit binding to $Ca_V2.2$ promotes channel targeting to the membrane surface, but there are also effects on channel kinetics (Singer et al., 1991; Brice et al., 1997). $Ca_V\beta$ enhancement of VGCC trafficking is believed to be due to a chaperone-like effect perhaps through occlusion of endoplasmic reticulum (ER) retention sites on the channel $Ca_V\alpha_1$ subunit (Dolphin, 2003a; Waithe et al., 2011). The effects of $Ca_V\beta$ subunits on channel gating include alternations in the voltage-dependence of activation (Olcese et al., 1996) and the voltage-dependence of inactivation (Dolphin, 2003a). Overall, $Ca_V\beta$ binding supports more $Ca_V2.2$ channels on the cell surface, and these channels open more readily in response to membrane depolarization.

Gβγ binding to $Ca_V2.2$ is thought to mediate VDI. Several groups have shown that Gβγ binding, and the resultant inhibition, is highly dependent on the interaction of $Ca_V2.2$ with $Ca_V\beta$ (Dolphin, 2003b). Current thinking favors a mechanism by which Gβγ binds more favorably to $Ca_V2.2$ when $Ca_V\beta$ is bound, and that Gβγ displaces the $Ca_V\beta$ subunit through an allosteric mechanism (Dolphin, 2003b). Strong depolarization delivered by endogenous action potential trains, or electrophysiologically, through a “prepulse facilitation” voltage step (to +80), reduces the affinity of Gβγ for $Ca_V2.2$, and at the same time increases the affinity of $Ca_V\beta$ for $Ca_V2.2$ (Bean, 1989; Ikeda, 1991; Hille, 1994; Dolphin, 2003b). As the membrane potential again hyperpolarizes, active Gβγ re-binds to and interferes with the function of $Ca_V2.2$ channels (Dolphin, 2003b).

The interplay between $Ca_V2.2$, $Ca_V\beta$ and Gβγ strikes a balance between activation and inhibition of $Ca_V2.2$. Apart from these interactions, several other protein-protein interactions are known to regulate the function of $Ca_V2.2$ channels. A comprehensive analysis of the protein-protein interactions involving $Ca_V2.2$ is shown in Figure 1.4. In our quest to better understand $Ca_V2.2$, specifically the $Ca_V2.2e[37a]$ and $Ca_V2.2e[37b]$ isoforms, we performed a yeast two-hybrid screen to identify novel protein-protein interactions with each isoform. This goal forms the framework for the following section and for my work on the ubiquitination of $Ca_V2.2$ channels (Chapter 2).

A screen for e37a/e37b binding partners

In order to better understand the functional differences between the $Ca_V2.2e[37a]$ and $Ca_V2.2e[37b]$ channels, a former graduate student, Andrew Castiglioni performed two parallel yeast two-hybrid screens. The two screens involved the proximal 108 amino acids of C-termini from each isoform. One screen employed the use of a e37a construct (bait), while the second, a e37b bait construct ($37a_S$, $37b_S$; Figure 1.7). As both splice isoforms are expressed in the DRG, a rat DRG cDNA library was screened, (Bell et al., 2004). When I arrived in the lab, all of the resulting (prey) clones had been isolated but only a small fraction had been identified. I streamlined the identification process of these clones, and this process allowed me to quickly identify all of the remaining ~ 150 clones (~ 60 %) (Appendix A.1 Table 1a, Table 1b).

As we were interested in proteins that differentially interacted with the e37a and e37b baits, we found an interesting result. Ten of the isolated clones (of 106 total) from the

37b screen coded for ubiquitin activating enzyme E1 (UBE1, E1), while none of the 130 clones identified in the 37a screen isolated this transcript (Figure 1.7, A.1 Table 1b). All UBE1 clones tested subsequently were found to interact robustly with e37b baits, but not with e37a baits. This novel observation formed the basis for Chapter 2 of this thesis (Marangoudakis *et al*., manuscript in revision).

Ubiquitin, UBE1, and ubiquitination

Ubiquitin (Ub) is one of the most highly conserved protein bio-molecules in nature, and dates from the earliest of eukaryotic life (Sharp and Li, 1987; Hochstrasser, 2009). This ~ 7 kDa protein is conserved from yeast to man and it has acquired only minor changes during this evolutionary period (Glickman and Ciechanover, 2002; Yi and Ehlers, 2005, 2007). In humans, Ub is a 76 amino acid protein that contains 7 lysine residues and a C-terminal glycine residue critical to its structure and function (Ciechanover, 1998; Hershko and Ciechanover, 1998). The lysines are found at positions: K6, K11, K27, K29, K33, K48 and K63 (Hershko and Ciechanover, 1998; Peng et al., 2003). Ub is expressed highly and ubiquitously in cells (hence its name) and it is conjugated to many proteins. Its conjugation is responsible for mediating some of the most critical housekeeping roles in cells, including, protein degradation, signaling, internalization, and regulation of protein activation and function (Ciechanover, 1998; Hershko and Ciechanover, 1998).

Before Ub is appended to substrate proteins, it must be activated (Figure 1.8). Ub activation requires an interaction with UBE1 that binds to and activates one molecule of

ubiquitin through the use of ATP (Hershko and Ciechanover, 1998). In this reaction the Ub C-terminal glycine (G76) is adenylated and forms a thioester linkage with UBE1 (Hotton and Callis, 2008). This molecule of Ub is then shifted to ubiquitin conjugating enzyme E2 (E2). This Ub-bound E2 then associates with a substrate-specific E3 ubiquitin ligase protein (E3) to target substrate proteins for attachment of the Ub molecule. This attachment process is termed “ubiquitination” (Ciechanover, 1998; Hershko and Ciechanover, 1998).

In humans, hundreds of different E3 proteins exist, compared to only a handful of E2s, and usually only one E1 (a second form of E1, UBE1L2, was recently found to also be highly expressed in testis) (Hershko and Ciechanover, 1998; Pickart, 2001; Pelzer et al., 2007). In eukaryotes, there are two major types of E3 proteins. The more common is the RING (really interesting new gene) family, with >600 members and the less common are the HECT domain-containing ligases with ~30 members (Deshaies and Joazeiro, 2009; Rotin and Kumar, 2009). This large repertoire of E3 proteins provides the cell the diversity required for proper homeostasis, although more proteins with E3 functions are likely to be discovered.

Ubiquitination results in a covalent isopeptide bond between G76 of Ub and an amino group of the substrate protein. Usually, this attachment occurs on an ε-amino group of a substrate protein’s lysine side-chain. However, rarely, Ub can be attached to the amino group at the N-terminus of a protein substrate (Ciechanover, 2005). Additional ubiquitin molecules can be attached, forming ubiquitin chains, branches, or even more intricate

structures by appending additional ubiquitin monomers to the available lysine residues of Ub, or to its N-terminus (Hershko and Ciechanover, 1998; Kirisako et al., 2006). The multitude of possible structures and chain-types are thought to be responsible for the diversity of functional effects on substrate proteins.

Classically, it is understood that ubiquitin chains formed through K48 linkages target substrate proteins to the proteasome for degradation. By contrast, Ub chain attachments formed through lysine 63 (K63) are thought to influence function and structure of substrate proteins (Xu et al., 2009). K63-linked chains can lead to diverse protein-protein interactions and also to steric and allosteric changes in protein structure (Lim and Lim, 2010). Recent work however has shown that polyubiquitin chains formed through almost any linkage, except K63, can cause substrate degradation through the proteasome (Xu et al., 2009). The downstream consequences of ubiquitination differ depending on the substrate, and for most substrates they are not fully understood. However, there is recent agreement that ubiquitination mediates a multitude of downstream effects independently from degradation, including: protein internalization, as well as changes in substrate stability, activity, protein-protein interactions, and phosphorylation state (Hershko and Ciechanover, 1998; Yi and Ehlers, 2007; Lim and Lim, 2010). Until quite recently, ubiquitination was thought of as a death sentence for a substrate protein, but today ubiquitination is thought of as a reversible posttranslational modification, similarly to protein phosphorylation, acetylation, or methylation. The reversibility of ubiquitination is mediated through deubiquitinating enzymes (DUBs) (Amerik and Hochstrasser, 2004).

Ubiquitination of VGCCs

Several neuronal ion channels are ubiquitinated (Rotin and Staub, 2010). Postsynaptic AMPA and NMDA receptors are downregulated by ubiquitination (Colledge et al., 2003; Patrick et al., 2003; Fu et al., 2011), and $Ca_V1.2$ L-type channels were shown to be ubiquitinated (Kawaguchi et al., 2006; Altier et al., 2010). However, data on ubiquitination of presynaptic ion channels are lacking. Inhibition of the proteasome increases the efficiency of presynaptic transmission, implying that key proteins are controlled by the ubiquitin proteasome system (Speese et al., 2003; Rinetti and Schweizer, 2010). However, few presynaptic protein targets of Ub have been determined.

In studies by the laboratory of Annette Dolphin, Ca_V2 family full-length channels and hemichannels were tested for their sensitivity to proteasomal inhibition. They were not able to conclusively show ubiquitination of either full-length $Ca_V2.2$ or hemi-channel $Ca_V2.2$ constructs (Raghib et al., 2001; Page et al., 2004). Recent work from this lab however shows that $Ca_V2.2$ can be ubiquitinated. This work illustrates that association of $Ca_V2.2$ with $Ca_V\beta$ subunits inhibits channel ubiquitination and degradation through the proteasome (Waithe et al., 2011). Alternatively, a $Ca_V2.2$ mutant in the AID that cannot associate with $Ca_V\beta$ undergoes robust ubiquitination and degradation. They also conclude that this degradation is proteasome-dependent (Waithe et al., 2011). In Chapter 2 I show evidence that $Ca_V2.2$ is ubiquitinated isoform-specifically, and that this ubiquitination is regulated by alternative splicing at the e37 locus. I also show that

surface channels are affected by ubiquitination, and that their levels are controlled by the ubiquitin proteasome system (UPS).

Other post-translational modifications of $Ca_V2.2$

Apart from ubiquitination, few other post-translational modifications are known to affect $Ca_V2.2$, and all of these modifications involve phosphorylation. It has been shown that the binding of a SNARE protein to $Ca_V2.2$ is affected by phosphorylation at serine residues within the II-III linker (Yokoyama et al., 2005). Additionally, one of the protein-protein interactions highlighted in Figure 1.4 is mediated by tyrosine phosphorylation of $Ca_V2.2$ (Schiff et al., 2000). In this case, phosphorylation within the synprint site of $Ca_V2.2$ is required for an interaction with RGS12, a regulator of G protein signaling (RGS). Phosphorylation and subsequent interaction with RGS12 affects the rate of desensitization of $Ca_V2.2$ channels, following voltage-independent inhibition (Schiff et al., 2000; Richman et al., 2005). A third group has shown that phosphorylation of the I-II linker reduces ERK kinase-dependent channel inhibition (Martin et al., 2006). Apart from these phosphorylation and the ubiquitination events however, no other data on post-translational modification of $Ca_V2.2$ exist.

$Ca_V2.2$ blockage by exogenous factors

In Chapter 4 I explore an exogenous mechanism found to inhibit surface $Ca_V2.2$ channel function. This work was the result of a collaborative effort with the laboratory of Robert Hurt of the Department of Engineering. Our goal was to study potential carbon nanotube-mediated block of $Ca_V2.2$. We found that the carbon nanotubes in solution

blocked $Ca_V2.2$ calcium currents. However, this block was not through a direct carbon nanotube-mediated mechanism as hypothesized. We found that inhibition of $Ca_V2.2$ channels was mediated by leached ionic yttrium (Y^{3+}) that was retained from an yttrium/nickel catalyst during production. In this chapter (Chapter 4) we show that yttrium was released from carbon nanotubes at levels sufficient to inhibit the flow of calcium through $Ca_V2.2$ channels.

This block occurs because Y^{3+}, as with other transition metals such as La^{3+}, Ni^{2+}, Co^{2+}, Cd^{2+}, *et cetera*, have higher affinities for the channel's calcium binding site than calcium does, and they can displace calcium from this site (Lansman et al., 1986). Also, because they bind so strongly, they have very slow rates of permeation (Figure 1.9) (Sather and McCleskey, 2003). At least one group has shown neuronal specific effects of carbon nanotubes in culture, however a mechanism based on metal contamination was likely not considered as an explanation of these results (Malarkey et al., 2008). We discuss the consequences of such a block in the discussion section of Chapter 4.

$Ca_V2.2$ channels as targets for therapeutics

Several studies have linked $Ca_V2.2$ dysfunction to maladies such as chronic (neuropathic) pain resulting from nerve injury (Bowersox et al., 1996; Altier and Zamponi, 2004; Costigan et al., 2009). Indeed, mice lacking functional $Ca_V2.2$ channels have higher pain thresholds compared to wild type mice, and in some studies they have reduced symptoms of neuropathic pain (Hatakeyama et al., 2001; Kim et al., 2001; Saegusa et al., 2002). In humans, one of the standard treatments for chronic pain has

been morphine (von Zastrow et al., 2003). An endogenous target of morphine is the μ-opioid receptor, and a target of this receptor is $Ca_V2.2$ (Waldhoer et al., 2004). Morphine works by co-opting the μ-opioid receptor's endogenous signaling pathways, leading to VDI and VII of presynaptic Ca_V2 channels, inhibition of sodium channels, and activation of potassium channels (Scott et al., 2002). However, non-specific as well as off-target effects of morphine mediate addictiveness and other side-effects. Thus, alternatives to morphine for treating chronic pain are imperative (von Zastrow et al., 2003).

Not long ago it was discovered that blocking $Ca_V2.2$ channels with omega-conotoxins CVID, GVIA, and MVIIA could alleviate chronic neuropathic pain (Bowersox et al., 1996; Wang et al., 2000; Scott et al., 2002). Ultimately, this led to the production and FDA approval of a conotoxin-derived therapeutic for the treatment of chronic pain (Garber, 2005). This drug (Prialt®), a synthetic peptide analogue of *Conus* toxin MVIIA, formed a new class of calcium channel blocking therapeutics. This peptide has proven to be up to 1,000 times more potent than morphine in treating chronic pain in humans (Staats et al., 2004). Unlike morphine, which has multiple targets, Prialt® directly and specifically inhibits $Ca_V2.2$, resulting in high potency (Scott et al., 2002; Altier and Zamponi, 2004). The significant benefits of this drug are the lack of tolerance and addictiveness, both common side-effects of morphine (Malmberg and Yaksh, 1995; Staats et al., 2004). As a peptide, however, the drawbacks include low stability *in vivo*. Resultantly, it must be routinely injected into the spinal cord (intrathecally) by implanted pump mechanism. Also, since this drug blocks $Ca_V2.2$ channels generally, regardless of the stimuli they transmit, general nerve function can be impacted, leading to significant side effects

(Garber, 2005). Thus, although this novel class of drug has proven helpful, we are always in need of therapeutics with greater specificity. The following chapters of my thesis explore $Ca_V2.2$ as both an important therapeutic target (Chapter 3), as well as a target of endogenous mechanisms of regulation (Chapter 2).

Conclusion

Cellular control of $Ca_V2.2$ channel activity is essential for normal neuronal function. Cells employ alternative splicing, post-translational modifications, and protein-protein interactions to control channel function. In this thesis I explore $Ca_V2.2$ channel regulation by three different mechanisms: ubiquitination, specifically of the $Ca_V2.2e$[37b] channel (Chapter 2); G protein-mediated inhibition, mediated through the μ-opioid receptor (Chapter 3); and yttrium block, resulting from contaminated carbon nanotubes (Chapter 4). In the final chapter (Chapter 5), crosstalk between these inhibitory mechanisms, as well as alternative models, and potential clinical relevance of the findings are explored.

Figure 1.1

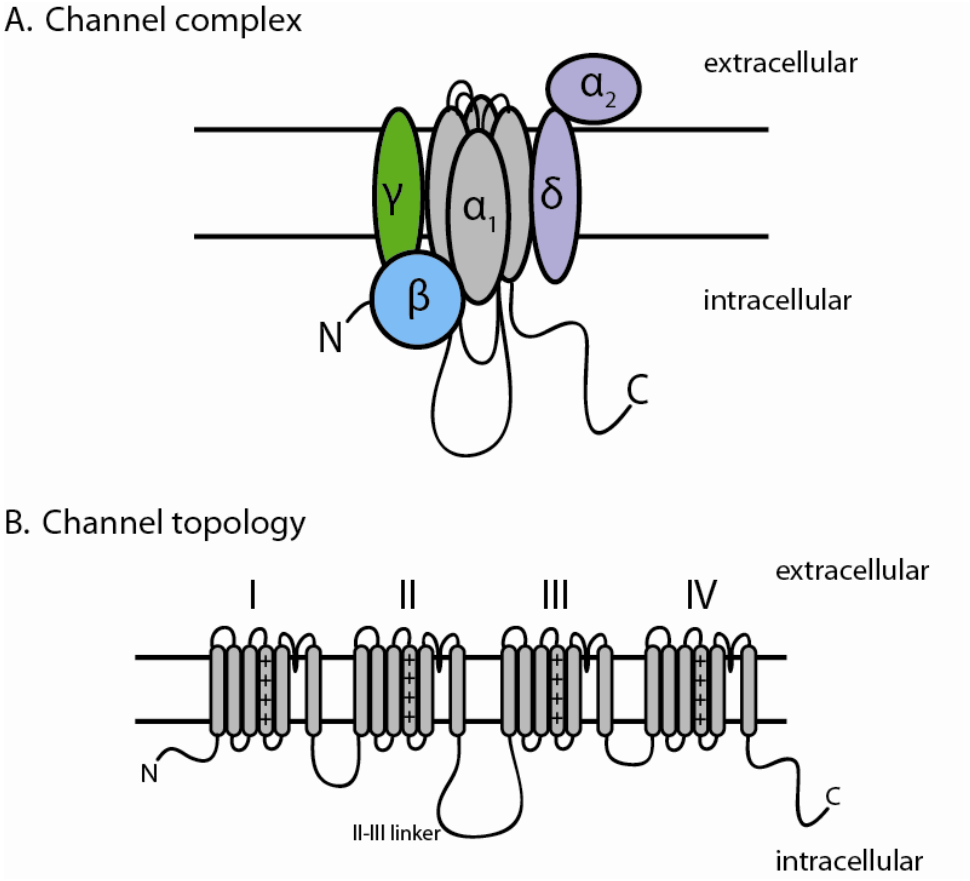
A. Channel complex
extracellular
α2
γ
α1
δ
β
intracellular
N
C
B. Channel topology
extracellular
I
II
III
IV
N
C
II-III linker
intracellular

Figure 1.1

Voltage-gated calcium channel structure. **(A)** VGCCs are composed of the main pore forming subunit, $Ca_V\alpha_1$, (α_1, central grey subunit) as well as $Ca_V\beta$ (β, blue circle), $Ca_V\alpha_2\delta$ (α_2 and δ, purple elliptical) and sometimes $Ca_V\gamma$ (γ, green elliptical). The β component is intracellular and soluble, although at least one version ($Ca_V\beta_{2a}$) is membrane anchored through palmitoylation domains (Chien et al., 1996; Dolphin, 2003a). The $\alpha_2\delta$ component is the product of a single gene that is posttranslationally cleaved and re-attached through a disulfide bond; this results in a transmembrane δ component, and an extracellular α_2 component (Dolphin, 2009). The γ subunit is not associated with most VGCCs, and has been found associated mainly with L-type channels derived from muscle tissue (Takahashi et al., 1987; Dolphin, 2003b, 2009). **(B)** $Ca_V2.2$ in topological display. All VGCCs share a common structure of four domains (I-IV), each consisting of six transmembrane domains (S1-6). The positive charges in S4 (provided by lysine and arginine residues) contribute to the voltage sensor. Four positive charges are shown in the figure, however the actual number of positively charged residues varies by linker (Hille, 2001). The P-loop region connecting S5 and S6 contains the glutamate residues responsible for pore formation and ion selectivity (Tedford and Zamponi, 2006).The structure modeled here is that of $Ca_V2.2$, but there is little discernable difference in terms of general structure between $Ca_V2.2$ and the other nine VGCCs. The intracellular domains share conservation between VGCCs, although the number and identity of the residues varies.

Figure 1.2

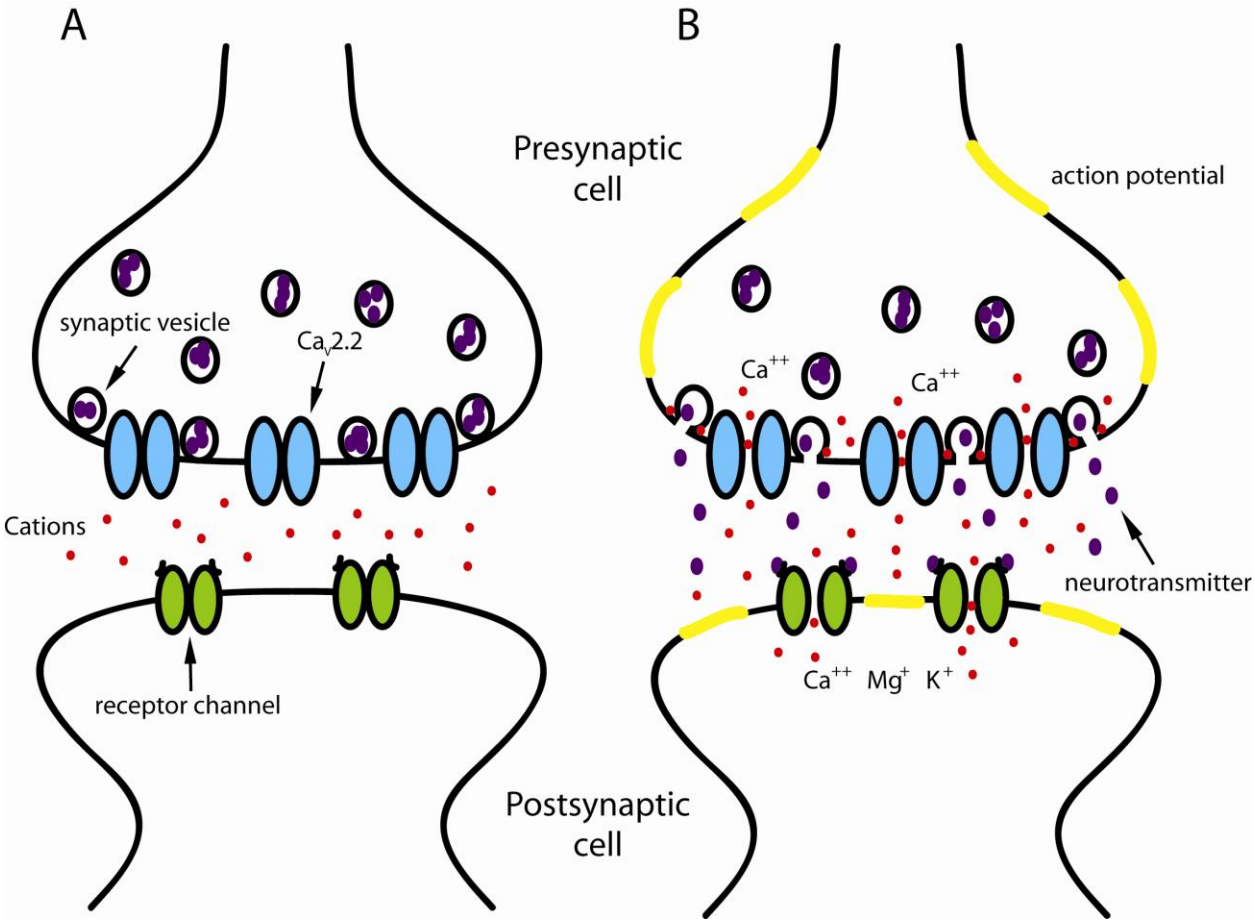
A
B
Presynaptic cell
action potential
synaptic vesicle
$Ca_v2.2$
Ca^{++}
Ca^{++}
Cations
neurotransmitter
receptor channel
Ca^{++} Mg^{+} K^{+}
Postsynaptic cell

Figure 1.2

$Ca_V2.2$ calcium channels as gatekeepers of neurotransmitter release. This figure highlights the role of $Ca_V2.2$ channels in **(A)** inactive, and **(B)** active synapses. $Ca_V2.2$ channels are shown in blue in the presynaptic cell. A strong depolarization of the plasma membrane **(B)** results in increased probability of channel opening. Upon opening, these channels transduce Ca^{2+} into the cell. Calcium ions bind to the calcium sensing region of synaptic proteins, mediating fusion of the synaptic vesicle membrane with the plasma membrane. This results in neurotransmitter release (purple spheres) into the synaptic cleft (Li and Chin, 2003). The degree of synaptic vesicle depletion depends on the size and frequency of activation (Rizzoli and Betz, 2005). Following synaptic vesicle fusion, released neurotransmitters bind receptors on the postsynaptic cell. In this case the neurotransmitters mediate activation of the postsynaptic cell by binding excitatory ionotropic ligand-gated ion channels (shown here as nondescript NMDA and AMPA receptors). These cause an influx of cations such as Ca^{2+}, Mg^{+}, and K^{+}. $Ca_V2.2$ calcium channels can also however mediate the release of inhibitory neurotransmitters, and neurotransmitters with neither a clear excitatory nor inhibitory effect. For simplicity's sake those have not been depicted here.

Figure 1.3

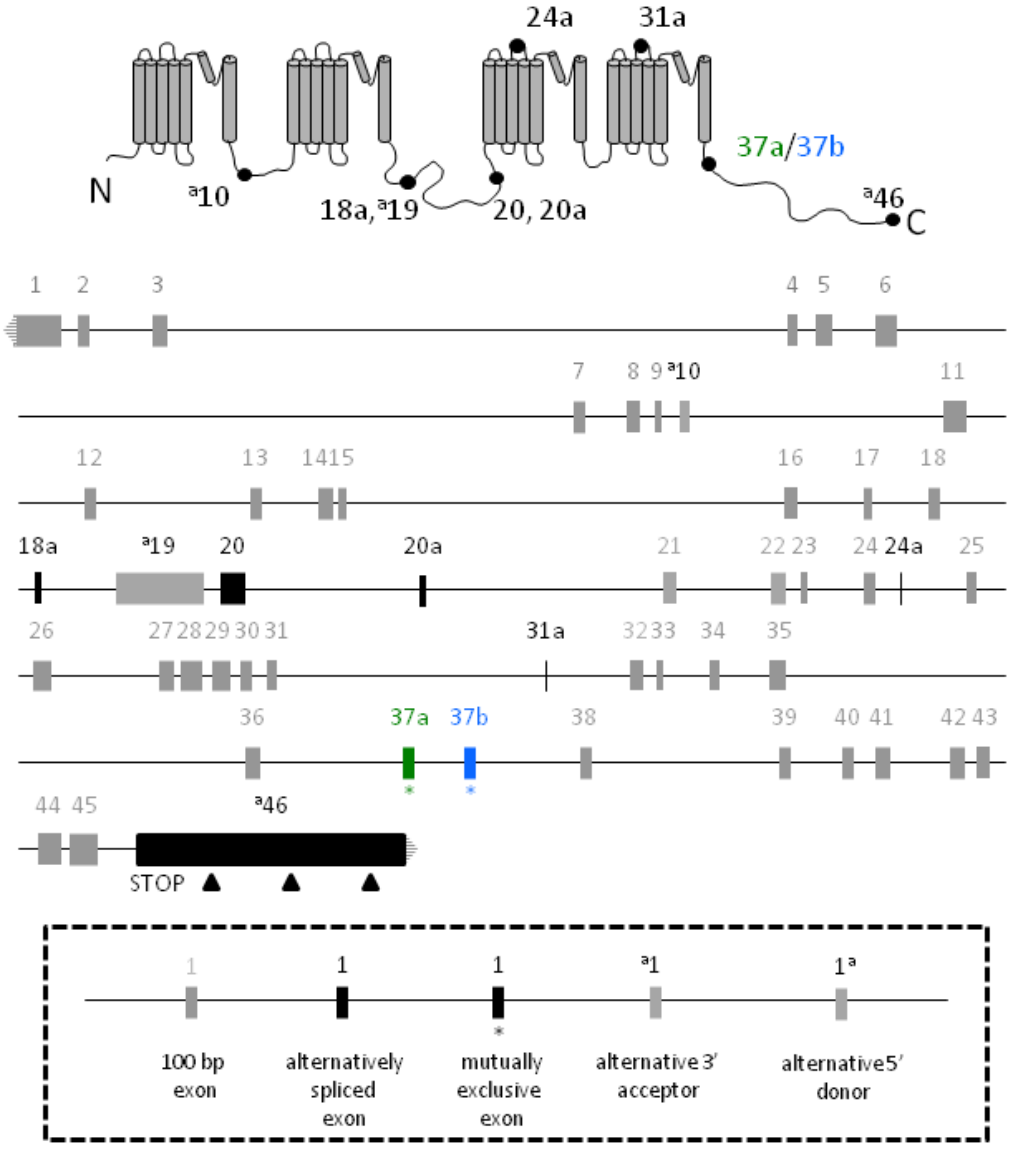
24a
31a
37a/37b
N
ª10
18a, ª19
20, 20a
ª46
C
1 2 3
4 5 6
7 8 9 ª10
11
12
13 1415
16 17 18
18a
ª19
20
20a
21
22 23
24 24a
25
26
27 28 29 30 31
31a
32 33
34
35
36
37a
37b
38
39
40 41
42 43
44 45
ª46
STOP
1
1
1
ª1
1ª
100 bp exon
alternatively spliced exon
mutually exclusive exon
alternative 3′ acceptor
alternative 5′ donor

Figure 1.3

(Figure is adapted from Lipscombe *et al.* 2002)

$Ca_V2.2$ gene structure and alternative splicing. **(Top)** Topographical map of the $Ca_V2.2$ protein with regions coded by alternative exons denoted with black circles. **(Bottom)** Gene structure of $Ca_V2.2$ with introns labeled as thin black lines and exons denoted as boxes. Constitutive exons are grey and alternative exons are black. Various types of alternative splicing are explained in the legend below the schematic. Currently, at least 10 exons are known to be alternatively spliced in the *Cacna1b* gene. These are referenced in Lipscombe *et al*. 2002. This gene structure was constructed from analysis of human genomic sequence NT_023929.

Figure 1.4

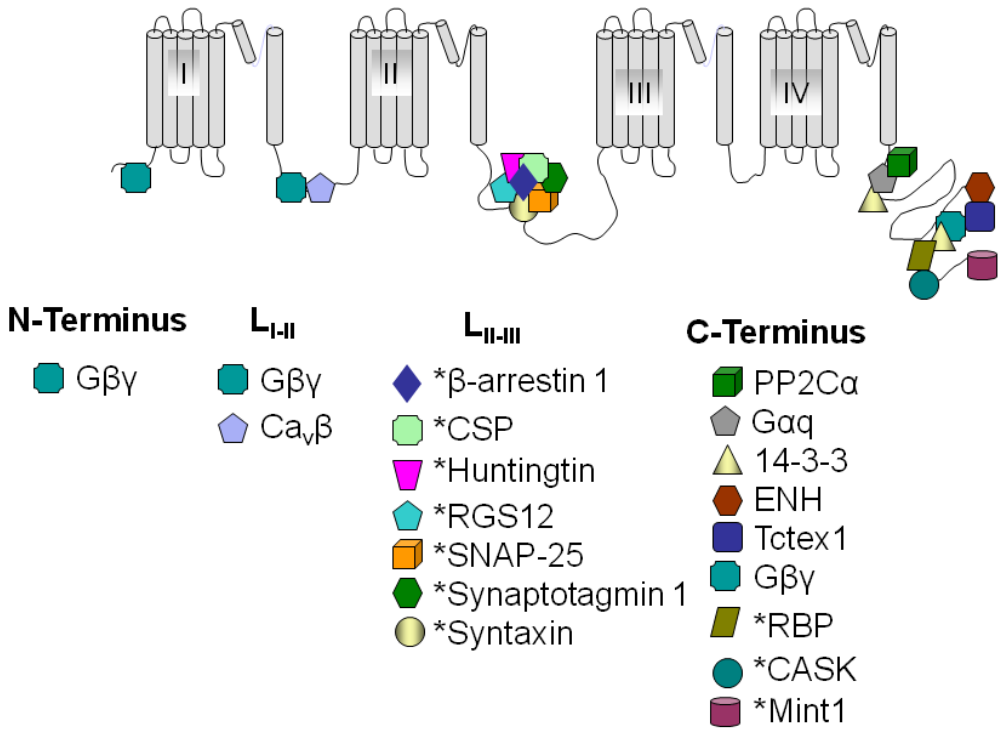
I
II
III
IV
N-Terminus
Gβγ
L I-II
Gβγ
Cavβ
L II-III
*β-arrestin 1
*CSP
*Huntingtin
*RGS12
*SNAP-25
*Synaptotagmin 1
*Syntaxin
C-Terminus
PP2Cα
Gαq
14-3-3
ENH
Tctex1
Gβγ
*RBP
*CASK
*Mint1

Figure 1.4

(This figure was created by **Spiro Marangoudakis** and was published previously in: Lipscombe D, *et al.* (2009). Alternative splicing of neuronal Ca_V2 calcium channels. *Structure, Function, and Modulation of Neuronal Voltage-Gated Ion Channels*. Wiley)

Protein-protein interactions involving $Ca_V2.2$. Proteins interact most notably with the II–III intracellular linker and with the C-terminus. A number of proteins involved in synaptic transmission interact with the II–III linker of $Ca_V2.2$, including: CSP (cysteine string protein) (Miller et al., 2003), SNAP-25 (Catterall, 1998), synaptotagmin 1 (Sheng et al., 1997), syntaxin 1A (Sheng et al., 1994), huntingtin (Swayne et al., 2005), RGS12 (Richman et al., 2005), and b-arrestin (Puckerin et al., 2006). The asterisk (*) denotes proteins whose binding is either known or expected to be modified by alternative splicing. Binding of SNAP-25, synaptotagmin, and syntaxin is isoform dependent (Catterall, 1998). A $Ca_V2.2$ splice isoform lacking most of the II–III linker (e19 through e21) (Kaneko et al., 2002) theoretically should not interact with proteins that bind to this region. A second group of proteins interacts with the C-terminus, including 14-3-3 (Li et al., 2006), CASK (Maximov and Bezprozvanny, 2002), ENH (enigma homologue protein) (Maeno-Hikichi et al., 2003), Gαq (Simen et al., 2001), Gβγ (De Waard et al., 2005), Mint1 (Maximov et al., 1999), PP2Ca (Li et al., 2005), RIM binding protein (RBP) (Hibino et al., 2002), and Tctex1 (Lai et al., 2005). CASK and Mint1 do not bind to a truncated splice isoform of $Ca_V2.2$ (Maximov et al., 1999; Maximov and Bezprozvanny, 2002). Theoretically, Rim binding protein should not bind to the truncated splice isoform of $Ca_V2.2$ described by Bezprozvanny and colleagues (Maximov et al., 1999). Gβγ and $Ca_V\beta$ subunits interact with the I–II linker (Pragnell et al., 1994; De Waard et al., 2005).

Based on their sites of interaction in the I–II loop, alternative splicing at e10 should not disrupt Gβγ and Ca_Vβ binding directly. The N-terminus is not known to undergo alternative splicing, thus the Gβγ (Canti et al., 1999) site should also not be affected by splicing.

Figure 1.5

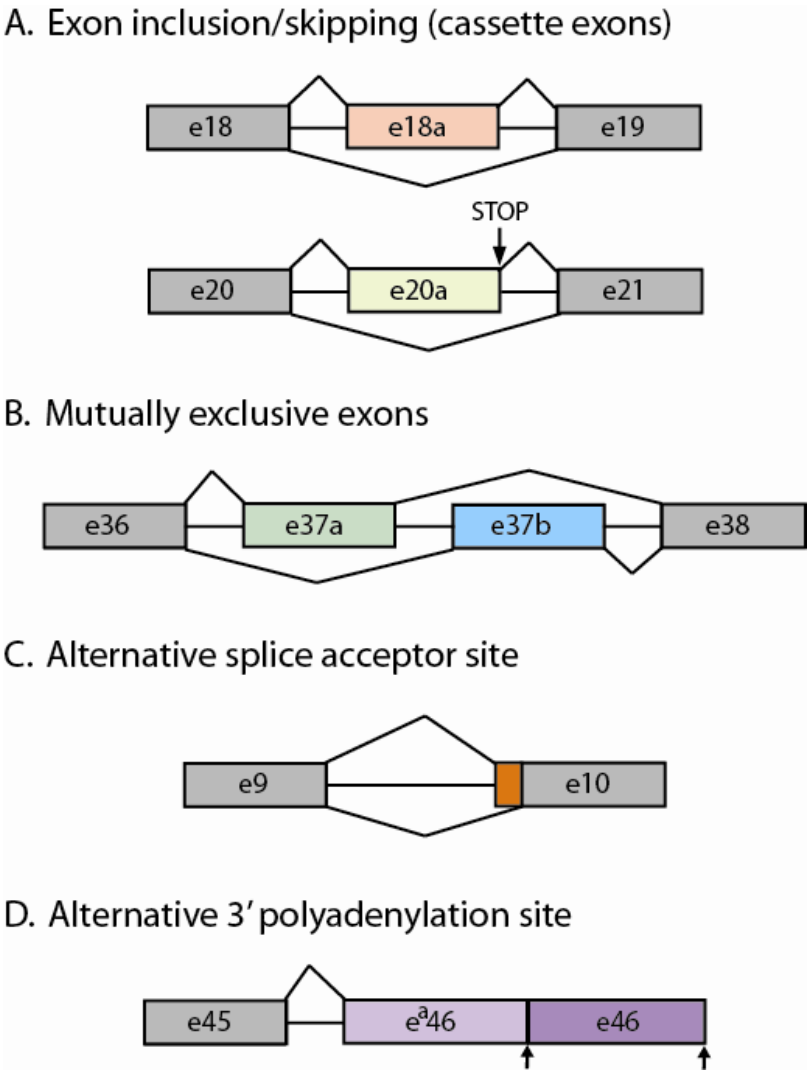
A. Exon inclusion/skipping (cassette exons)
e18
e18a
e19
STOP
e20
e20a
e21
B. Mutually exclusive exons
e36
e37a
e37b
e38
C. Alternative splice acceptor site
e9
e10
D. Alternative 3′ polyadenylation site
e45
e^a46
e46

Figure 1.5

Alternative splicing of $Ca_V2.2$. **(A)** The most common form of alternative splicing associated with $Ca_V2.2$ involves inclusion/exclusion of cassette exons. The two examples shown above are exon e18a detailed in Thaler *et al*. 2004, and exon 20a which I discovered in mouse and rat tissue (described in Chapter 1). **(B)** Highly homologous exons 37a and 37b act as a mutually exclusive pair. **(C)** Exon 10 can form an alternate version (^{a}10), in which a portion of the upstream intron is retained through an alternate 3' splice acceptor site. The splicing event yields one extra codon. **(D)** Several polyadenylation sites exist in exon 46, leading to truncation of the C-terminus (Lipscombe et al., 2002).

Figure 1.6

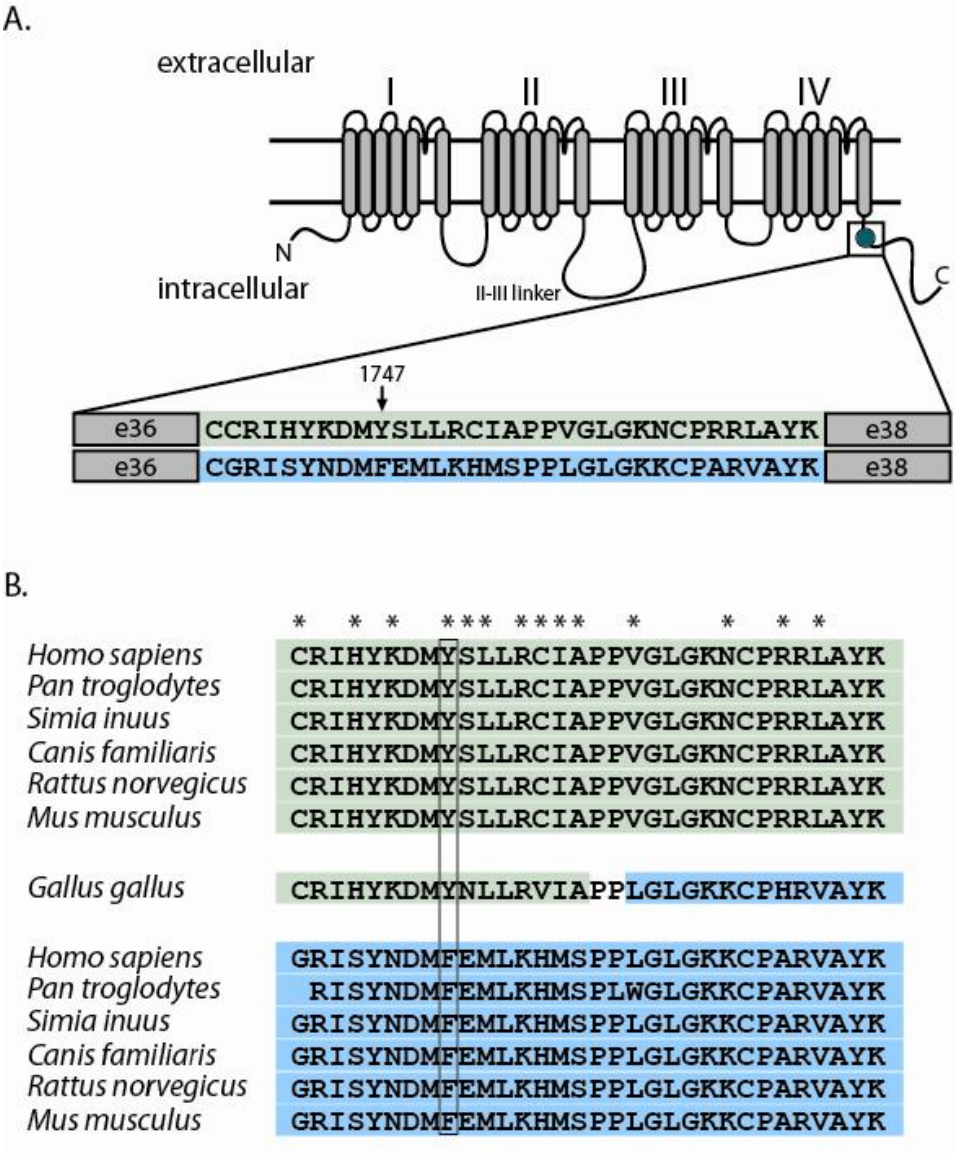
A.
extracellular
I
II
III
IV
N
C
intracellular
II-III linker
1747
e36 CCRIHYKDMYSLLRCIAPPVGLGKNCPRRLAYK e38
e36 CGRISYNDMFEMLKHMSPPLGLGKKCPARVAYK e38
B.
* * * *** **** * * * *
Homo sapiens CRIHYKDMYSLLRCIAPPVGLGKNCPRRLAYK
Pan troglodytes CRIHYKDMYSLLRCIAPPVGLGKNCPRRLAYK
Simia inuus CRIHYKDMYSLLRCIAPPVGLGKNCPRRLAYK
Canis familiaris CRIHYKDMYSLLRCIAPPVGLGKNCPRRLAYK
Rattus norvegicus CRIHYKDMYSLLRCIAPPVGLGKNCPRRLAYK
Mus musculus CRIHYKDMYSLLRCIAPPVGLGKNCPRRLAYK
Gallus gallus CRIHYKDMYNLLRVIAPPLGLGKKCPHRVAYK
Homo sapiens GRISYNDMFEMLKHMSPPLGLGKKCPARVAYK
Pan troglodytes RISYNDMFEMLKHMSPLWGLGKKCPARVAYK
Simia inuus GRISYNDMFEMLKHMSPPLGLGKKCPARVAYK
Canis familiaris GRISYNDMFEMLKHMSPPLGLGKKCPARVAYK
Rattus norvegicus GRISYNDMFEMLKHMSPPLGLGKKCPARVAYK
Mus musculus GRISYNDMFEMLKHMSPPLGLGKKCPARVAYK

Figure 1.6

$Ca_V2.2$ exons 37a and 37b. Exons 37a and 37b code for peptides in the proximal C-terminus of $Ca_V2.2$. **(A)** The protein sequences derived from exons 37a (top, green) and 37b (bottom, blue) are found in the proximal C-terminus of $Ca_V2.2$. They differ by 14 of 33 amino acid residues. Tyrosine 1747 (Y1747, black arrow) is found in $Ca_V2.2$e[37a] channels, however that position in $Ca_V2.2$e[37b] channels is occupied by a phenylalanine residue. These residues mediate significant differences in functional output between the two channels, and are described in this thesis as well as in Raingo *et al.* 2007. **(B)** An alignment of the protein sequence coded by exons 37a (top) and 37b (bottom) from human, chimpanzee, macaque monkey, dog, rat and mouse. Only one exon encodes e37 in chicken, and the exon is a hybrid of e37a and e37b, with the first half being more highly homologous to e37a and the second half being more homologous to e37b. High conservation is evident among both exons in all organisms analyzed. Chicken e37 shows high homology to both e37a and e37b. Position 1747 is highlighted in the alignment. Residues not conserved between 37a and 37b are marked with an asterisk; there are 14 in total. The first cysteine is conserved between e37a and e37b and is gaped out of the sequences.

Figure 1.7

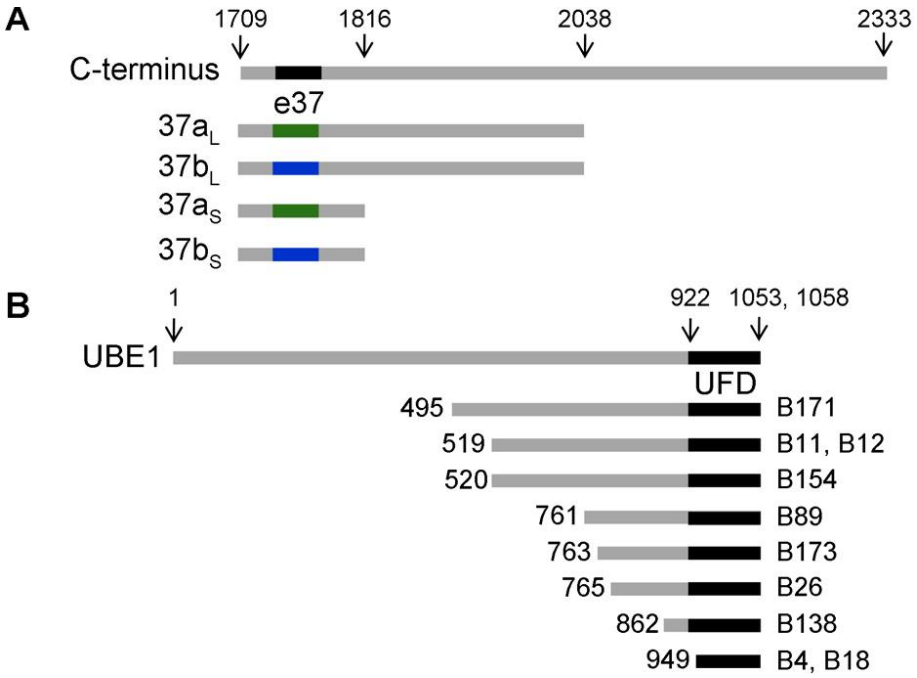
A
1709
1816
2038
2333
C-terminus
e37
37a$_L$
37b$_L$
37a$_S$
37b$_S$
B
1
922
1053, 1058
UBE1
UFD
495
B171
519
B11, B12
520
B154
761
B89
763
B173
765
B26
862
B138
949
B4, B18

Figure 1.7

Yeast two-hybrid bait and prey clones. **(A)** Bait constructs used in the yeast two-hybrid screen ($37a_S$, $37b_S$) contained the first 108 amino acid residues of the proximal C-terminus of $Ca_V2.2$ (aa 1709-1816, numbering according to AY211499 (Bell, Thaler et al. 2004)). Longer bait constructs ($37a_L$, $37b_L$) were also created for control yeast two-hybrid experiments, but not used in the actual screening process (aa 1709-2038). Both of these constructs are explained further in Chapter 2. **(B)** The 10 UBE1 clones isolated in the screen are aligned to the full-length UBE1 protein. Each clone is listed with its unique identifying number assigned to it during screening. The ubiquitin fold domain (UFD, aa 922-1053; black bar) is also shown. All clones contain all or most of this domain. These clones are described in more detail in Chapter 2.

Figure 1.8

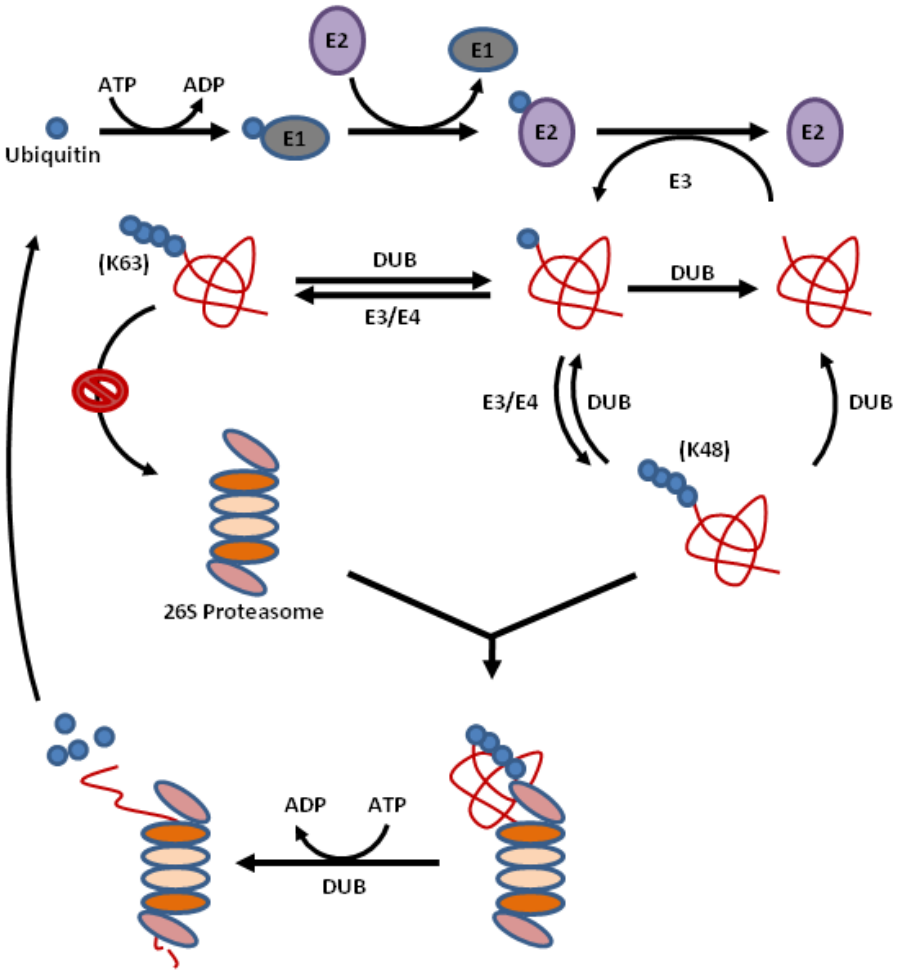
E2
E1
ATP
ADP
Ubiquitin
E1
E2
E2
E3
(K63)
DUB
E3/E4
DUB
E3/E4
DUB
DUB
(K48)
26S Proteasome
ADP
ATP
DUB

Figure 1.8

Ubiquitination and the ubiquitin proteasome pathway. Ub is activated by E1. Ub is then transferred to Ub conjugating enzyme E2 (E2), which then in conjunction with E3 ubiquitin ligases (E3) targets proteins for monoubiquitination. Monoubiquitin tags can then be elongated by the same E3, or additional E3s. E4 enzymes can also elongate ubiquitin chains from a preexisting monoubiquitination. Ubiquitin molecules can however be removed from chains by deubiquitinating enzymes (DUBs), reverting to the monoubiquitinated, or Ub-free form of the substrate. Chains formed through K48 linkages associate with the 19S cap of the 26S proteasome and become targeted for degradation (Hershko and Ciechanover, 1998). Chains formed through K63 linkages have not been shown to associate with the proteasome, and thus do not mediate degradation through this mechanism. Once associated with the proteasomal cap, various proteins unfold the substrate protein, allowing it to be threaded through the proteasome. Concurrently, DUBs remove ubiquitin. Ub is subsequently free to enter the cycle once more. At the end of the process, substrate proteins are broken down into small polypeptides (average length of 7-9 amino acid residues) (Voges et al., 1999). Downstream processes then break these peptides down into individual amino acids which can then be used for protein synthesis.

Figure 1.9

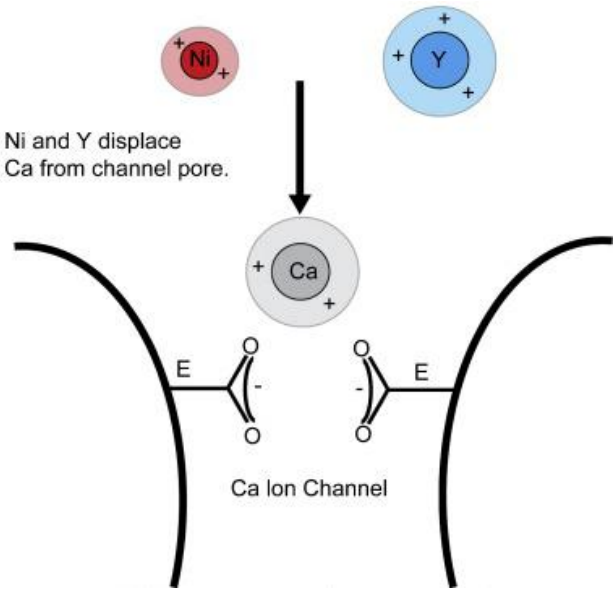
Ni
Y
Ni and Y displace
Ca from channel pore.
Ca
E
O
O
-
O
O
-
E
Ca Ion Channel

Figure 1.9

(This was adapted from a figure previously published in Jakubek/ **Marangoudakis** *et al.*, 2009; the complete figure is shown as Figure 4.5 in Chapter 4.)

Inhibition of $Ca_V2.2$ through metal ions. The Ca^{2+} selective pore of the $Ca_V2.2$ voltage-gate calcium channel is shown as curved black lines. The glutamates forming the calcium-binding site(s) are oriented with their carboxylate side chains positioned toward the center of the pore. Only two of the four glutamate residues are shown. These glutamates are critical for the selectivity and permeation of Ca^{2+} ions through the pore (Sather and McCleskey, 2003). Yttrium (Y^{3+}), and to a lesser extent nickel (Ni^{2+}), occlude the pore due to their strong binding (Nachshen, 1984). Ni^{2+} are effective blockers at higher concentrations, as is evident in Chapter 4.

CHAPTER 2

UBIQUITINATION AND PROTEASOME TARGETING OF N-TYPE $Ca_V2.2$ CHANNELS DEPENDS ON ALTERNATIVE SPLICING

Manuscript written by Spiro Marangoudakis and Diane Lipscombe.

This chapter has been submitted for peer review as: **Marangoudakis S**, Andrade A, Helton TD, Denome S, Castiglioni AJ, Lipscombe D. Ubiquitination and proteasome targeting on N-type $Ca_V2.2$ channels depends on alternative splicing. (In revision)

I performed all protein immunoblots and immunoprecipitations (Figures 2.3, 2.4, 2.5), as well as the yeast two-hybrid analyses (Figure 2.2) (apart from the original screen)

Arturo Andrade performed the electrophysiology in Figure 2.6C-F

Thomas Helton performed the electrophysiology in Figures 2.1B, 2.6A,B

Sylvia Denome created the $Ca_V2.2e[37a]^{Y1747F}$ clone

Andrew Castiglioni performed the original yeast two-hybrid screens

Acknowledgements

I would be remiss if I did not thank Arturo Andrade PhD, and Thomas Helton PhD, for their beautiful electrophysiology, and Andrew Castiglioni PhD for the quality of the initial yeast two-hybrid screens. I would also like to take the opportunity to thank professors Jeffrey Singer PhD, and Jeffrey Laney PhD, for their useful discussions on the topic of ubiquitination, and for sparking experiments and analyses. The National Institutes of Health supported this work through grants: NS29967 (D.L.) and 1F31NS066702 (S.M.).

Abstract

N-type calcium channels control the entry of calcium into neurons to regulate numerous essential functions including presynaptic transmitter release, neurite outgrowth, and excitability. N-type channel expression levels must be precisely controlled, however we know little of how neurons accomplish this. The ubiquitin proteasome system is used to regulate many presynaptic and postsynaptic receptors and ion channels to optimize synaptic efficiency. Surprisingly little is known about presynaptic calcium channel ubiquitination. Here we show that the core protein of N-type channels, $Ca_V2.2$, is ubiquitinated and, depending on alternative splicing, sensitive to the ubiquitin proteasome system. We showed previously that a pair of mutually exclusive exons, e37a and e37b that encode 33 amino acids in the proximal C-terminus of $Ca_V2.2$, strongly influence N-type current density. The most common $Ca_V2.2$ splice isoform in neurons contains e37b. We identify a specific and robust interaction between ubiquitin-activating enzyme E1 and $Ca_V2.2$ sequences containing e37b in yeast. Prompted by this finding, we discover that e37b-$Ca_V2.2$ proteins are ubiquitinated significantly more (70%) than e37a-$Ca_V2.2$ splice isoforms. E37b-specific ubiquitinated $Ca_V2.2$ protein is sensitive to proteasome inhibition by MG132, increasing N-type current densities in tsA201 cells and in mouse neurons by 40%. The broad expression pattern of e37b in the nervous system, relative to e37a that is enriched in a subset of nociceptors, suggests that the ubiquitin proteasome system exerts tonic down-regulation on the majority of neuronal N-type channels. We conclude that $Ca_V2.2$ channels are important targets of cellular ubiquitination and proteasome-dependent regulation of excitation-dependent calcium entry.

Introduction

Presynaptic Ca_V2 channels mediated calcium entry that trigger neurotransmitter release and support synaptic transmission (Catterall, 2000). $Ca_V2.2$ channels underlie N-type currents and they are sensitive to regulation by several cellular mechanisms with distinct temporal characteristics, including G protein-coupled receptors, posttranslational modifications, and protein interactions (Dunlap and Fischbach, 1978; Holz et al., 1986; Lipscombe et al., 1989; Hille et al., 1995; Ikeda and Dunlap, 1999; Altier et al., 2006; Dolphin, 2009). Relative to other synaptic proteins, and particularly postsynaptic receptors (Chen and Roche, 2007; Yi and Ehlers, 2007), we know little of the neuronal mechanisms that control surface expression of $Ca_V2.2$ channels.

Ubiquitination influences synaptic efficiency by modifying the trafficking, endocytosis and activity of presynaptic and postsynaptic receptors and ion channels (DiAntonio and Hicke, 2004; Yi and Ehlers, 2007; Rotin and Staub, 2010). Furthermore, activity-dependent ubiquitination of postsynaptic receptors regulates synaptic plasticity (Colledge et al., 2003; Patrick et al., 2003). Despite functional evidence that ubiquitin-dependent changes in synaptic efficacy involves presynaptic components (Speese et al., 2003; Bingol and Schuman, 2005 ; Rinetti and Schweizer, 2010), $Ca_V2.2$ channels are only newly recognized targets of the ubiquitin proteasome system (UPS) (Waithe et al., 2011).

Neurons employ alternative pre-mRNA splicing to optimize $Ca_V2.2$ channel activity (Lipscombe, 2005; Liao et al., 2009). By comparing the properties of functionally

validated splice isoforms we, and others, have discovered critical structural domains in $Ca_V2.2$ channels that control their properties (Maximov and Bezprozvanny, 2002; Bell et al., 2004; Thaler et al., 2004; Castiglioni et al., 2006; Altier et al., 2007; Raingo et al., 2007). One functionally important site of alternative splicing in $Ca_V2.2$ involves a pair of mutually exclusive exons, e37a and e37b, that alter 14 amino acids in the proximal C-terminus of the $Ca_V2.2$ channel (Figure 2.1) (Bell et al., 2004). E37a is enriched in nociceptors of dorsal root ganglia. We showed that e37a renders $Ca_V2.2$ ($Ca_V2.2e[37a]$) channels more susceptible to inhibition by $G_{i/o}$ protein-coupled receptors when compared to e37b ($Ca_V2.2e[37b]$) channels that are expressed throughout the nervous system (Raingo et al., 2007; Andrade et al., 2010). We also observed significantly greater N-type current densities in cells expressing cloned as well as native $Ca_V2.2e[37a]$ channels compared to $Ca_V2.2e[37b]$ (Figure 2.1) (Bell et al., 2004; Castiglioni et al., 2006; Raingo et al., 2007). By analyzing gating currents, we found that e37a associated with significantly more functional $Ca_V2.2$ channels at the cell surface (Castiglioni et al., 2006).

We speculated that e37a and e37b differentially influence protein interactions with the proximal $Ca_V2.2$ C-terminus. To test this, we screened for neuronal proteins that differentially interacted with e37a and e37b baits in a yeast two-hybrid screen. We found a protein essential for ubiquitination interacted selectively with the e37b-derived sequence. By biochemical and functional analyses of cloned and native channels, we conclude that e37b promotes ubiquitination of $Ca_V2.2$. The majority of neuronal $Ca_V2.2$ channels contain e37b and they are down-regulated by the UPS. By contrast, e37a

occludes this ubiquitination pathway, rendering these channels relatively insensitive to the UPS, and leading to greater current densities.

Results

Ubiquitin-E1 interacts specifically with e37b baits

We performed parallel yeast two-hybrid screens using baits that encode the first 108 amino acids of the $Ca_V2.2$ C-terminus and containing either e37a or e37b (bait constructs $37a_S$, $37b_S$; Figure 2.2A). For this screen, we generated a high quality cDNA library derived from dorsal root ganglia (DRG), where both e37a and e37b-containing channels are normally expressed. We isolated and identified a total of 236 (prey) clones encoding putative $Ca_V2.2$ binding partners from this screen. These clones survived high stringency selection media (see methods). A subset of these proteins were identified by proteomic analyses of $Ca_V2.2$ immunoprecipitated complexes by other groups (e.g. stathmin family proteins, adaptor protein components, microtubule associated protein 1B, CaMKIV, and latrophilin-1) (Khanna et al., 2007; Muller et al., 2010).

We focused on interactions that occurred with high frequency and that were specific to either the e37a or the e37b bait construct. By these criteria the most interesting clones encoded ubiquitin-activating enzyme E1 (UBE1). UBE1 is a critical component of the ubiquitin pathway (Glickman and Ciechanover, 2002). We identified 10 UBE1-derived sequences from a total of 106 prey clones isolated using the bait containing e37b (Figure 2.2B). By comparison, none of the 130 prey clones isolated using the e37a bait encoded UBE1 (Appendix A.1 Tables 1a and 1b).

To assess the robustness and specificity of the UBE1-e37b interaction, we co-transformed these prey clones back into yeast and studied the interactions between bait and prey proteins using high stringency media (Figure 2.2C). We found that UBE1 interacted strongly with both the e37b bait used in the screen, and also a longer clone containing more of the $Ca_V2.2$ C-terminus ($37b_S$ and $e37b_L$; Figure 2.2A, 2.2C). By contrast, yeast co-transformed with the UBE1 clone and the e37a screening bait, or a longer e37a construct, did not promote growth ($37a_S$ and $37a_L$; Figure 2.2A, 2.2C). Our data suggest that UBE1 does not interact with e37a-containing $Ca_V2.2$ sequences. To further test the specificity of UBE1-e37b interaction we found no evidence for an interaction between UBE1 and any of the following baits: $Ca_V2.2$ baits encoding a segment of the intracellular II-III linker ($II\text{-}III_1$, $II\text{-}III_2$); the corresponding C-terminal sequences of: P/Q-type $Ca_V2.1$ e37a ($2.1\text{-}37a_S$), L-type $Ca_V1.2$ ($1.2\text{-}CT_S$), and L-type $Ca_V1.3$ ($1.3\text{-}CT_S$); a Lamin-C clone (LAM, Clontech); or the naked Gal4 DNA binding domain (BD; pGBKT7, Clontech) (Figure 2.2C). Yeast co-transformed with UBE1 and the corresponding C-terminal region of e37b-containing $Ca_V2.1$ ($2.1\text{-}37b_S$) showed weak growth (Figure 2.2C). This weak interaction likely reflects the relatively high degree of amino acid sequence homology between e37b of $Ca_V2.1$ and $Ca_V2.2$ (79 %), that is greater than the homology between e37a and e37b of $Ca_V2.2$ (58 %). All 10 UBE1 clones isolated in our screen encode the C-terminal region and contain the ubiquitin fold domain (UFD), which suggests its importance in the interaction (Figure 2.2B). The UFD is essential for binding the ubiquitin-conjugating enzyme E2 (UBE2) and for mediating ubiquitin transfer from UBE1 to UBE2 (Nalepa et al., 2006; Schulman and Harper,

2009). Eight of the ten UBE1 clones were different lengths and therefore independent isolates (Figure 2.2B).

UBE1 is an essential and highly conserved member of the cellular ubiquitination pathway. During ubiquitination, ubiquitin (Ub) attaches to and is activated by UBE1, is then shuttled to UBE2, and then in concert with substrate-specific E3 ubiquitin ligases, is attached to substrate proteins (Ciechanover, 1998; Hershko and Ciechanover, 1998). During this process however, UBE1 is not known to interact with substrate proteins. Thus, the yeast two-hybrid UBE1-e37b interaction led us to consider that $Ca_V2.2e$[37b] channels may play a role in complex with UBE1, but apart from ubiquitination.

To explore the functional significance of our yeast two-hybrid results, we first performed immunoprecipitation analyses of full length $Ca_V2.2$ splice isoforms transiently expressed in the tsA201 (HEK293-derived) cell line. We found no evidence for a direct interaction between UBE1 and $Ca_V2.2$; neither $Ca_V2.2e$[37a] nor $Ca_V2.2e$[37b] co-immunoprecipitated with UBE1 (Figure 2.3). A native UBE1-$Ca_V2.2$ complex thus seemed unlikely. Others have however shown that endogenous protein bridges can form in yeast, linking functionally connected proteins in the two-hybrid assay (Rzymski et al., 2008). The UBE1-e37b interaction observed in our yeast two-hybrid screen therefore might reflect a process relevant to ubiquitination of $Ca_V2.2$, as a substrate protein. To test this, we directly measured cellular ubiquitination levels of full-length $Ca_V2.2$[e37a] and $Ca_V2.2e$[37b] proteins.

Ubiquitination of $Ca_V2.2$ protein is regulated by exon 37

We expressed full length $Ca_V2.2e[37a]$ and $Ca_V2.2e[37b]$ channel isoforms in tsA201 cells together with HA-tagged ubiquitin and immunoprecipitated $Ca_V2.2$. By immunoblot analyses using antibodies against HA and $Ca_V2.2$, we compared ubiquitination and total $Ca_V2.2$ protein levels between e37 isoforms (Figure 2.4). HA antibodies detected bands spanning a relatively wide range of molecular weights and running higher than bulk $Ca_V2.2$ protein (Figure 2.4). By comparing HA signals, we found that $Ca_V2.2e[37b]$ channels isolated from tsA201 cells were more strongly ubiquitinated compared to $Ca_V2.2[e37a]$ channels (Figure 2.4, 2.5A, 2.5B). We stripped and re-probed the same western blots with an antibody to ubiquitin (monoclonal clone P4D1), and this signal overlapped with the anti-HA signal as expected if they label the same protein pool (Figure 2.4). We then examined overall expression levels of $Ca_V2.2$ isoforms by stripping and re-probing the membrane with $Ca_V2.2$ antibodies, and normalized HA signal to total $Ca_V2.2$ signal to compensate for potential variations in expression. We found that $Ca_V2.2e[37b]$ protein was associated with 70 % greater ubiquitin signal compared to $Ca_V2.2e[37a]$ ($p = 0.005$; Figures 2.4, 2.5A, 2.5B). E37b-dependent ubiquitination could explain why fewer functional $Ca_V2.2$ channels are on the surface of cells expressing $Ca_V2.2e[37b]$ compared to those expressing $Ca_V2.2e[37a]$ isoforms (Castiglioni et al., 2006).

The Y1747F mutant of $Ca_V2.2e[37a]$ is associated with higher ubiquitination levels

To test our hypothesis further, we used an especially interesting mutant of $Ca_V2.2e[37a]$ in which we replaced tyrosine 1747 with phenylalanine (the corresponding amino acid in

$Ca_V2.2e[37b]$; Figure 2.1C, black arrow). In earlier studies we used this single point mutant of $Ca_V2.2e[37a]$ and showed that it effectively converted the $Ca_V2.2e[37a]$ channel phenotype to that of $Ca_V2.2e[37b]$. Namely, N-type current density and G protein modulation of $Ca_V2.2e[37a]^{Y1747F}$ were indistinguishable from $Ca_V2.2e[37b]$ (Raingo et al., 2007).

We compared ubiquitination levels of $Ca_V2.2e[37a]^{Y1747F}$ protein expressed in tsA201 cells with wild-type channels, and found that the ubiquitin signal associated with immunoprecipitated $Ca_V2.2e[37a]^{Y1747F}$ protein was significantly, and almost two-fold greater (~90 %), compared to wild-type $Ca_V2.2e[37a]$ $p = 0.017$; Figure 2.5A, 2.5B), and statistically indistinguishable from that of $Ca_V2.2e[37b]$ ($p = 0.54$; Figure 2.5A, 2.5B). These data link greater ubiquitination of $Ca_V2.2e[37b]$ and $Ca_V2.2e[37a]^{Y1747F}$ proteins to reduced N-type current densities relative to $Ca_V2.2e[37a]$ (Raingo et al., 2007).

Proteasome inhibition controls N-type current density in cells expressing $Ca_V2.2e[37b]$

Ubiquitin can control several aspects of protein function, but it is arguably best understood as a cellular tag to identify proteins for degradation through the proteasome (Ciechanover, 1998; Yi and Ehlers, 2007; Tai and Schuman, 2008). We used MG132, a well-known inhibitor of the proteasome to test if Ub-tagged $Ca_V2.2$ is degraded via the ubiquitin-proteasome system (Bloom and Pagano, 2005). We treated tsA201 cells expressing $Ca_V2.2e[37a]$ and $Ca_V2.2e[37b]$ clones with MG132 (Bloom and Pagano, 2005). Ubiquitinated $Ca_V2.2$ protein accumulated after MG132 treatment in cells expressing either isoform, however $Ca_V2.2e[37a]$ and $Ca_V2.2e[37b]$ protein levels

conjugated with ubiquitin were indistinguishable under these conditions (Figure 2.5C). We also did not detect changes in total $Ca_V2.2$ protein levels after MG132 treatment, even though ubiquitinated $Ca_V2.2$ protein levels increased. These data suggest that ubiquitinated $Ca_V2.2$ protein is a small fraction of total protein, consistent with $Ca_V2.2$ protein analyses shown in Figure 2.4, in which Ub-$Ca_V2.2$ is visibly undetectable at higher molecular weights where HA signal is strong.

We then tested to determine if e37b-dependent ubiquitinated $Ca_V2.2$ protein is preferentially targeted for degradation through the proteasome. We compared N-type currents in tsA201 cells expressing $Ca_V2.2$e[37a] or $Ca_V2.2$e[37b], in the absence and presence of MG132. As we reported previously, N-type current densities in tsA201 cells expressing $Ca_V2.2$e[37a] were significantly larger than those in cells expressing $Ca_V2.2$e[37b] (Figure 2.1B) (Bell et al., 2004; Castiglioni et al., 2006; Gray et al., 2007; Raingo et al., 2007). Only current densities in cells expressing $Ca_V2.2$e[37b] channels were however significantly enhanced by MG132. Peak N-type current densities in cells expressing $Ca_V2.2$e[37a] increased 8 % following MG132 treatment ($p = 0.10$) whereas, N-type current densities in cells expressing $Ca_V2.2$e[37b] increased by 44 % relative to control ($p = 0.016$) (Figure 2.6A, 2.6B). Our data suggest that the sequence unique to e37b supports ubiquitination of $Ca_V2.2$ protein, which normally prevents excessive surface expression.

Proteasome-dependent control of native N-type current densities in nociceptors

Our analyses of recombinant $Ca_V2.2$ channels suggest that e37b-dependent ubiquitination preferentially targets channels to the proteasome. To argue functional relevance however, we need a way to test our hypothesis on native N-type currents in neurons. We do not have antibodies to distinguish e37a and e37b splice isoforms or pharmacological tools to separate their relative contributions to N-type currents in neurons. However, we recently generated mice that lack e37a and only express e37b-containing $Ca_V2.2$ channels. We did this by homologous recombination, replacing e37a with e37b* and generating tandem e37b*-e37b exons in the *Cacna1b* gene. In these mice, the e37b* exon contains a silent mutation that removes an endogenous XhoI restriction site, which allows for verification of its expression. This silent mutation has no effect on the protein however. We refer to these mice as *Cacna1b*$^{b*b/b*b}$ (Andrade et al., 2010). In the same study, we also generated mice that lack e37b and only express e37a-containing $Ca_V2.2$ channels. These mice were however not useful for our analyses of MG132 because e37a was not able to substitute for wild-type e37b, and channels expression levels were low. Thus total $Ca_V2.2$ protein levels, along with N-type current densities, were substantially reduced relative to wild-type (Andrade et al., 2010).

Nociceptors of dorsal root ganglia normally express both e37a and e37b isoforms (Bell et al., 2004; Andrade et al., 2010), so we used these cells from wild-type (e37a and e37b expressing) and *Cacna1b*$^{b*b/b*b}$ (e37b expressing only) mice to compare the effects of MG132 on native N-type currents. We isolated N-type currents from non-N-type currents by a conotoxin-subtraction protocol (Andrade, Denome et al. 2010). This

multi-step method isolates pure N-type current and it also allows us to assess the effect of MG132 on both N-type and non-N-type currents. We measured whole cell calcium currents from nociceptors (determined based on their small size and capsaicin-responsiveness (Andrade et al., 2010)), applied 2 μM ω-conotoxin GVIA (CTx) to selectively inhibit the N-type component, measured non-N-type currents (resistant to CTx), and then determined the N-type component by offline subtraction.

We first noticed that whole cell calcium currents in nociceptors of wild type and *Cacna1b*$^{b*b/b*b}$ mice were enhanced following pretreatment with MG132, suggesting a steady state level of calcium channel degradation via the UPS. Whole cell calcium currents in wild-type and in *Cacna1b*$^{b*b/b*b}$ cells treated with MG132 increased significantly compared to control currents (30 %, p = 0.003 and 47 %, p = 0.007, respectively; not shown). By comparing the effect of MG132 on calcium currents after CTx application, we showed it enhanced non-N-type currents (CTx-insensitive) in nociceptors of wild type (58 %; p = 0.03) and *Cacna1b*$^{b*b/b*b}$ (54 %; p = 0.03) mice by the same extent (Figure 2.6C, 2.6D). N-type currents in nociceptors of *Cacna1b*$^{b*b/b*b}$ mice also increased 41 % after MG132 compared to control (p = 0.0013; Figure 2.6F), by contrast, N-type currents in nociceptors of wild-type mice that normally express significant levels of e37a-containing channels were not significantly different from control currents when treated with MG132 (p = 0.32; Figure 2.6E). Our data suggest that the majority of calcium currents, e37b-containing N-type, as well as non-N-type, are down-regulated by the UPS. They also support our conclusions from studies of cloned $Ca_V2.2$ isoforms that e37a-containing channels that are normally protected from the

influence of the UPS are functional and on the cell surface. Collectively, our analyses support the hypothesis that e37b prevents high-level functional $Ca_V2.2$ channel accumulation on the neuronal cell surface via an ubiquitin-proteasome dependent mechanism (Figure 2.7).

Discussion

We show that $Ca_V2.2$ protein is ubiquitinated and that this posttranslational modification controls N-type current density in neurons and cells by an isoform-specific mechanism. $Ca_V2.2$ may have been overlooked as a cellular target of ubiquitination in part because Ub-$Ca_V2.2$ is a minor fraction of the total $Ca_V2.2$ protein pool. The functional consequences of $Ca_V2.2$ channel ubiquitination depend on which alternative C-terminal exon, e37a or e37b, is present. E37b-dependent ubiquitinated $Ca_V2.2$ protein appears to be preferentially targeted to the proteasome and this fraction of the $Ca_V2.2$ pool contributes disproportionately to functional channels. Our findings suggest a mechanism to explain why N-type currents in cells expressing $Ca_V2.2$e[37b] clones are smaller compared to N-type currents in cells expressing $Ca_V2.2$e[37a] clones. The e37b isoform of $Ca_V2.2$ underlies the vast majority of N-type current in the nervous system suggesting that N-type current in most neurons are down-regulated by the UPS.

Consistent with our data, several groups studying both invertebrate and vertebrate preparations have shown that UPS inhibition leads to increases in synaptic efficacy, and that it has substantial presynaptic involvement (Speese et al., 2003; Bingol and Schuman, 2005; Rinetti and Schweizer, 2010). Acute inhibition of the UPS can also

enhance neurotransmission in mammalian neurons, suggesting that presynaptic proteins and synaptic transmission are dynamically influenced by ubiquitination (Rinetti and Schweizer, 2010). Our results show that N-type current density increases ~ 40 % when the UPS is inhibited, a change that could alter the efficacy of excitation-secretion coupling given the steep relationship between presynaptic calcium entry and transmitter release (Bollmann et al., 2000; Schneggenburger and Neher, 2000, 2005). A similar UPS-mediated reduction in postsynaptic AMPA receptors has a marked effect on synaptic plasticity (Colledge et al., 2003).

UBE1 interaction with e37b sequence

We were prompted to characterize the ubiquitination state of $Ca_V2.2$ splice isoforms by the unexpected interaction between e37b-sequence and UBE1 in the yeast two-hybrid protein interaction assay. Although UBE1 is not known to bind directly to substrate proteins, several observations suggest that the UBE1-$Ca_V2.2$ interaction we have identified is functionally significant, including: the specificity and reproducibility of the interaction in yeast, the increased ubiquitination of $Ca_V2.2$e[37b] over $Ca_V2.2$e[37a], and the lower current density phenotype of $Ca_V2.2$e[37b] channels, that increases, and normalizes to $Ca_V2.2$e[37a] levels after MG132 treatment. The UBE1 interaction with $Ca_V2.2$ has however not proved stable when testing full-length channel, and although UBE1 has been identified as part of the interactome of the nicotinic acetylcholine receptor ion channel (Paulo et al., 2009), indicating that UBE1 can under certain conditions associate with membrane ion channel receptors, we have no evidence for a direct interaction between $Ca_V2.2$ and UBE1.

As shown in the results, however, the UBE1-$Ca_V2.2$ interaction is specific in yeast, and this likely indicates a specific, yet indirect interaction mediated via a protein bridge, as shown for other protein-protein interactions (Rzymski et al., 2008). The high degree of conservation of structures and proteins within the ubiquitination pathways of distant organisms increases the likelihood that yeast homologues form a protein bridge between UBE1 and e37b baits (Glickman and Ciechanover, 2002; Yi and Ehlers, 2005, 2007). As all UBE1 clones isolated in our screen contain the C-terminal UFD, a region well known for its role in high affinity binding to UBE2 enzymes (Figure 2.2B) (Schulman and Harper, 2009), an E2-E3 enzyme-ligase bridge could theoretically connect the UBE1 clones to e37b baits. In an over-expression system such as the yeast two-hybrid assay, this kind of mechanism could be favored, and although the exact mechanism is unclear, the interaction ultimately indicates differential ubiquitination of full-length $Ca_V2.2$. Regardless of mechanism however, our screen led us to identify a novel isoform-specific interaction with $Ca_V2.2$ and consequently to assign new function to the proximal C-terminus of the channel.

Ubiquitinated $Ca_V2.2$ protein and the UPS

Ubiquitinated $Ca_V2.2$ protein migrates at molecular weights significantly higher, but is found at much lower levels than bulk $Ca_V2.2$ protein. E37b-dependent ubiquitinated $Ca_V2.2$ protein is likely an even smaller fraction of $Ca_V2.2$ protein, a subset of the ubiquitinated $Ca_V2.2$ pool, but it targets the channel to the UPS. The UPS down regulates functional $Ca_V2.2e$[37b] channels consistent with studies showing

ubiquitination-mediated membrane-protein internalization (Shenoy et al., 2001; Patrick et al., 2003; Yi and Ehlers, 2007; Tai and Schuman, 2008; Rotin and Staub, 2010). Although it's also possible that $Ca_V2.2e[37b]$ channels might be trafficked less efficiently to the cell surface compared to $Ca_V2.2e[37a]$ channels and/or $Ca_V2.2e[37b]$ channels might be more susceptible to UPS degradation before they reach the cell surface.

Interestingly, Dolphin and colleagues recently demonstrated ubiquitination and proteasome control of $Ca_V2.2$ channels depends on the presence of $Ca_V\beta$ subunits (Waithe et al., 2011). Similarly, Zamponi and colleagues found that $Ca_V\beta$ subunits occlude ubiquitination of $Ca_V1.2$ L-type channels that would otherwise be degraded via the proteasome and the endoplasmic reticulum-associated protein degradation complex (Altier et al., 2010). Ubiquitination of $Ca_V1.2$ depends on sequences in the C-terminus that have homology to e37b of $Ca_V2.2$, although UBE1 did not interact with this region of $Ca_V1.2$ in our yeast two-hybrid assay (Figure 2.2C).

Our results with MG132 differ from those of the Dolphin lab who find a reduction in biotinylated and presumed surface expressed $Ca_V2.2$ channels after 18 hr MG132 treatment. We, by contrast observe increased current density following 1-3 hr MG132 treatment, consistent with increased levels of surface channels. The effects of MG132 that we measured on $Ca_V2.2$ currents were very similar on currents from cloned e37b channels in tsA201 cells and on native currents in DRG neurons expressing only e37b (~ 40 % increase).

By comparing $Ca_V2.2$ splice isoforms we assign additional function to the sequence encoded by e37. Our data suggest that Y1747 in e37a occludes e37b-dependent ubiquitination of $Ca_V2.2$, and that consequently, N-type current densities in cells expressing $Ca_V2.2$e[37a] tend to be larger (Castiglioni et al., 2006; Raingo et al., 2007), and relatively insensitive to inhibition by the UPS. Many groups have shown that phosphorylation can both promote and inhibit ubiquitination of other membrane proteins (Sheng et al., 2002; Hunter, 2007; Rotin and Staub, 2010) raising the possibility that the potential phosphorylation state of Y1747 could influence ubiquitination of $Ca_V2.2$. Interestingly, we showed previously that the Y1747 to F1747 point mutation in $Ca_V2.2$e[37a] reduces N-type current densities, and abolishes $G_{i/o}$-mediated voltage-independent inhibition as if we converted the phenotype to $Ca_V2.2$e[37b] (Raingo et al., 2007). Collectively, our findings suggest that ubiquitination of $Ca_V2.2$ and $G_{i/o}$-mediated voltage-independent inhibition of $Ca_V2.2$ might converge on a common mechanism. This possibility needs to be tested; indeed others have shown that activated G protein-coupled receptors can promote ubiquitination of ion channel substrate proteins through signaling-induced E3 Ub ligase binding sites (Shukla et al., 2010).

$Ca_V2.2$ proteins are ubiquitinated by at least two pathways, one depends on e37b sequence, and one or more are independent of e37b and common to both e37a and e37b channels (Figure 2.7). Cell-specific replacement of e37b with e37a in $Ca_V2.2$ occludes e37b-dependent ubiquitination and is perhaps used to increase functional N-type channels on the cell surface. At the same time, $Ca_V2.2$ channels become more sensitive to G protein mediated voltage-independent inhibition via e37a (Raingo et al.,

2007; Andrade et al., 2010). $Ca_V2.2$ channels play a significant role in regulating excitation-secretion coupling at nerve terminals throughout the nervous system. Here we conclude that $Ca_V2.2$ is a target of cell-specific ubiquitination and a contributor to proteasome-dependent regulation of synaptic efficacy.

Methods

Molecular Biology and Cloning. $Ca_V2.2$ C-terminus baits containing e37a and e37b, were from rat clones AY211499 (Bell et al., 2004) and AF055477 (Lin et al., 1997) respectively. Short baits contained aa 1709-1816 ($37a_S$ and $37b_S$), and longer baits contained aa 1709-2038 ($37a_L$ and $37b_L$,). Human $Ca_V2.2$ II-III linker baits with e18a (II-III_1) or without e18a (II-III_2) contained aa 720-890 and aa 720-870, respectively (AF233289). C-terminal baits: 2.1-$37a_S$ and 2.1-$37b_S$ contained aa 1766-1876 from mouse $Ca_V2.1$ clones AY714490 (Richards et al., 2007) and BF731417 (respectively), 1.2-CT_S baits contained aa 1480-1585 from mouse $Ca_V1.2$ clone AY728090, and 1.3-CT_S baits contained aa 1464-1569 from rat $Ca_V1.3$ clone AF370009. All correspond to the proximal C-terminus of $Ca_V2.2$, after the final transmembrane domain ($Ca_V2.2$ aa 1709-1816). All mouse sequences translate identically to homologous rat sequences. All cDNA fragments were ligated in-frame into the pGBKT7 vector (Clontech). Construction of full-length calcium channel clones and accessory subunits were described previously (Raingo et al., 2007). The rat HA-Ub clone (in pcDNA3) was a generous gift of Pietro De Camilli.

Yeast two-hybrid screen. A Matchmaker™ Two-Hybrid System 3 (Clontech) kit was used to construct the clones and to screen. We generated a cDNA library from rat dorsal root ganglia (P5–P7) in pGADT7 (Clontech) and screened using baits $37a_S$ and $37b_S$. *S. cerevisiae* strain Y187 (mating type α) was transformed with each of the two baits, and strain AH109 (mat type a) was transformed with the prey library. Diploid yeast were plated on medium-stringency, triple drop-out media (SD/-His/-Leu/-Trp). Surviving yeast were re-streaked onto high-stringency, quadruple drop-out media (SD/-His/-Leu/-Trp/-Ade).

Immunoprecipitation and Western blot analyses. Calcium channel alpha subunits $Ca_V2.2e$[37a] or $Ca_V2.2e$[37b] together with $Ca_V\beta_3$, $Ca_V\alpha_2\delta_1$, and enhanced green fluorescent protein (eGFP) were expressed transiently in tsA201 cells as described previously (Raingo et al., 2007), with or without HA-Ub cDNAs. We harvested cells 24 to 36 hours after transfection. For IPs ~1 mg total protein lysates were incubated at 4^oC overnight with 2 µg polyclonal anti-$Ca_V2.2$ and 100 µL protein A agarose slurry (Sigma, #P3476). Westerns were performed as described previously (Andrade *et al.* 2010). Primary antibodies were: rabbit anti-$Ca_V2.2$ polyclonal (1:200; Alomone, #ACC-002), mouse anti-ubiquitin monoclonal (1:200; Cell Signaling, P4D1), goat anti-UBE1 polyclonal (1:1000; Santa Cruz), and HRP conjugated rat anti-HA monoclonal antibodies (1:7,500; Roche, clone 3F10). HRP labeled donkey α-rabbit and α-mouse IgG (Jackson cat#: 711-036-152 and 715-035-151, respectively) and donkey anti-goat IgG secondary antibodies (Jackson cat#: 705-036-147) were used at ≥1:10,000 dilution. Further details are provided in Andrade et al., 2010.

Electrophysiology- Calcium currents were recorded from tsA201 cells and acutely isolated nociceptors of dorsal root ganglia (P6-P9 mice, of either sex) using standard whole cell patch clamp methods as described previously (Raingo et al., 2007; Andrade et al., 2010). The external solution contained 1 mM $CaCl_2$ as charge carrier. The pipette solution contained (in mM) 100 CsCl, 10 EGTA, 1 EDTA, 10 HEPES, 4 MgATP, pH 7.2 with CsOH. Cells were maintained in standard growth medium (DMEM + 10% FBS) supplemented with 5 µM MG132 in 0.1 % DMSO or 0.1 % DMSO alone for control 1-3 hrs prior to recording. In neurons, ω-conotoxin GVIA (CTx) subtraction and capsaicin screening were performed as described (Bell et al., 2004; Andrade et al., 2010). All recordings were obtained at room temperature.

Figure 2.1

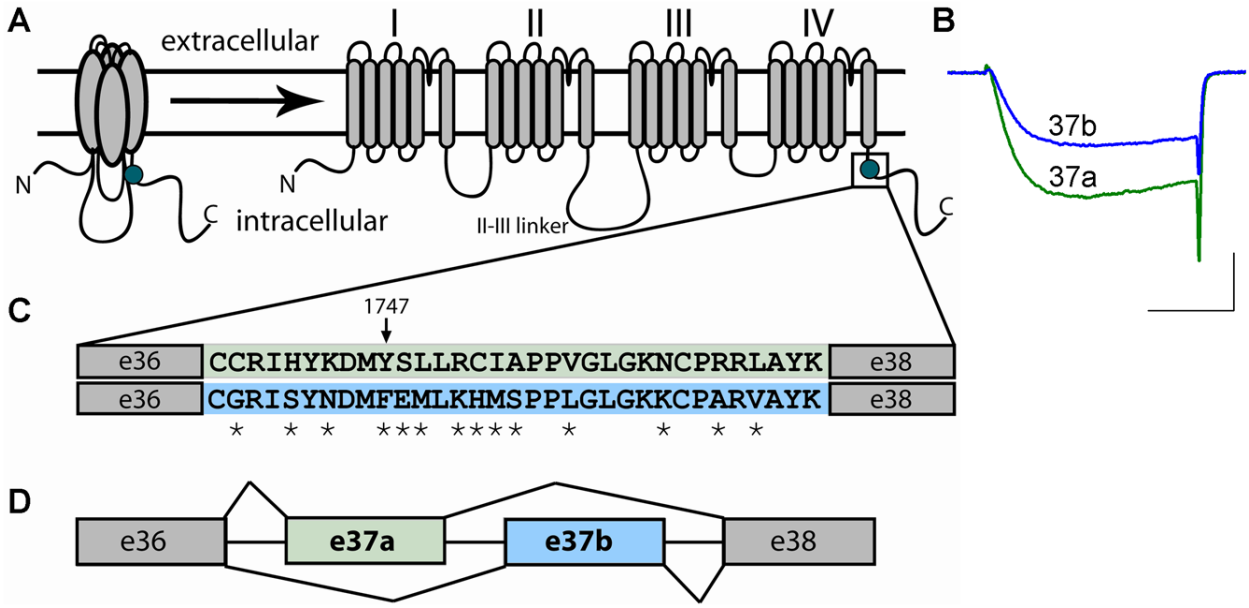
A
extracellular
I
II
III
IV
N
C
N
intracellular
II-III linker
C
B
37b
37a
C
1747
e36
CCRIHYKDMYSLLRCIAPPVGLGKNCPRRLAYK
e38
e36
CGRISYNDMFEMLKHMSPPLGLGKKCPARVAYK
e38
D
e36
e37a
e37b
e38

Figure 2.1

Mutually exclusive exons e37a and e37b of the *Cacna1b* gene encode 32 amino acids in the proximal C terminus of the $Ca_V2.2$ protein. **(*A*)** Membrane topography of $Ca_V2.2$ channel indicating the approximate location of e37a and e37b encoding sequence in the C-terminus. **(*B*)** Representative N-type currents recorded from tsA201 cells expressing 37a-containing (green) and e37b-containing (blue) $Ca_V2.2$ clones. Currents were induced by a voltage step to 5 mV from a holding potential of -100 mV. Scale bars correspond to 500 pA/pF and 10 ms. **(*C*)** Comparison of amino acid sequences encoded by e37a and e37b. Asterisks denote amino acids that are different. Arrow denotes amino acid residue 1747, a tyrosine in e37a and a phenylalanine in e37b. We have shown this amino acid is critical for functional differences between e37a- and e37b-containing $Ca_V2.2$ channels (Raingo et al., 2007). **(D)** Two patterns of alternative splicing in *Cacna1b* pre-mRNA that generates e37a and e37b containing $Ca_V2.2$ mRNAs.

Figure 2.2

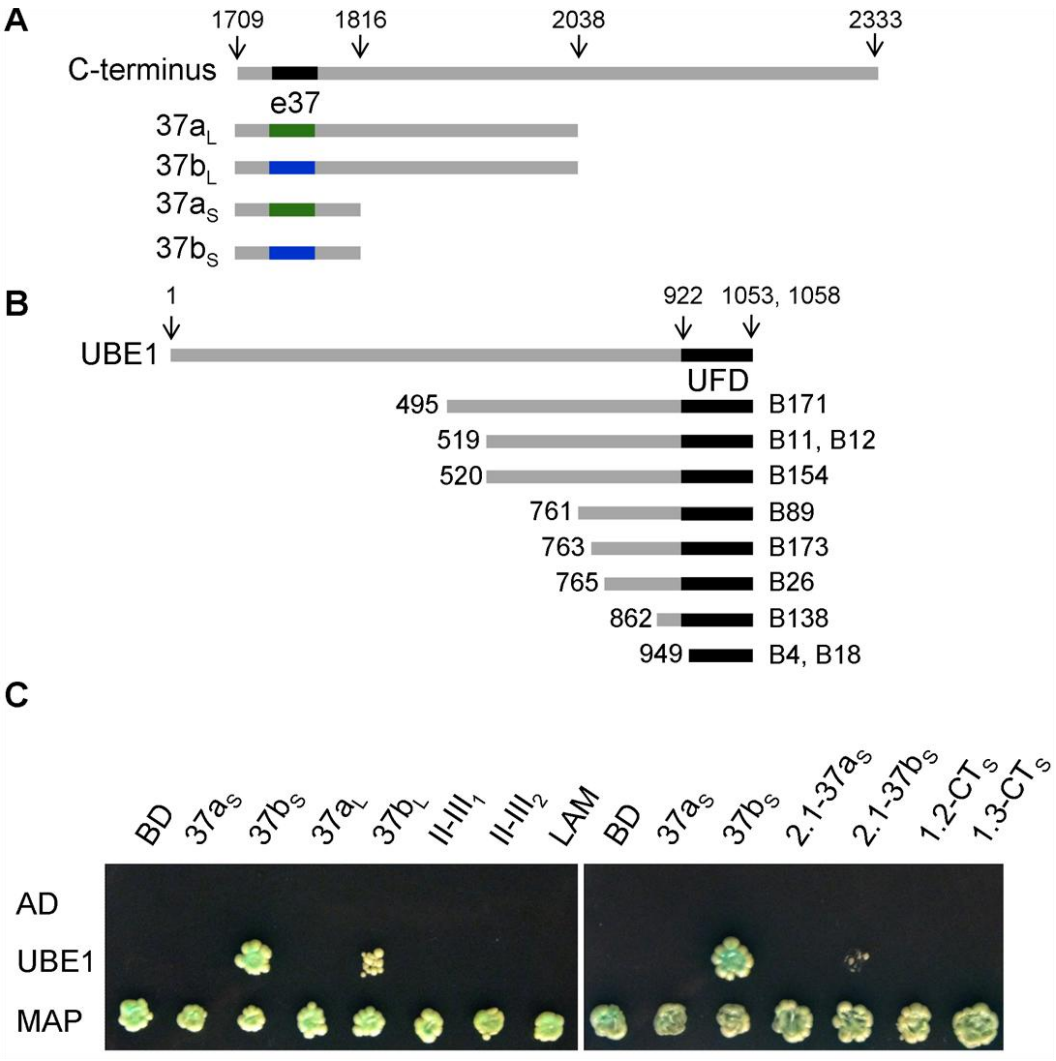
A
1709
1816
2038
2333
C-terminus
e37
37a_L
37b_L
37a_S
37b_S
B
1
922
1053, 1058
UBE1
UFD
495
B171
519
B11, B12
520
B154
761
B89
763
B173
765
B26
862
B138
949
B4, B18
C
BD
37a_S
37b_S
37a_L
37b_L
II-III_1
II-III_2
LAM
BD
37a_S
37b_S
2.1-37a_S
2.1-37b_S
1.2-CT_S
1.3-CT_S
AD
UBE1
MAP

Figure 2.2

Specific interaction between UBE1 and e37b-containing baits in yeast two-hybrid protein interaction assay. **(*A*)** $Ca_V2.2$ C-terminus baits used in yeast two-hybrid screen. All contain e37 and amino acids 1709 to 1816 (numbering according to AY211499 (Bell, Thaler et al. 2004)). The short baits end at aa 1816 ($37a_S$ and $37b_S$) and the longer baits extend to aa 2038 ($37a_L$ and $37b_L$). **(*B*)** The ubiquitin-activating enzyme E1 (UBE1;1058 amino acids) contains a ubiquitin fold domain (UFD) at its C-terminus between aa 922 and 1053 (shaded black). Individual UBE1 clones isolated from a DRG cDNA library using $37b_S$ as bait. Clone identifier numbers are included (e.g. B171). All ten UBE1 clones encode the ubiquitin fold domain. Clones B11 and B12 and clones B4 and B18 are identical in size, respectively. **(*C*)** Representative yeast colonies grown on high stringent selection media (SD/-Leu/-His/-Trp/-Ade/+X-α-gal). A matrix of pair-wise yeast two-hybrid interactions are shown. Three prey clones (left): Activation domain only (AD; pGADT7), representative UBE1 clone (UBE1; B154), and microtubule-associated protein 1A (MAP, a control for bait expression; this prey interacts with the Gal4 DNA binding domain shared by all baits). 12 co-transformant baits (top), starting with the pGBKT7 clone expressing only the Gal4 DNA binding domain (BD); followed by clones described in methods and in the main article. All constructs were transformed into *S. cerevisiae* yeast strain AH109. Three independent colonies were pooled and plated on high stringency media. All UBE1 clones tested showed similar growth patterns.

Figure 2.3

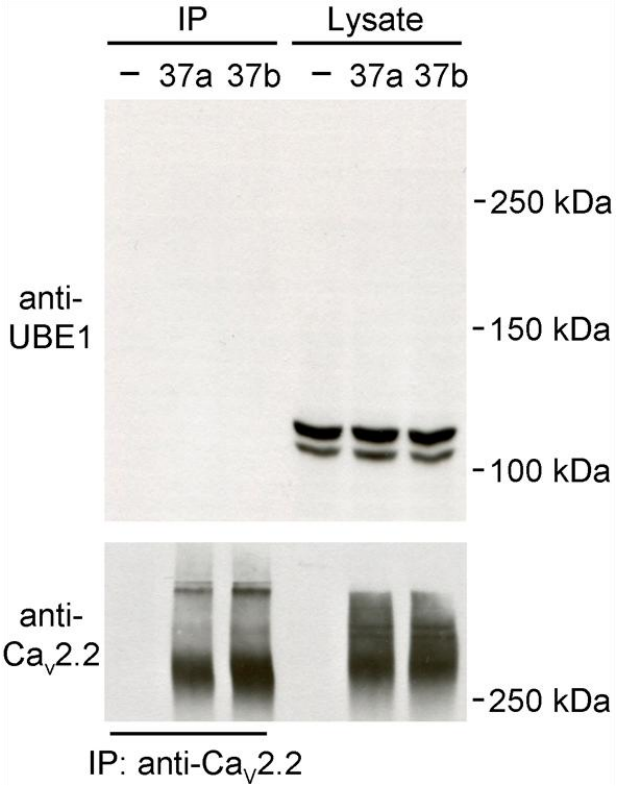
IP
Lysate
–
37a
37b
–
37a
37b
anti-
UBE1
250 kDa
150 kDa
100 kDa
anti-
Ca$_V$2.2
250 kDa
IP: anti-Ca$_V$2.2

Figure 2.3

UBE1 does not co-precipitate with $Ca_V2.2$. Representative western blots from protein preparations from tsA201 cells. Anti-UBE1 signals (*top*) in anti-$Ca_V2.2$ immunoprecipitate (*IP, lanes 1-3*) and cell lysate (*lanes 4-6*). Anti-UBE1 signals present in lysates migrate close to 110 kDa (lanes 4-6). Protein isolated from control non-transfected cells (lanes 1 and 4) and those transfected with e37a-containing $Ca_V2.2$ (lanes 2 and 5) and e37b-containing $Ca_V2.2$ (lanes 3 and 6) cDNAs. UBE1 does not co-immunoprecipitate with $Ca_V2.2$ (lanes 2-3). The same membrane was stripped and re-probed with anti-$Ca_V2.2$ (lower image). Lysate lanes (4-6) were loaded with about 3% of the sample used for each immunoprecipitation (lanes 1-3). Anti-UBE1 detects two bands that correspond to UBE1 isoforms: UBE1a and UBE1b (Stephen, Trausch-Azar et al. 1996).

Figure 2.4

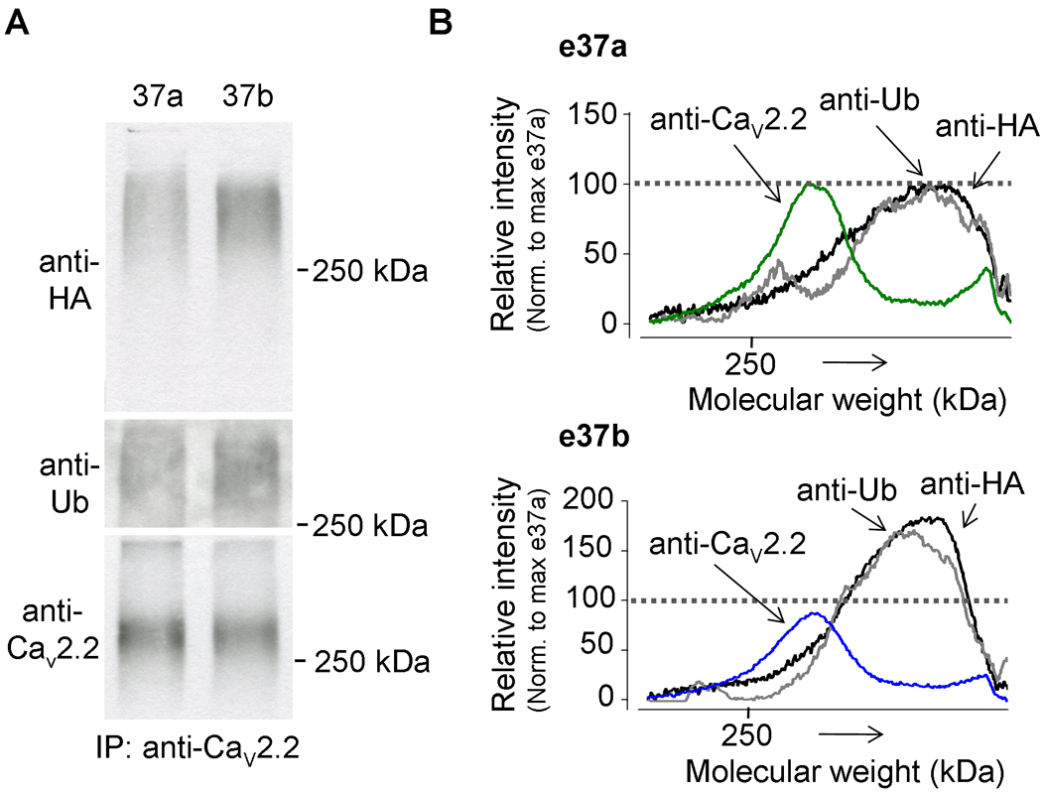
A
37a
37b
anti-HA
250 kDa
anti-Ub
250 kDa
anti-Cav2.2
250 kDa
IP: anti-Cav2.2
B
e37a
Relative intensity
(Norm. to max e37a)
150
100
50
0
anti-Cav2.2
anti-Ub
anti-HA
250
Molecular weight (kDa)
e37b
Relative intensity
(Norm. to max e37a)
200
150
100
50
0
anti-Ub
anti-HA
anti-Cav2.2
250
Molecular weight (kDa)

Figure 2.4

E37 modulates cellular ubiquitination of $Ca_V2.2$ protein. **(A)** Representative protein blots comparing cellular ubiquitination of $Ca_V2.2e$[37a] (lane 1) and $Ca_V2.2e$[37b] (lane 2) in tsA201 cells. Protein immunoprecipitated with anti-$Ca_V2.2$. Anti-HA signal (top), anti-Ub signal on same membrane as above stripped and re-probed (middle), and anti-$Ca_V2.2$ signal on same membrane as above stripped and re-probed (lower), in this order. **(*B*)** Relative signal intensity plotted against protein mobility from analyses of blots shown in *A* (ImageJ densitometry software). Anti-HA (black), anti-Ub (gray), and anti-$Ca_V2.2$ (green and blue) signals from cells expressing $Ca_V2.2e$[37a] (top) and $Ca_V2.2e$[37b] (lower). Signal intensities were normalized to the peak $Ca_V2.2e$[37a] signals for comparison.

Figure 2.5

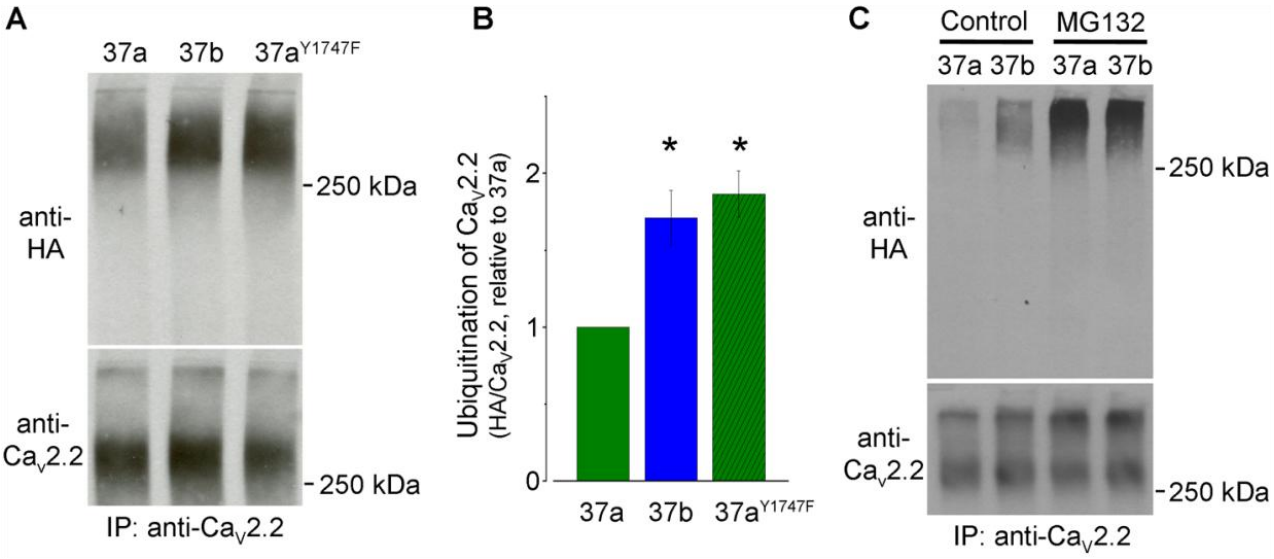
A
37a
37b
37a^{Y1747F}
anti-HA
anti-$Ca_V2.2$
250 kDa
250 kDa
IP: anti-$Ca_V2.2$
B
Ubiquitination of $Ca_V2.2$ (HA/$Ca_V2.2$, relative to 37a)
0
1
2
*
*
37a
37b
37a^{Y1747F}
C
Control
MG132
37a 37b 37a 37b
anti-HA
anti-$Ca_V2.2$
250 kDa
250 kDa
IP: anti-$Ca_V2.2$

Figure 2.5

Phenylalanine 1747 controls ubiquitination of $Ca_V2.2$ protein. $Ca_V2.2$ and HA-ubiquitin cDNA clones expressed in tsA201 cells to compare ubiquitination states of $Ca_V2.2$ splice isoforms. **(*A*)** Representative blots compare cellular ubiquitination of $Ca_V2.2e[37a]$, $Ca_V2.2e[37b]$, and $Ca_V2.2e[37a]^{Y1747F}$ protein immunoprecipitated with anti-$Ca_V2.2$. Anti-HA signals (*upper*) and anti-$Ca_V2.2$ signals from same membrane stripped and re-probed (*lower*). **(*B*)** Averaged, normalized anti-HA signal quantified by densitometry from three independent transfections. Anti-HA signal intensities normalized to total $Ca_V2.2$ protein in each experiment, and then plotted relative to the $Ca_V2.2e[37a]$ signal for comparison. HA signal relative to the $Ca_V2.2e[37a]$-associated signal was 1.87 ± 0.15 ($p = 0.017$, $n = 3$) and 1.71 ± 0.18 ($p = 0.005$, $n = 3$) for $Ca_V2.2e[37a]^{Y1747F}$ and $Ca_V2.2e[37b]$, respectively. ***C*)** Representative protein blots comparing anti-HA signal in protein preps from cells expressing $Ca_V2.2e[37a]$ and $Ca_V2.2e[37b]$ in the absence and presence of 10 µM MG132 (3hr incubation in DMEM + FBS). HA signal (*upper*) and $Ca_V2.2$ signal from the same membrane stripped and re-probed (*lower*). Errors are ± s.e.m.

Figure 2.6

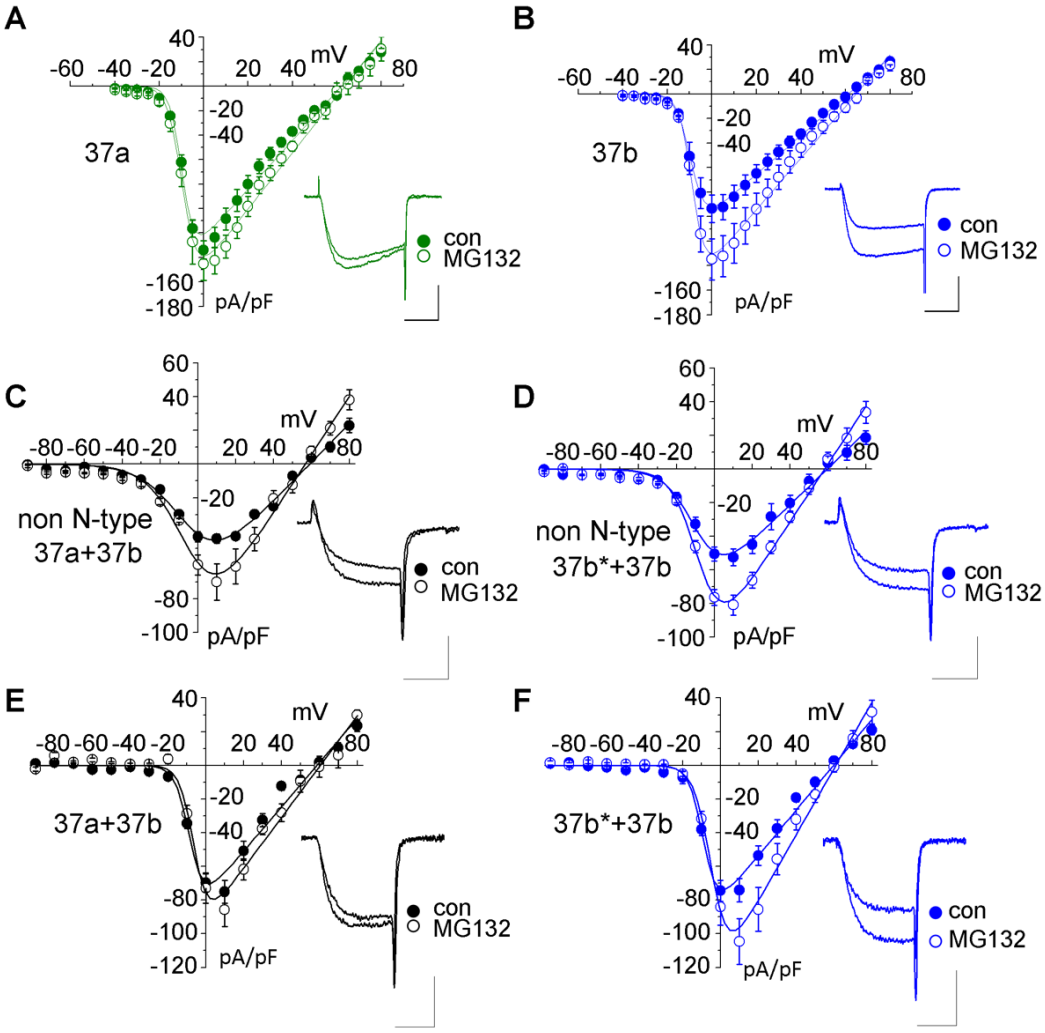
A
37a
mV
pA/pF
con
MG132
B
37b
C
non N-type
37a+37b
D
non N-type
37b*+37b
E
37a+37b
F
37b*+37b

Figure 2.6

Proteasome inhibition preferentially increases N-type current densities in cells expressing $Ca_V2.2e[37b]$ compared to $Ca_V2.2e[37a]$. **(*A, B*)** Averaged current voltage relationships for N-type currents recorded in tsA201 cells expressing recombinant $Ca_V2.2e[37a]$ **(*A*)** and $Ca_V2.2e[37b]$ **(*B*)** in control (solid circles) and after preincubation with 5 µM MG132 for 3 hours (open circles). Averaged peak current densities for $Ca_V2.2e[37a]$ were -133.9 ± 7.4 pA/pF, n=11 in control and -145.2 ± 13.4 pA/pF, n=10, after MG132 (p = 0.10) and for $Ca_V2.2e[37b]$ were -93.5 ± 11.3 pA/pF, n=11 in control cells and -134.7 ± 16.8 pA/pF, n=11, after MG132 treatment (p = 0.016; student's t-test). Scale bars correspond to 500 pA/pF and 10 ms. **(*C-F*)** Average current voltage relationships for non-N-type currents **(*C, D*)** and N-type current **(*E, F*)** in nociceptors from wild-type mice **(*C, E*)** and from *CACNA1B*$^{e37b*/e37b}$ mice **(*D, F*)** in control cells (closed circles) and after pre-treated with 5 µM MG132 for 1 hr (open circles). Non-N-type currents (ω-conotoxin GVIA-resistant) in nociceptors of wild-type and *CACNA1B*$^{e37b*/e37b}$ mice are not significantly different after MG132 treatment (p = 0.37; student's t-test). **(*C*)** Average, peak non N-type currents in wild type (e37a + e37b) mice were -44.4 ± 2.8 pA/pF in control and -70.1 ± 10.9 pA/pF after MG132 treatment, and **(*D*)** in *Cacna1b*$^{b*b/b*b}$ (e37b only) mice were -52.5 ± 5.1 pA/pF in control and -81.0 ± 5.9 pA/pF after MG132. **(*E*)** Average, peak N-type currents densities in wild-type (37a + e37b) mice were -75.1 ± 6.8 pA/pF, n = 6 in control and -85.8 ± 10.0 pA/pF, n = 13, after MG132 treatment (p = 0.32) and **(*F*)** in *Cacna1b*$^{b*b/b*b}$ (e37b only) mice were -74.5 ± 6.2 pA/pF, n = 7, in control and -104.5 ± 13.5 pA/pF, n = 13, after MG132 (p = 0.0013; student's t-test). Control currents were recorded in the presence of 0.01% DMSO

vehicle only. Representative non N-type and N-type currents are shown. Scale bars in C, D, E, F correspond to 50 pA/pF and 5 ms. Errors are ± s.e.m.

Figure 2.7

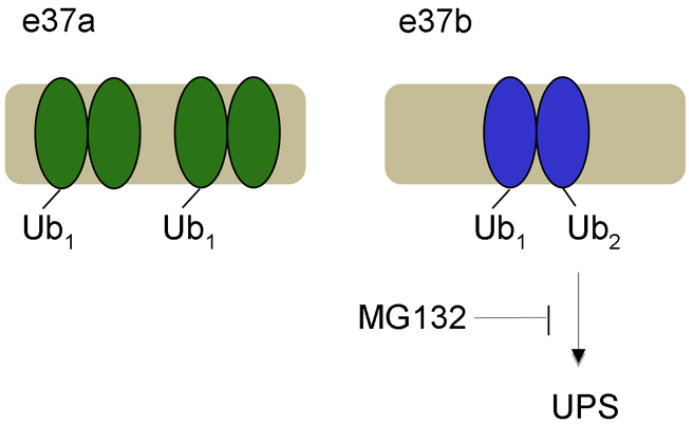

Figure 2.7

Differential ubiquitination of e37a and e37b affects functional $Ca_V2.2$ expression. Model illustrates functionally active surface $Ca_V2.2$ channel isoforms, e37a and e37b. Two sites of ubiquitination are shown. One site is common to e37a and e37b isoforms (Ub_1) whereas the second site (Ub_2) is unique to e37b. Ub_2 modification targets $Ca_V2.2$ channels to the ubiquitin proteasome system (UPS). Ub_2 reduces the level of functional $Ca_V2.2$ channels at the cell surface, a process that can be inhibited by MG132. We cannot distinguish if Ub_2 promotes internalization of functional surface $Ca_V2.2$ channels, or if Ub_2 inhibits surface membrane trafficking.

CHAPTER 3

NOVEL $Ca_V2.2$ KNOCK-IN MICE REVEAL ISOFORM-SPECIFIC RESPONSE TO MORPHINE

All authors contributed equally to writing the original work. This work has been adapted from the original article to fit this thesis format.

This chapter has been published as: Andrade A, Denome S, Jiang YQ, **Marangoudakis S**, Lipscombe D. (2010). Opioid inhibition of N-type Ca^{2+} channels and spinal analgesia couple to alternative splicing. *Nature Neuroscience*. Oct;13(10):1249-56.

I performed the protein analyses in Figures 3.3b,c, 3.4, 3.9

Arturo Andrade performed the electrophysiology in Figures 3.3a, 3.5, 3.6 and 3.7

Sylvia Denome was responsible for generating and breeding the transgenic mice, as well as performing the DNA and RNA analyses in Figures 3.1, 3.2 and Table 3.1

Yu-Qui Jiang performed the behavioral work in Figure 3.8

Acknowledgements

We thank J. Kysik and E. Paul in the mouse transgenic facility at Brown University. This work was supported by US National Institutes of Health grants RO1NS055251 (D.L.), F31NS066702 (S.M.) and P20RR015578 (Transgenic Facility at Brown University)

Abstract

Alternative pre-mRNA splicing occurs extensively in the nervous systems of complex organisms, including humans, considerably expanding the potential size of the proteome. Cell-specific alternative pre-mRNA splicing is thought to optimize protein function for specialized cellular tasks, but direct evidence for this is limited. Transmission of noxious thermal stimuli relies on the activity of N-type $Ca_V2.2$ calcium channels in nociceptors. Using an exon-replacement strategy in mice, we show that mutually exclusive splicing patterns in the $Ca_V2.2$ gene modulate N-type channel function in nociceptors, leading to a change in morphine analgesia. Exon 37a (e37a) enhances μ-opioid receptor–mediated inhibition of N-type calcium channels by promoting activity-independent inhibition. In the absence of e37a, spinal morphine analgesia is weakened *in vivo* but the basal response to noxious thermal stimuli is not altered. Our data suggest that highly specialized, discrete cellular responsiveness *in vivo* can be attributed to alternative splicing events regulated at the level of individual neurons.

Introduction

Alternative pre-mRNA splicing is used extensively in the nervous systems of complex organisms, including humans (Lipscombe, 2005; Ule and Darnell, 2006; Li et al., 2007). Transcriptome analyses suggest that alternative pre-mRNA splicing events occur in the vast majority of multi-exon human genes (Pan et al., 2008). Furthermore, an increasing number of human diseases are linked to defects in alternative splicing (Dredge et al., 2001). Neurons are thought to use alternative splicing to add and subtract discrete protein modules encoded by alternative exons, optimizing protein function for specific cellular tasks. There is evidence that cell-dependent inclusions of alternatively spliced exons in ion channels and receptors act like molecular switches, permitting new interactions that control channel gating and receptor targeting (Mu et al., 2003; Lipscombe, 2005; Raingo et al., 2007). However, there are few studies linking a specific splicing event in an identified population of neurons to changes in native protein function and behavior (Lipscombe, 2005; Li et al., 2007). The challenge is perhaps greatest in the nervous system, where a heterogeneous population of neurons express a vast number of multi-exon genes (Li et al., 2007; Chen and Manley, 2009). Here we study the function of one site of alternative splicing in the *Cacna1b* gene, which encodes the pore-forming subunit of the N-type channel.

Ion channels underlie all electrical signals in the nervous system (Hille, 2001). They are highly sensitive to perturbations in their structure or chemical environment. Moreover, these changes can be monitored with precision. Studies of ion-channel splice isoforms have shown that alternatively spliced exons in ion channels can modify plasma mem-

brane and subcellular targeting and trafficking, second-messenger sensitivities and channel gating properties (Xie and Black, 2001; Mu et al., 2003; Lipscombe, 2005).

Alternatively spliced exons in genes encoding voltage-gated calcium channels have been shown to have tissue-specific expression patterns and to modify channel activity and drug sensitivity (Bourinet et al., 1999; Lipscombe, 2005; Zhong et al., 2006; Raingo et al., 2007; Mich and Horne, 2008; Adams et al., 2009; Liao et al., 2009). But there are little data on the cellular consequences in neurons and none on the behavioral consequences of regulated alternative splicing events. We have focused on *Cacna1b*, the gene encoding the presynaptic calcium channel $Ca_V2.2$, which is the core of the N-type calcium channel. In particular, we focus on a pair of mutually exclusive exons in $Ca_V2.2$ mRNA, e37a and e37b, which encode 33 amino acid residues in the proximal region of the protein's C terminus. Fourteen of the 33 residues differ between e37a and e37b. E37a has an intriguing expression profile: $Ca_V2.2e[37a]$ mRNAs are enriched in nociceptors of dorsal root ganglia (DRG) and expressed at lower levels in other regions, including brain, while $Ca_V2.2e[37b]$ mRNAs are ubiquitous in the nervous system (Bell et al., 2004; Castiglioni et al., 2006). By studying clones of $Ca_V2.2$ splice isoforms expressed in a mammalian cell line, we have previously shown that e37a creates an inhibitory domain in the $Ca_V2.2$ protein that renders N-type calcium channels sensitive to a form of $G_{i/o}$ protein–dependent inhibition that persists when cells are depolarized (Raingo et al., 2007). We have also found that e37a promotes greater N-type current density (Bell et al., 2004; Castiglioni et al., 2006). *In vivo* silencing of $Ca_V2.2e[37a]$ reduces basal thermal nociception, suggesting this isoform participates in transmission

at C-fiber terminals (Altier et al., 2007). But the role of $Ca_V2.2e[37a]$ channels in $G_{i/o}$ protein inhibition of native N-type channels in the pain pathway remains unexplored.

With this in mind, we devised a mouse model to determine why $Ca_V2.2e[37a]$ channels are enriched in nociceptors of DRG. We eliminated e37a from the mouse *Cacna1b* gene and replaced it with a second 37b-encoding exon. By comparing these mice to wild-type mice that express both e37a and e37b isoforms, we show that e37a regulates μ-opioid receptor–mediated inhibition of native N-type calcium channels in nociceptors and that spinal-level analgesia by morphine *in vivo* is reduced in the absence of e37a by a mechanism that does not affect basal transmission of noxious thermal stimuli.

Results

Exon substitution in the *Cacna1b* mouse gene

To determine how e37a affects N-type calcium channel activity *in vivo*, we chose an exon-substitution strategy aimed at eliminating the $Ca_V2.2e[37a]$ splice isoform while preserving cell-directed splicing and N-type channel expression. Figure 3.1 illustrates our approach. E37a and e37b are mutually exclusive and identical in size, and can substitute for each other structurally and, in part, functionally. We replaced e37a in the mouse *Cacna1b* gene with an e37b sequence (e37b*), creating tandem 37b exons (*Cacna1b*$^{b*b/b*b}$) and eliminating e37a; we also generated mice expressing e37a only (*Cacna1b*$^{aa*/aa*}$) by the same strategy, replacing e37b in *Cacna1b* with e37a sequence (e37a*) (Figure 3.1 and Figure 3.2). Correct *Cacna1b* targeting was verified by genomic PCR (Figure 3.2) and sequencing. Mice homozygous for each mutation, *Cacna1b*$^{b*b/b*b}$ and *Cacna1b*$^{aa*/aa*}$, were viable and fecund. *Cacna1b*$^{b*b/b*b}$ homozygotes were born at

wild-type frequencies, but *Cacna1b*$^{aa*/aa*}$ homozygotes were born at ~50% of the expected Mendelian rate (Table 3.1). Our data suggest that *Cacna1b*$^{b*b/b*b}$ homozygotes tolerate e37b* as a replacement exon for e37a, whereas *Cacna1b*$^{aa*/aa*}$ homozygotes are physiologically compromised. These results point to a global disruption of N-type calcium channel function (Table 3.1).

To distinguish mutant (e37a* and e37b*) from wild-type expressed sequences (e37a and e37b) we introduced synonymous point mutations. We eliminated the BsrGI restriction site in e37a and the XhoI restriction site in e37b. A combination of reverse-transcription PCR (RT-PCR) and restriction digest analysis showed that e37b*- and e37a*-containing mRNAs were expressed in DRG of mutant mice (Figure 3.1b,c and Figure 3.2).

Alternative splicing patterns were comparable for *Cacna1b*$^{b*b/b*b}$ and wild-type mice in DRG. Although not quantitative, our PCR analyses suggest that the proportion of e37b* in mutants was similar to that of e37a in wild-type DRG (Figure 3.1c). Similarly, the proportion of e37b-derived RT-PCR products amplified in mutants was comparable to that of e37b-derived products in wild-type DRG (Figure 3.1c). These results, combined with our previous studies in rat, suggest that e37a-containing mRNAs are enriched in DRG relative to other parts of the nervous system but $Ca_V2.2$e[37b] mRNAs still represent the most common $Ca_V2.2$ isoform in RNA of whole DRG (Bell et al., 2004; Castiglioni et al., 2006).

In contrast, expression patterns of $Ca_V2.2e[37a]$ and $Ca_V2.2e[37a*]$ mRNAs in DRG of *Cacna1b*$^{aa*/aa*}$ mice are different from those in wild-type mice (Figure 3.1c). First, from *Cacna1b*$^{aa*/aa*}$ DRG we amplified a PCR product of 335 base pairs (bp) that was resistant to both XhoI and BsrGI cleavage (Figure 3.1c). DNA sequence analysis showed this cDNA product was amplified from $Ca_V2.2$ mRNAs that lacked exon 37 (Δ37; Figure 3.1b). We know from our previous analyses that $Ca_V2.2$ mRNAs lacking both e37a and e37b create a shift in the reading frame, an early stop codon, and nonfunctional $Ca_V2.2$ protein (Pan and Lipscombe, 2000). Second, the relative abundances of e37a- and e37a*-containing $Ca_V2.2$ mRNAs in DRG of *Cacna1b*$^{aa*/aa*}$ mice are different from those of $Ca_V2.2e[37a]$ and $Ca_V2.2e[37b]$ mRNAs in wild-type mice (Figure 3.1c). Below we show that N-type currents and $Ca_V2.2$ protein levels in DRG of *Cacna1b*$^{aa*/aa*}$ mice are also substantially reduced relative to wild-type mice.

Ca^{2+} currents in DRG of *Cacna1b*$^{b*b/b*b}$ and wild type mice

We have previously reported that $Ca_V2.2e[37a]$ mRNAs are enriched in DRG, specifically in small-diameter nociceptors defined by their capsaicin sensitivity (Bell et al., 2004). We have also shown in a mammalian expression system that e37a promotes voltage-independent inhibition of N-type currents through μ-opioid receptor activation (Raingo et al., 2007). To test the role of e37a in mediating inhibition of native N-type current in capsaicin-responsive small-diameter neurons of DRG, we first distinguished these neurons from two other classes of neurons (large and T-rich). We did this by assessing capsaicin sensitivity, cell capacitance (size) and calcium channel properties.

Small neurons had small membrane capacitances tightly distributed around an average value of 13 pF. These were readily separable from large neurons (37 pF). We found the vast majority of small neurons were capsaicin responsive (17 of 21), whereas large neurons rarely responded to capsaicin (1 of 19). A third group of neurons (T-rich (Nelson et al., 2005)) expressed large T-type calcium currents that characteristically activate at low voltages and deactivate with slow kinetics. These were intermediate in size and did not respond to capsaicin, but by virtue of their large T-type currents they were easily identified and separated from small and large neurons (not shown).

Whole-cell calcium currents from *Cacna1b*$^{b*b/b*b}$ mice were indistinguishable from those in wild type mice (*Cacna1b*$^{ab/ab}$; Figure 3.3). DRG neurons express at least four different classes of calcium channels, N-type, P/Q-type, L-type and T-type; N-type represents the largest component (Taddese et al., 1995; Bell et al., 2004; Nelson et al., 2005). We isolated pure N-type from non–N-type currents using the N-type calcium channel blocker 2 μM ω-conotoxin GVIA and found that N-type currents in DRG neurons of *Cacna1b* $^{b*b/b*b}$ mice were also indistinguishable from the wild type (Figure 3.5)). These data support our RT-PCR analyses that show e37b* can substitute for e37a and support wild-type splicing patterns in DRG neurons.

N-type Ca^{2+} currents in aa* mice are smaller than in wild type

In contrast to *Cacna1b*$^{b*b/b*b}$, N-type currents in small and large neurons of *Cacna1b* $^{aa*/aa*}$ mice were significantly smaller than in wild-type mice (Student's *t*-test, *P* = 0.000238; Figure 3.5a). $Ca_V2.2$ protein levels in DRG (Figure 3.3b) and in brains (Figure 3.4) of *Cacna1b* $^{aa*/aa*}$ mice were reduced relative to wild-type mice. This reduction was specific to $Ca_V2.2$ protein and did not lead to compensatory changes in levels of the

closely related $Ca_V2.1$ protein in brains of *Cacna1b* $^{aa*/aa*}$ mice (Figure 3.4). The reduction in $Ca_V2.2$ protein levels in DRG of *Cacna1b* $^{aa*/aa*}$ mice could not be explained by differences in cell size; whole-cell capacitance values within each subset of neurons were indistinguishable among genotypes. Furthermore, we compared calcium current densities (pA pF^{-1}) to normalize for cell size (Figures 3.3a and 3.5). N-type currents in DRG neurons from *Cacna1b*$^{aa*/aa*}$ mice activated at voltages ~7 mV more hyperpolarized than the voltages at which N-type currents were activated in neurons of wild-type and *Cacna1b* $^{b*b/b*b}$ mice (Figure 3.5a). Our findings are highly consistent with our previous studies of cloned e37a-containing N-type channels expressed in mammalian and amphibian cells. These similarly activated at voltages ~7 mV more hyperpolarized than e37b-containing N-type channels (Bell et al., 2004; Castiglioni et al., 2006; Raingo et al., 2007).

The reduction of $Ca_V2.2$ protein levels in *Cacna1b*$^{aa*/aa*}$ mice probably results from a disruption in alternative splicing, consistent with the data from e37a-lacking $Ca_V2.2$ mRNAs in DRG (Figure 3.1c). We next compared G protein inhibition of N-type currents in small-diameter nociceptors from our various mouse lines, but with our primary focus on *Cacna1b* $^{b*b/b*b}$ and wild-type recordings, because $Ca_V2.2$ protein levels are reduced in *Cacna1b*$^{aa*/aa*}$ mice.

DAMGO inhibits Ca^{2+} currents in all genotypes similarly

In previous studies of cloned $Ca_V2.2e[37a]$ and $Ca_V2.2e[37b]$ channels in a mammalian cell line, we have shown that e37a-containing N-type channels promote voltage-

independent inhibition of N-type currents via G protein–coupled receptors without affecting overall inhibition of peak current (Raingo et al., 2007). We next tested whether e37a regulates the responsiveness of native N-type currents to μ-opioid receptor–mediated inhibition in nociceptors that express both $Ca_V2.2e[37a]$ and $Ca_V2.2e[37b]$ mRNAs under normal circumstances (Bell et al., 2004).

We used a saturating concentration of the opioid peptide DAMGO (10 μM) to activate μ-opioid receptors and monitored the effects on N-type and non–N-type currents in nociceptors of *Cacna1b* $^{b*b/b*b}$ and wild-type mice (Figure 3.6). Overall, we found DAMGO was a more effective inhibitor of N-type (70–75%) than of non–N-type (15–25%) current, as reported elsewhere (Taddese et al., 1995). DAMGO inhibited N-type current amplitudes in nociceptors from *Cacna1b* $^{b*b/b*b}$ and wild-type mice equally (P = 0.64; Figure 3.6f). Similarly, the efficacy of DAMGO on N-type currents in small neurons of *Cacna1b*$^{aa*/aa*}$ mice was not significantly different from its efficacy in wild-type mice (P = 0.49; Figure 3.6f).

E37a promotes voltage-independent inhibition by DAMGO

If e37a does not influence the overall inhibitory action of DAMGO, does it affect the type of inhibition? To answer this question, we next tested whether e37a was important for voltage-independent inhibition of N-type currents by DAMGO.

We used standard strong, brief, suprathreshold depolarizations to 80 mV just before the test pulse to remove voltage-dependent inhibition mediated by saturating concentrations

of DAMGO (Figure 3.7). This allowed us to calculate the relative amounts of voltage-dependent and voltage-independent inhibition of non–N-type and N-type currents (Figure 3.7g,h). DAMGO inhibited non–N-type currents by voltage-dependent and voltage-independent mechanisms, and the relative contribution of each was the same in neurons of wild-type, *Cacna1b* $^{b*b/b*b}$ and *Cacna1b*$^{aa*/aa*}$ mice (70% voltage-independent; Figure 3.7d–f,h).

However, we observed substantial differences when we compared DAMGO's effects on N-type currents in nociceptors of *Cacna1b* $^{b*b/b*b}$ mice compared with wild-type mice (P = 0.032; Figure 3.7g). Even though peak N-type currents in nociceptors of all three genotypes were inhibited equally well by DAMGO (Figure 3.6), its inhibitory effects were mostly voltage-dependent in neurons of *Cacna1b* $^{b*b/b*b}$ mice (75% voltage-dependent; Figure 3.7b,g), in contrast to wild-type mice (50% voltage-dependent; Figure 3.7a,g). In other words, DAMGO caused significantly less voltage-independent inhibition of N-type currents in nociceptors of *Cacna1b*$^{b*b/b*b}$ mice. It was only in nociceptors of *Cacna1b*$^{b*b/b*b}$ mice that we observed a shift from voltage-independent toward voltage-dependent inhibition of N-type currents; DAMGO's effects on N-type currents in nociceptors of *Cacna1b*$^{aa*/aa*}$ mice (Figure 3.7c,g) and on non–N-type currents in *Cacna1b* $^{b*b/b*b}$ and *Cacna1b*$^{aa*/aa*}$ mice (Figure 3.7e,f,h) were the same as in wild-type mice. This is generally consistent with our studies of cloned $Ca_V2.2$e[37a] and $Ca_V2.2$[e37b] channels expressed in tsA201 cells (Raingo et al., 2007).

E37a influences spinal-level analgesia by morphine

Our electrophysiological analyses show that e37a promotes a form on N-type channel inhibition in nociceptors that is resistant to depolarization (voltage independent). We next used our mouse models to test the role of e37a in (i) basal nociception and (ii) spinal analgesia by morphine. Small capsaicin-responsive nociceptors transmit information about noxious thermal stimuli. Intrathecal morphine, acting through μ-opioid receptors, inhibits transmission in this pathway (Glaum et al., 1994; Scherrer et al., 2009). At least part of morphine's spinal-level analgesia is through μ-opioid receptor–mediated inhibition of presynaptic N-type channels on nociceptor terminals in the dorsal horn of the spinal cord (Bao et al., 1998; Williams et al., 2001). To assess this pathway, we applied standard thermal stimuli to the hind paw and measured paw-withdrawal latencies in all three mouse lines. This behavioral test specifically assesses spinal-level circuits (Hargreaves et al., 1988; Wilson and Mogil, 2001). Paw-withdrawal latencies measured from wild-type, *Cacna1b* $^{b*b/b*b}$ and *Cacna1b* $^{aa*/aa*}$ mice were the same (Figure 3.8a). Our data suggest that amino acid residues unique to e37a are not necessary for normal transmission of noxious thermal stimuli.

Finally, we tested whether e37a contributes to the analgesic actions of intrathecal morphine. This route of administration restricts the site of morphine action to the spinal cord and rules out contributions from supraspinal sites (Hylden and Wilcox, 1980; Wang et al., 2000). At doses higher than 3 μg, morphine induced behavior that interfered with testing. At its peak, 3 μg morphine induced analgesia to a level 70% of the maximum possible effect against the thermal stimulus, similar to other reported results (Marker et

al., 2005). We found substantial differences in the analgesic efficacy of intrathecal morphine in *Cacna1b* $^{b*b/b*b}$ mice compared with wild-type mice (Figure 3.8b–c). As reported (Wang et al., 2000), intrathecal morphine transiently lengthened latencies of paw withdrawal in response to thermal stimuli. Overall, morphine was 30% less effective as an analgesic at 3 µg in *Cacna1b* $^{b*b/b*b}$ than in wild-type mice (n = 20, Student's two-tailed t-test, P = 0.004; Figure 3.8b). By comparison, morphine was similarly effective at prolonging paw-withdrawal latencies in *Cacna1b*$^{aa*/aa*}$ and wild-type mice (n = 14, P = 0.77; Figure 3.8b). We compared the time courses of morphine-induced analgesia in *Cacna1b* $^{b*b/b*b}$, *Cacna1b*$^{aa*/aa*}$ and wild-type mice (Figure 3.8c,d). The analgesic effect of 3 µg morphine was apparent within 10 min and peaked at 20–30 min; the effect was reduced in *Cacna1b*$^{b*b/b*b}$ mice at all time points tested. These differences are significant at 20, 30, 50 and 60 min (Student's two-tailed t-test, P = 0.008–0.044; Figure 3.8c). Our data suggest that e37a is needed for the maximal spinal-level analgesic actions of morphine in response to noxious thermal stimuli.

Discussion

Cell-directed alternative pre-mRNA splicing is thought to represent an important step in optimizing protein function for specialized tasks, but few if any studies have linked a single splicing event to a specific behavior in mammals (Lipscombe, 2005; Li et al., 2007). We used an exon-replacement strategy to show that it is possible to attribute a decrease in the efficacy of morphine to a single RNA processing event. We suggest that cell-specific selection of e37a during alternative pre-mRNA splicing enhances activity-independent G protein inhibition of N-type calcium channels in nociceptors. The

enrichment of e37a in nociceptors may augment the analgesic actions of morphine *in vivo.*

Intrathecal morphine may need e37a for maximal efficacy

Our approach took advantage of a localized splicing event in a well-described population of functionally specialized neurons, which underlie a behavior that can be measured reliably. Capsaicin-responsive small-diameter nociceptors of unmyelinated C-fibers are specialized to transmit noxious thermal stimuli (Costigan et al., 2009; Scherrer et al., 2009). N-type $Ca_V2.2$ calcium channels at presynaptic terminals of C-fiber afferents in the spinal cord mediate transmitter release and behavioral responses to noxious stimuli (Bowersox et al., 1996). Morphine occludes transmission of noxious thermal stimuli in the spinal cord in large part by μ-opioid receptor–mediated inhibition of presynaptic N-type channels at nociceptor terminals (Malmberg and Yaksh, 1995; Bowersox et al., 1996; Matthews and Dickenson, 2001; Scott et al., 2002; Altier and Zamponi, 2004). By comparing behavioral responses in *Cacna1b*$^{b*b/b*b}$ and wild-type mice, we have obtained evidence that maximal analgesic actions of intrathecal morphine may depend on e37a-containing $Ca_V2.2$ channels (Figure 3.8). Collectively, our studies support the hypothesis that e37a boosts the analgesic effects of morphine via its influence on μ-opioid receptor–mediated inhibition of N-type calcium channels. E37a selectively augments voltage-independent inhibition of N-type currents without affecting the overall level of current inhibition (Figures 3.6, 3.7, 3.8). Our conclusions about the role of e37a from the present studies on native channels and receptors are reinforced by our previous studies of cloned $Ca_V2.2$ isoforms and receptors expressed in the tsA201 cell line (Raingo et al., 2007).

Our analyses of *Cacna1b*$^{b*b/b*b}$ and wild-type mice suggest that, at higher doses, about 30% of morphine's analgesic actions at the level of the spinal cord rely on e37a-dependent inhibition of N-type channels. E37a-independent actions of morphine probably include voltage-dependent and voltage-independent inhibition of N-type calcium channels, and postsynaptic GIRK potassium channel activation via μ-opioid receptors (Marker et al., 2005). Notably, the GIRK-dependent component of spinal analgesia by morphine is similar in magnitude and is engaged at the same concentration of morphine as we report for e37a (Marker et al., 2005).

Paw-withdrawal latencies to noxious thermal stimuli were indistinguishable among genotypes, suggesting that $Ca_V2.2e[37a]$ and $Ca_V2.2[e37b]$ channels support transmission of nociceptive information in the spinal cord equally well. By contrast, studies using isoform-specific small interfering RNA suggest that $Ca_V2.2e[37a]$ channels have a preferred role in transmission of noxious thermal stimuli (Altier et al., 2007), in apparent contradiction to our analyses of *Cacna1b*$^{b*b/b*b}$ mice. However, these two observations might be reconcilable if $Ca_V2.2e[37a]$ channels localize preferentially at transmitter release sites in nerve terminals of nociceptors of wild-type mice and in their absence (*Cacna1b*$^{b*b/b*b}$), $Ca_V2.2e[37b]$ channels target to these presynaptic locations and support transmission of nociception with similar efficacy. There are no gross differences in anti-$Ca_V2.2$ signals in dorsal spinal horn among genotypes, but experiments designed to quantify the density of presynaptic N-type channels would be needed to test these and other possibilities.

Cacna1b$^{aa*/aa*}$ mice are physiologically compromised, but our behavioral analyses suggest that transmission of nociceptive signals and morphine's analgesic actions are very similar to those in wild-type mice. This might be unexpected, because N-type currents and $Ca_V2.2$ protein levels are reduced in DRG neurons, but the results are consistent with reports that withdrawal latencies to thermal stimuli are unchanged in *Cacna1b*$^{-/-}$null mice compared with wild-type mice (Shapiro and Hille, 1993; Luebke and Dunlap, 1994; Hille et al., 1995; Kammermeier et al., 2000; Saegusa et al., 2002; Elmslie, 2003; Altier and Zamponi, 2004; Tedford and Zamponi, 2006). As noted above, experiments are needed to measure the relative contribution of N-type currents to transmission in the dorsal spinal horn.

Voltage-independent inhibition and morphine analgesia

Voltage-independent inhibition of N-type calcium currents has been studied for more than a decade (Shapiro and Hille, 1993; Luebke and Dunlap, 1994; Hille et al., 1995; Kammermeier et al., 2000; Elmslie, 2003; Tedford and Zamponi, 2006). From these and other findings, a hypothesis has developed that voltage-independent inhibition of presynaptic N-type calcium channels via G protein–coupled receptors represents a mechanism for transmitter- and drug-mediated inhibition of synaptic transmission independent of neuronal activity (Luebke and Dunlap, 1994; Kammermeier et al., 2000; Elmslie, 2003; Altier and Zamponi, 2004; Ikeda and Dunlap, 2007). By contrast, a purely voltage-dependent mechanism would inhibit N-type channels and synaptic transmission most strongly during periods of low neuronal activity, but would become less effective as activity increased (Ikeda and Dunlap, 1999; Elmslie, 2003; Ikeda and Dunlap, 2007). Voltage-independent inhibition of N-type calcium channels through $G_{i/o}$ coupled

receptors and e37a might underlie some of the analgesic actions of morphine, particularly at higher doses. However, e37a may also influence other properties of N-type channels, including cellular distribution and, as we report here, N-type current densities. One or all of these could influence the spinal-level actions of morphine.

Although morphine is a highly effective analgesic in response to noxious thermal stimuli in naïve mice and humans, it is much less effective against the thermal hyperalgesia characteristic of neuropathic pain (Costigan et al., 2009). Expression levels of many genes are altered in the DRG of animals experiencing neuropathic pain. These changes have been implicated in the development and maintenance of chronic pain as well as in the loss of morphine efficacy (Costigan et al., 2009). $Ca_V2.2$ mRNA and protein levels are not thought to change in DRG after peripheral nerve injury, but as we have reported (Altier et al., 2007), $Ca_V2.2$e[37a] mRNAs are reduced. In light of the present study, it is possible that an injury-induced shift from e37a-containing to e37b-containing $Ca_V2.2$ channels in nociceptors, and therefore a concomitant change in inhibition of N-type calcium channels via μ-opioid receptors, might contribute to decreased spinal-level analgesia in response to morphine.

Cell-directed splicing of e37a

E37a is enriched in a subset of nociceptors in DRG (Bell et al., 2004). What are the factors that control exon selection—an important step in the pain pathway—in these cells? Genome-wide analyses show that several proteins are involved in driving neuronal-specific alternative splicing (Licatalosi et al., 2008; Zhang et al., 2008), but there are few examples of how these factors coordinate exon selection in specific gene

families within defined populations of neurons. Several neuronal splicing factors can function both as repressors and enhancers, depending on binding location with respect to the target exon, and exon selection probably depends on the relative contributions of several splicing factors working in concert (Boutz et al., 2007; Li et al., 2007; Licatalosi et al., 2008). The expression profile of e37a and the marked decrease in $Ca_V2.2$ protein levels in*Cacna1b*$^{aa*/aa*}$ mice suggest that most neurons may contain repressor activity that prevents e37a inclusion during splicing. However, our analysis of N-type current densities among several cell types of DRG from *Cacna1b*$^{aa*/aa*}$ mice suggest that e37a selection depends on additional factors with differential actions in these three classes of neuron. We studied *Cacna1b* gene sequences at and close to e37a and e37b splice junctions, but we have not identified the *cis* elements and *trans* factors that regulate alternative splicing at this site. We hope new data from genome-wide screens of splicing factor–RNA binding events will help define cell-specific mechanisms that orchestrate alternative splicing in Ca_V2 pre-mRNAs in specific neurons (Boutz et al., 2007; Licatalosi et al., 2008; Zhang et al., 2008).

The e37a/e37b splice site is conserved in all mammalian *Cacna1b* genes, so activity unique to e37a must provide some evolutionary advantage. Our data suggest that at higher doses, morphine engages e37a in spinal analgesia to thermal stimuli, but it is likely that endogenous transmitters use this inhibitory pathway to control nociception under certain conditions. Identifying cell-specific splicing factors that control alternative splicing of e37a could lead to new therapeutic approaches to increase the efficacy of drugs and neurotransmitters that work through G protein–coupled receptors to inhibit N-type calcium channels. Such studies could also provide insight into cell-specific,

coordinated alternative splicing of several pre-mRNAs that contribute to setting the efficacy of transmission in the pain pathway.

Methods

Construction of genomic clones for mouse exon substitution

To create *Cacna1b*$^{b*b/b*b}$ mice, we substituted e37a with e37b*; to create *Cacna1b*$^{aa*/aa}$ mice, we substituted e37b with e37a*. We derived mouse genomic DNA for all constructs from the MICER clone MHPN59f07 (Wellcome Trust Sanger Institute). Details of the cloning steps are given in "Supplementary - Construction of genomic clones for mouse exon substitution" (below). To facilitate detection of the specific exons spliced into the final mRNA products, we introduced silent mutations into restriction sites of the substituted exons; we mutated the BsrGI site in the mutant e37a to produce e37a* and mutated the XhoI site in e37b to produce e37b*.

We inserted a 2-kilobase (kb) *loxP-Neo*^{R}*-loxP* cassette into each targeting construct at the AfeI site located in the intron between the normal positions of e37a and e37b. We added flanking AfeI sites to the *loxP-Neo*^{R}*-loxP* cassette amplified from *PL452* by PCR with primers SD29for and SD31rev. Finally, we reintroduced the mutagenized DNA into BamHI-EagI sites to create the final ~12-kb targeting constructs in pBSSK+.

Supplementary - Construction of genomic clones for mouse exon substitution

We cloned the ~9.9 kb AscI fragment from MHPN59f07 spanning e36-e38 of *Cacna1b* into the BssHII site of *pBluescript II SK*+ (Stratagene). To facilitate mutagenesis, we subcloned the 2.8 kb BamHI-EagI fragment containing e37a and e37b into *pBluescript II*

SK+. After several rounds of mutagenesis (QuickChange II XL Site-Directed Mutagenesis Kit, Stratagene) and we reinserted the mutated fragments into the BamHI-EagI sites to recreate the ~12 kb AscI final constructs for gene targeting. To create the e37a-e37a* construct used to make the *Cacna1b*$^{aa*/aa}$ mice, we created an intermediate construct (e37a-Δe37b) with primers SD7for and SD8rev. We created another intermediate construct (*e37a*-e37b*) to delete the BsrGI site in e37a by introducing a silent single nucleotide mutation with primers SD19for and SD20rev. We PCR amplified a mutagenesis primer that contained e37a* flanked by the upstream and downstream intronic sequences of e37b from the *e37a*-e37b* construct with primers SD17for and SD18rev; we used the resulting primer to insert e37a* into the De37b position of the *e37a-De37b* construct, creating the *e37a-e37a** targeting construct. We used a similar strategy to create the *e37b*- e37b* construct used to make *Cacna1b*$^{b*b/b*b}$ mice. We created the *De37a-e37b* construct with primers SD5for and SD6rev and with primers SD21for and SD22rev, created the *e37a-e37b** intermediate construct to delete the XhoI site in e37b. We used the mutagenesis primer, amplified with primers SD15for and SD16rev, to insert e37b* into the De37a position of the *De37a-e37b* construct, creating the *e37b*-e37b* targeting construct.

Mouse embryonic stem cell gene targeting and mouse breeding

Animal housing and experimental procedures were in accordance with Brown institutional animal care and use committee guidelines. In brief, we used 129Ola embryonic stem cells derived from a male embryo, grown on mitotically inactive SNL76/7 feeder cells. We transformed 10^7 embryonic stem cells with 20 µg of a

construct linearized with PvuI and selected with G418 after 24 h. We selected 200 G418-resistant clones for further analysis. We used PCR to identify correctly targeted embryonic stem cell clones. We isolated E3.5 blastocysts from C57BL/6- *Tyr*$^{c\text{-}Brd}$ female mice and injected them with 12–20 embryonic stem cells harvested by trypsinization from 90%-confluence cultures. We then implanted injected blastocysts into day-2.5 pseudopregnant females to generate chimeras (eight to ten injected embryos per uterine horn). We mated male chimeras with C57BL/6-*Tyr*$^{c\text{-}Brd}$ females to obtain F1 progeny. We obtained germline transmission of the mutant alleles with several targeted cell lines for each construct.

Identification of correctly targeted embryonic stem cell clones

We confirmed homologous integration with two PCR reactions on genomic DNA from each embryonic stem cell clone. Integration from the long arm was confirmed by PCR amplification of a 7-kb product with Clontech′s Advantage 2 Polymerase Mix (35 cycles, 68 °C annealing, 8 min extension at 68 °C) with primers SD77for (anneals 5′ to e37a, outside of the targeting construct sequence) and SD64rev (anneals to the 5′ end of the *Neo*^{R} insert). Homologous integration from the short arm was confirmed by PCR amplification of a 3.5-kb product using Taq polymerase (35 cycles, 60 °C annealing, 4 min extension at 72 °C; New England Biolabs) and primers SD47for (anneals to the 3′ end of the *Neo*^{R} insert) and SD79rev (anneals 3′ to e37b, outside of the targeting construct sequence). We also confirmed correct targeting by sequencing through the substituted region of the *Cacna1b* gene of *Cacna1b*$^{aa*/aa}$ and *Cacna1b*$^{b*b/b*b}$ mice.

We used BsrGI to identify the exon present in the normal e37a position. In BsrGI digests of PCR products amplified using primers SD62 for (anneals upstream of the normal e37a position) and SD64rev (35 cycles, 60 °C annealing, 2 min extension at 72 °C with Taq polymerase), e37a was digested by BsrGI (617 and 1,156 bp), whereas e37b* was not (uncut, 1,773 bp). Similarly, we used XhoI to identify the exon present in the normal e37b position, digesting PCR products amplified using primers SD47for and SD48rev (anneals downstream of the normal e37b position). E37b has two XhoI sites (generating products of 144, 216 and 636 bp), and e37a* has one XhoI site (generating products of 144 and 852 bp).

Genomic DNA isolation

We incubated a 0.3-0.5 cm tail piece from 7-9 day old mouse overnight at 60°C with 300 ml lysis buffer (50 mM Tris-HCl pH7.5, 50 mM EDTA pH 8.0, 100 mM NaCl, 5 mM DTT, 0.5 mM spermidine, 1% SDS) and 20 ml 10 mg ml-1 fresh proteinase K, then extracted once with 300 ml phenol/choloform/isoamyl alcohol (25:24:1) by shaking vigorously for 30 sec. We separated phases by centrifugation for 15 min , 16k relative centrifugal force (r.c.f.), transferred the aqueous phase to a new tube and precipitate genomic DNA with 300 ml of isopropanol and centrifugation for 10 min (16k r.c.f.) at room temperature. After re-suspending in 200 ml TE (10 mM Tris-HCl pH 8.0, 1mM EDTA), DNA was precipitated by 20 ml of 3M sodium acetate pH5.2 and 500 ml ethanol and centrifugation (16k r.c.f.) for 10 min. We dissolved the DNA pellet in 300 ml 10mM Tris-HCl pH 8.0 and used 1 ml for genotyping PCR reaction.

RNA extraction and reverse transcription polymerase chain reaction (RT-PCR)

We extracted total DRG RNA from 10 P10 mice by homogenization with TriZol reagent (Invitrogen) following the manufacturer's recommendations. We reverse transcribed from 1 mg of total RNA using SuperScript First Strand system (Invitrogen) with oligo-(dT)12-18 priming. We PCR amplified a 430 bp fragment spanning e35 and e38 from 1 ml of the first-strand RT reaction using Taq Polymerase (New England Biolabs) [35 cycles, 60°C annealing, 1 min extension at 72°C] and primers SD151 for and SD153rev. We used BsrGI (which cuts e37a) and XhoI (which cuts e37b) to distinguish WT from mutant mRNAs.

PCR Primers:

SD5for 5'- CCTGTAACATTTCCTTTCCAGTGTTTGCAACTTCAGAGCCTCC

SD6rev 5'- GGAGGCTCTGAAGTTGCAAACACTGGAAAGGAAATGTTACAGG

SD7for 5'- CCTCTGGAACGGGTTTCCAGTGTAGACCTTGACCCTGCACTG

SD8rev 5'- CAGTGCAGGGTCAAGGTCTACACTGGAAACCCGTTCCAGAGG

SD15for 5'- CCTGTAACATTTCCTTTCCAGTGGGCGCATCAGTTACAATGAC

SD16rev 5'- GGAGGCTCTGAAGTTGCAAACCTTGTATGCAACTCGAGCCG

SD17for 5'- CCTCTGGAACGGGTTTCCAGTTGCCGGATTCATTATAAGGATATG

SD18rev 5'- CAGTGCAGGGTCAAGGTCTACCTTGTAGGCCAACCTACGAGG

SD19for 5'- GCCGGATTCATTATAAGGATATGTATAGTTTGTTGCGTTGTATTG

SD20rev 5'- CAATACAACGCAACAAACTATACATATCCTTATAATGAATCCGGC

SD21for 5'- GAAGAAATGCCCGGCACGAGTTGCATACAAGGTTTG

SD22rev 5'- CAAACCTTGTATGCAACTCGTGCCGGGCATTTCTTC

SD29for 5'- CATGAGCGCTGAATTCCTGCAGCCCAATTCC

SD31rev 5'- CTAGAGCGCTCCCTCGAGGGACCTAATAACTTCG

SD47for 5'- GGGAAGACAATAGCAGGCATGC

SD48rev 5'- CTGGGATGAGAGCAAAGGGT

SD62for 5'- ATGGACGGGGTGCAACATGG

SD64rev 5'- CTACCCGGTAGAATTTCGACG

SD77for 5'- CCGTGGTGGCATTTGAGGC

SD79rev 5'- CCAAGGCTATGTGACTCACC

SD151for 5'- AGGCCTGGCATGAGATCATGC

SD153rev 5'- TGAGGGCCATCAGTGTGGACG

Neo^{R} cassette deletion

We genotyped F1 animals with genomic DNA from tails, using the four primer sets described above. We crossed more than eight positive animals identified for each of the two mutations with a *Cre* deletor strain (B6.FVB-Tg(EIIa-cre)C5379Lmgd/J; Jackson Laboratory stock no. 003724) to delete the *Neo*^{R} gene. We genotyped *ΔNeo*^{R} mice for appropriate e37 mutations (see genotyping below). We crossed *ΔNeo*^{R} siblings carrying appropriate mutations to produce homozygotes that were maintained by crossing of sibling homozygotes. We maintained at least two separate homozygous lines for each mutation.

Genotyping

We used primers SD62for and SD64rev to genotype for *ΔNeo*^{R} by genomic PCR. We performed this genotyping for at least two generations. Refer to Figure 3.2 for complete genotyping of *Cacna1b*^{ab}, aa* and b*b heterozygotes and homozygotes.

Western blot analysis

We pooled DRG from five mice but carried out three separate experiments on brains from three mice (2–8 months). Details of protein isolation and antibody staining are given in "**Supplementary western blot methods"** below. We developed all membranes with ECL reagent (Amersham Biosciences) and used time-series exposures to ensure the signal was in the linear range. We measured signal densities (ImageQuantTM software, Amersham) from TIFF images generated from nonsaturated films. After background correction, we quantified $Ca_V2.1$- or $Ca_V2.2$-derived signals as a fraction of the average GAPDH signal. Complete uncropped blots are shown in Figure 3.9.

Supplementary western blot methods

We homogenized tissue on ice in RIPA buffer (50 mM Tris-HCl pH 7.5, 150mM NaCl, 1% Igepal, 0.5% sodium deoxycholate, 0.1% SDS) containing protease inhibitor (Complete, mini; Roche Diagnostics), followed by 2-3 hr incubation on ice and centrifugation at 14.9k r.c.f. for 20 min at $4^{O}C$ to remove debris. We diluted a volume of supernatant equivalent to 20 µg of protein (determined by BCA Protein Assay) for each sample in 2X reducing buffer (100mM Tris-HCl pH 6.8, 4% SDS, 0.2% bromophenol blue, 20% glycerol, 200 mM dithiothreitol). We incubated samples at room temperature for 15 min before resolving on 6% ($Ca_V2.2$) or 15% (GAPDH) SDS-polyacrylamide gels (4% stacking gels were used in both cases). We discovered that boiling samples at this stage caused $Ca_V2.2$ protein to aggregate, impeding protein movement through the gel. Proteins were transferred using electrophoresis to 0.45 mm nitrocellulose membranes (Whatman) for 1hr on ice. After blocking with 5% non-fat dry milk, 0.1% Tween-20, PBS

for 1 hr, membranes were probed with antibodies against $Ca_V2.2$ (Alomone) and $Ca_V2.1$ diluted 1:200 (Alomone) and Glyceraldehyde 3-Phosphate Dehydrogenase (GAPDH) diluted 1:1,000 (Cell Signaling, clone 14C10) for one hour at room temperature. We then washed membranes (3X; 0.1% Tween-20, PBS) and incubated with horseradish peroxidase labeled donkey anti-rabbit IgG secondary antibodies diluted 1:15,000 (Jackson) for 1 hr at room temp. All antibodies were diluted in 1% BSA, 0.1% Tween-20, 1X PBS unless otherwise recommended by vendor. Membrane stripping (before re-probing) was performed with stripping buffer: (2%SDS, 62.5 mM Tris-HCL pH 6.8, 100 mM 2-mecaptoethanol) and incubation for 30 minutes at 50 ^{O}C (with rocking), followed by two washing steps with excess PBS-T, and blocking as usual.

Cell isolation and electrophysiology

We harvested DRG from P7–P9 mice of all three genotypes. We obtained a higher yield of neurons from DRG of these young animals. However, we also recorded N-type currents from mice of the same age as those used for behavior studies (>2 months). Although the yield of neurons was lower from the older mice, we confirmed that results from N-type currents recorded from their nociceptors, for all three genotypes, were not different from those of P7–P9 animals. Single neurons were dissociated from ganglia in Hank's Balanced Salt Solution (HBSS, GIBCO) medium containing 1.5 mg ml^{-1} collagenase (Sigma) and 2 mg ml^{-1} trypsin (Sigma) at 37 °C for ~30 min, then triturated with a fire-polished pipette. We quenched protease activity with Dulbecco's Modified Eagle Medium (DMEM, GIBCO) with 10% fetal bovine serum (vol/vol, FBS, GIBCO). After two washes, we plated neurons on coverslips coated with poly-D-lysine

(Sigma) in 10% FBS-DMEM supplemented with 1 ng ml^{-1} nerve growth factor (Sigma) and incubated them at 37 °C with 5% CO_2. We sylgard-coated and fire-polished electrodes to a resistance of 3-6 MΩ. Our external solution contained 135 mM TEA-Cl, 1 mM $CaCl_2$, 10 mM HEPES, 4 mM $MgCl_2$ and 0.1 μM TTX, adjusted to a pH of 7.2 with TEA-OH. Our pipette solution contained 126 mM CsCl, 4 mM Mg-ATP, 1 mM EDTA, 10 mM EGTA and 10 mM HEPES, adjusted to a pH of 7.2 with CsOH. We did not include GTP in the patch pipette because we had evidence from studies of expressed channels (Raingo et al., 2007) that low levels of GTP (0.2–0.3 mM) can lead to tonic inhibition of N-type currents in a voltage-independent manner in the absence of agonist. However, we obtained highly reproducible inhibition of N-type currents by brief repeat applications of DAMGO (Sigma), suggesting that the components necessary for mediating inhibition do not wash out under the conditions of our experiments. We limited the cell's exposure to DAMGO to 1 min. This also avoided μ-opioid receptor desensitization. We evoked whole-cell calcium currents by 10-ms test pulses from a holding potential of −80 mV and monitored tail currents with a 5-ms repolarizing pulse to −60 mV. We applied 2 μM ω-conotoxin GVIA (Alomone) via a pipette to inhibit the N-type current and reapplied voltage steps. We removed ω-conotoxin GVIA from the recording chamber between recordings by washing with 2% SDS (wt/vol) and 10 mM DTT for 20 min. We used pClamp version 8.1 software and the Axopatch 200A (Axon Instruments) for data acquisition; data were filtered at 2 kHz (–3 dB) and sampled at 20 kHz. We compensated series resistance by 70–90% with a 7-μs lag and performed online leak correction with a P/–4 protocol. All recordings were obtained at room temperatures.

Behavioral analyses

We tested paw-withdrawal thresholds with Plantar Testing Instruments (IITC) (Hargreaves et al., 1988) on 8- to 16-week-old male mice. We applied a high-intensity beam (set at 20%, ~45 W) to the middle of the plantar surface of a resting mouse. Paw-withdrawal latency was measured to the nearest 0.1 s, with a cutoff value of 20 s. We injected 3 μg morphine sulfate in a volume of 5 μl intrathecally under anesthesia (2% isoflurane, vol/vol) with a 28-gauge needle connected to a microsyringe through a PE 50 polyester catheter (15 cm) (Hylden and Wilcox, 1980). We tested paw-withdrawal thresholds before and 10, 20, 30, 40, 50 and 60 min after morphine injection. We calculated the percentage of maximum possible effect of morphine (%MPE) using the following formula: $\%MPE = (PWL_{morphine} - PWL_{baseline})100/(20 - PWL_{baseline})$, where PWL is paw-withdrawal latency. We used the area under the curve of %MPE to compare the overall effect of intrathecal morphine among the three genotypes. Data shown in figures are means ± s.e.m. of measurements from at least ten animals for each genotype.

Statistical analysis

Data are presented as means ± s.e.m. Comparisons of mean differences between groups were made by unpaired two-tailed Student's *t*-test unless otherwise stated. $P < 0.05$ was considered to be statistically significant. We used the software Origin 6.1.

Figure 3.1

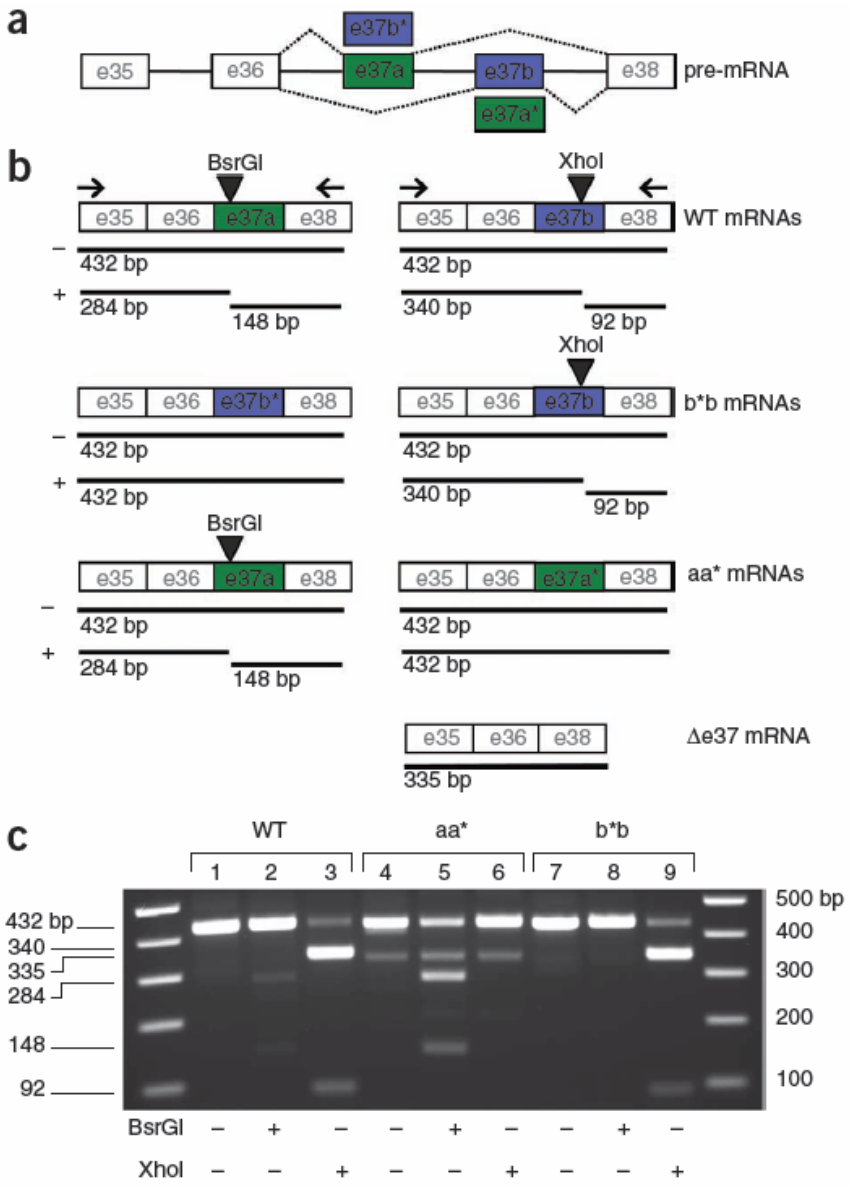
a
e35
e36
e37b'
e37a
e37b
e37a'
e38
pre-mRNA
b
BsrGI
XhoI
WT mRNAs
432 bp
284 bp
148 bp
340 bp
92 bp
b*b mRNAs
aa* mRNAs
Δe37 mRNA
335 bp
c
WT
aa*
b*b
1 2 3 4 5 6 7 8 9
432 bp
340
335
284
148
92
500 bp
400
300
200
100
BsrGI
XhoI

Figure 3.1

Exon 37 substitution in *Cacna1b* and resultant mRNAs in wild-type and mutant DRG. **(a)** Schematic of *Cacna1b* gene showing mutually exclusive exons e37a (green) and e37b (blue) with constitutively expressed exons (e35, e36 and e38). **(b)** Exon-replacement strategy and predicted mRNAs. E37b* replaces e37a, and e37a* replaces e37b to generate *Cacna1b*$^{b*b/b*b}$ (b*b) and *Cacna1b*$^{aa*/aa*}$ (aa*) mice, respectively. Shown under exon diagrams are predicted products when $Ca_V2.2$ mRNAs derived from DRG of wild-type, b*b and aa* mice are subjected to RT-PCR with primers located in exons 35 and 38. Sizes of PCR products undigested (−) and digested with BsrGI or XhoI (+) are indicated. Uncut cDNAs containing either e37a or e37b are 432 bp, and cDNAs lacking either e37a or e37b (Δ37) are 335 bp. BsrGI cuts wild-type e37a into 284-bp and 148-bp products, and XhoI cuts wild-type e37b into 340-bp and 92-bp products. Mutant e37a*– and mutant e37b*–containing sequences lack BsrGI and XhoI sites, respectively. **(c)** Results of RT-PCR from 1 μg of total RNA isolated from mouse DRG of wild-type (lanes 1–3), aa* (lanes 4–6) and b*b (lanes 7–9) mice. PCR products untreated (lanes 1, 4 and 7) and treated with BsrGI (lanes 2, 5 and 8) or XhoI (lanes 3, 6 and 9) were separated on a 2% TAE agarose gel. Lanes 1–9 are flanked by 1 kb Plus DNA ladders. A 335-bp product was amplified from DRG of aa* mice and was resistant to BsrGI and XhoI. Sequencing showed that it corresponds to mRNA lacking e37 (Δ37).

Figure 3.2

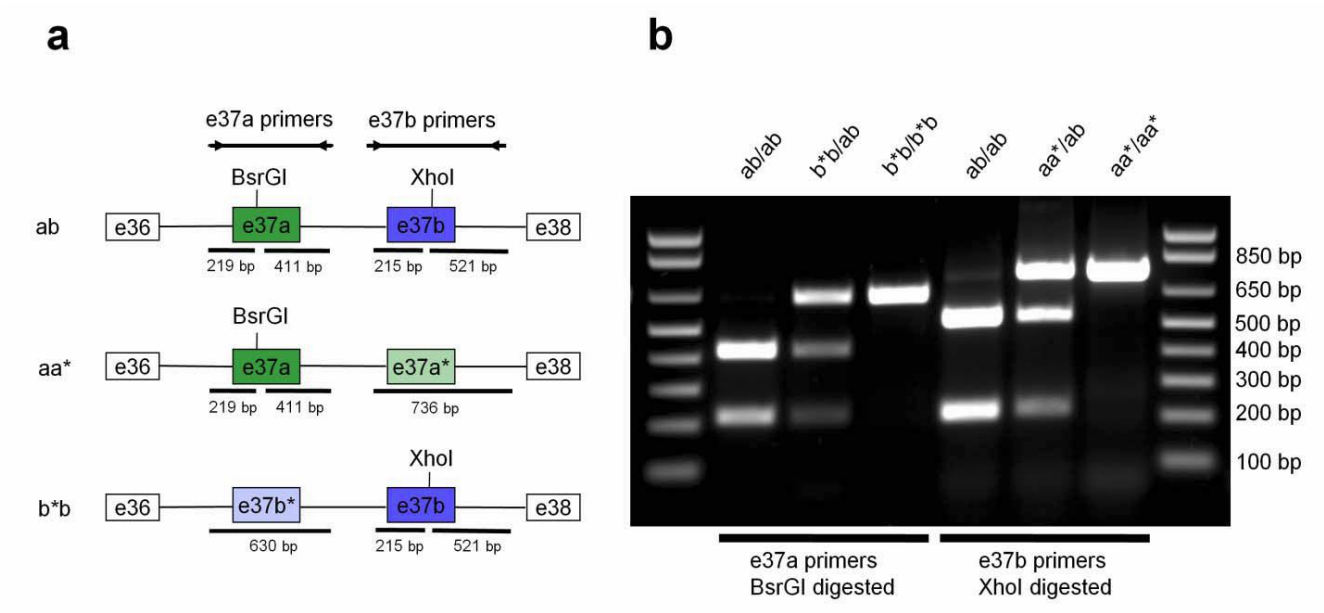
a
e37a primers
e37b primers
BsrGI
XhoI
ab
e36
e37a
e37b
e38
219 bp
411 bp
215 bp
521 bp
BsrGI
aa*
e36
e37a
e37a*
e38
219 bp
411 bp
736 bp
XhoI
b*b
e36
e37b*
e37b
e38
630 bp
215 bp
521 bp
b
ab/ab
b*b/ab
b*b/b*b
ab/ab
aa*/ab
aa*/aa*
850 bp
650 bp
500 bp
400 bp
300 bp
200 bp
100 bp
e37a primers
BsrGI digested
e37b primers
XhoI digested

Figure 3.2

Genotyping mouse strains. **(a)** Schematic representation of genotyping data obtained from genomic DNA of *Cacna1b* WT, aa* and b*b heterozygous and homozygous mice. To identify which exon (e37a or e37b*) was present in the position normally occupied by e37a, a 630 bp product was PCR amplified with e37a intronic primers that anneal upstream and downstream of the normal e37a position. Digestion of the product with BsrGI identified the exon present in the "a" position: e37a digests into two bands (219 and 411 bp), and e37b* does not digest (630 bp). Possible genotyping results for the "a" region (BsrGI digested) are: WT (ab/ab) = 219, 411 bp; heterozygous (b*b/ab) = 219, 411, 630 bp; homozygous (b*b/b*b) = 630 bp. To identify the exon (e37b or e37a*) present in the position normally occupied by e37b, a 736 bp product was PCR amplified with e37b intronic primers that anneal upstream and downstream of the normal e37b position, resulting in a 736 bp product. Digestion with XhoI identified the exon present in the "b" position: e37b digests into two bands (215 and 521 bp) and e37a* does not digest (736 bp). Possible genotyping results for the "b" region (XhoI digested) are: WT (ab/ab) = 215, 521 bp; heterozygous (aa*/ab) = 215, 521, 736 bp; homozygous (aa*/aa*) = 736 bp. **(b)** Representative genotyping of *Cacna1b* WT, aa* and b*b heterozygous and homozygous mice. To genotype the e37a region, mouse genomic DNA was PCR amplified using Taq Polymerase (New England Biolabs), 35 cycles, 60°C annealing, 1 min extension at 72°C with primers SD62for 5'-ATGGACGGGGTGCAACATGG (anneals to the intron upstream of the normal e37a position) and SD130rev 5'- CATCCAGGATGCTGGAACG

(anneals to the intron downstream of the normal e37a position). The resulting 630 bp product was digested with BsrGI, which only cuts e37a (219 and 411 bp). To genotype the e37b region, DNA was PCR amplified (as above) with primers SD132for 5'- CTGCTGCTGTGGTTCTCAGC (anneals to the intron upstream of the normal e37b position) and SD48rev 5'- CTGGGATGAGAGCAAAGGGT (anneals to the intron downstream of the normal e37b position). The resulting 736 bp product was digested with XhoI, which only cuts e37b (215 and 521 bp). Mouse genotypes are shown above the lanes. PCR primers and diagnostic restriction enzyme digestion shown below the lanes. Flanking lanes, 1 Kb Plus DNA ladder (Invitrogen).

Figure 3.3

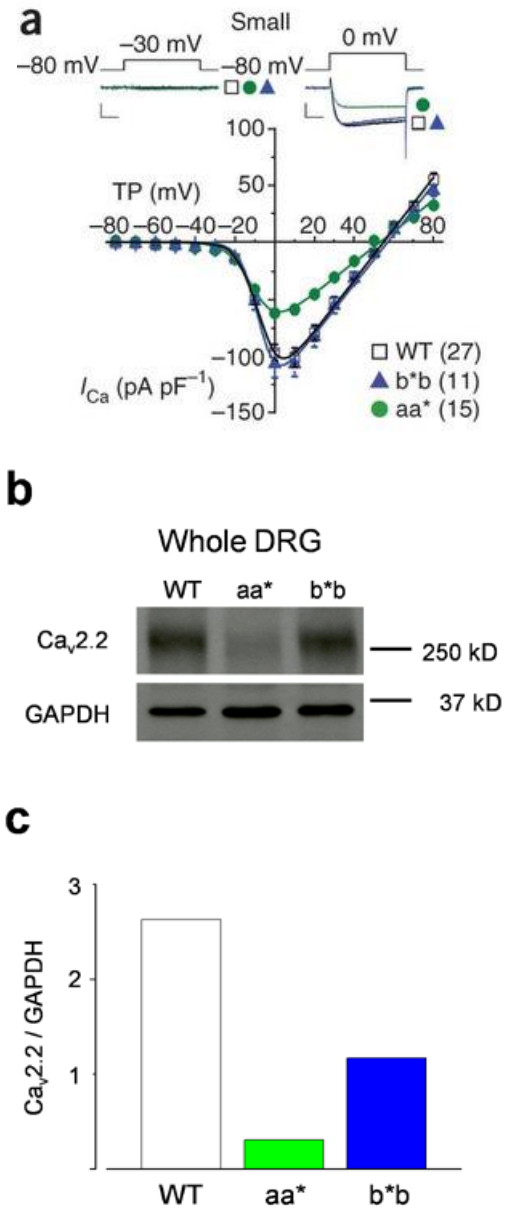
a
Small
−30 mV
0 mV
−80 mV
−80 mV
100
50
TP (mV)
−80 −60 −40 −20
20 40
80
−100
−150
I_{Ca} (pA pF^{-1})
WT (27)
b*b (11)
aa* (15)
b
Whole DRG
WT
aa*
b*b
$Ca_v2.2$
250 kD
GAPDH
37 kD
c
$Ca_v2.2$ / GAPDH
3
2
1
WT
aa*
b*b

Figure 3.3

Whole-cell calcium current densities in DRG neurons of *Cacna1b*$^{b*b/b*b}$ mice are indistinguishable from wild-type DRG neurons. **(a)** Average current-voltage relationships in small DRG neurons from wild-type, *Cacna1b*$^{b*b/b*b}$ (b*b) and *Cacna1b*$^{aa*/aa*}$ (aa*) mice. Currents were evoked by test pulses to −30 mV (left) and 0 mV (right) from a holding potential of −80 mV. A series of currents were elicited by depolarizations applied every 10 s to test potentials between −70 mV and +80 mV from a holding potential of −80 mV. Current densities are plotted (pA/pF) for small cells (13pF). Calcium current densities from *Cacna1b*$^{aa*/aa*}$ mice were significantly smaller than those from wild-type mice (P = 0.0004). Individual current voltage plots were fit with one Boltzmann function using average parameters. Scale bars, 500 pA and 5 ms. Data are means ± s.e.m. n values shown in parentheses are number of cells; all data sets contain recordings from at least nine mice. **(b)** Western blot of DRG lysates derived from wild-type, aa* and b*b mice using a polyclonal antibody directed to $Ca_V2.2$ and a monoclonal antibody directed to glyceraldehyde 3-phosphate dehydrogenase (GAPDH). $Ca_V2.2$ protein levels in DRG of aa* mice were lower than in wild-type mice. $Ca_V2.2$ protein runs at 260 kDa; location of a 250-kDa size marker is indicated. Complete, uncropped blots are shown in Figure 3.9. **(c)** Channel levels were determined for each transgenic mouse line using. The results are expressed as $Ca_V2.2$ over GAPDH, to control for loading ($Ca_V2.2$/GAPDH): 2.63, 0.31, and 1.17 for Cacna1b $^{wt/wt}$, Cacna1b$^{aa*/aa*}$ and Cacna1b$^{b*b/b*b}$, respectively. P values were 0.0005 for CACNA1B$^{aa*/aa*}$ and 0.004 for CACNA1B$^{b*b/b*b}$**.**

Figure 3.4

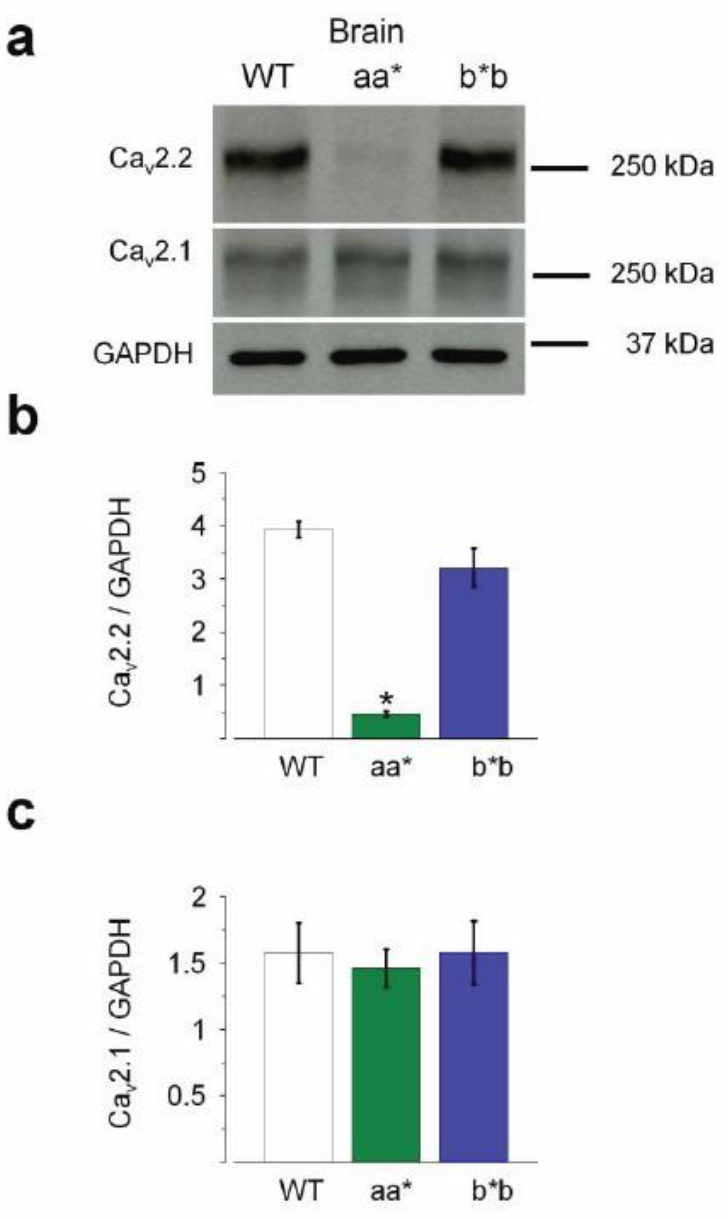
a
Brain
WT
aa*
b*b
$Ca_v2.2$
250 kDa
$Ca_v2.1$
250 kDa
GAPDH
37 kDa
b
$Ca_v2.2$ / GAPDH
5
4
3
2
1
*
WT
aa*
b*b
c
$Ca_v2.1$ / GAPDH
2
1.5
1
0.5
WT
aa*
b*b

Figure 3.4

Western blot analysis of brain $Ca_V2.2$ and $Ca_V2.1$ channel levels in Cacna1b $^{wt/wt}$, Cacna1b $^{aa*/aa*}$, and Cacna1b$^{b*b/b*b}$ mice. Three 9-10 week mouse brains of each genotype were homogenized and tested for levels of $Ca_V2.2$, $Ca_V2.1$ and GAPDH (as a control). **(a)** One representative set of western blot results (of three) is shown. The un-cropped Western blot is shown in Figure 3.9 below. **(b)** Protein levels were quantified, and results are shown as an average of the three $Ca_V2.2$ bands for each genotype after normalization to the average of three GAPDH bands for each genotype. We found that Cacna1b$^{aa*/aa*}$ and Cacna1b$^{b*b/b*b}$ mice express $Ca_V2.2$ protein at roughly 12% and 82% that of Cacna1b$^{wt/wt}$ mice respectively. The results (in arbitrary units) are as follows: 3.9 ± 0.15, 0.47 ± 0.048, and 3.21 ± 0.37 for Cacna1b$^{wt/wt}$, Cacna1b$^{aa*/aa*}$ and Cacna1b$^{b*b/b*b}$ respectively. The errors were calculated as standard errors. The P values are 0.000014 for CACNA1B $^{aa*/aa*}$ and 0.07 for CACNA1B$^{b*b/b*b}$, using a one-tailed, unpaired t test. **(c)** The $Ca_V2.2$ blots described above were stripped and re-probed for $Ca_V2.1$. Channel levels were determined for each transgenic mouse line using the same methods as for $Ca_V2.2$. We found that all lines express $Ca_V2.1$ channel at similar levels, indicating lack of compensation of $Ca_V2.2$. The results are: 1.58 ± 0.23, 1.46 ± 0.14, and 1.58 ± 0.24 for Cacna1b $^{wt/wt}$, Cacna1b$^{aa*/aa*}$ and Cacna1b$^{b*b/b*b}$, respectively. P values were 0.34 for CACNA1B$^{aa*/aa*}$ and 0.50 for CACNA1B$^{b*b/b*b}$**.**

Figure 3.5

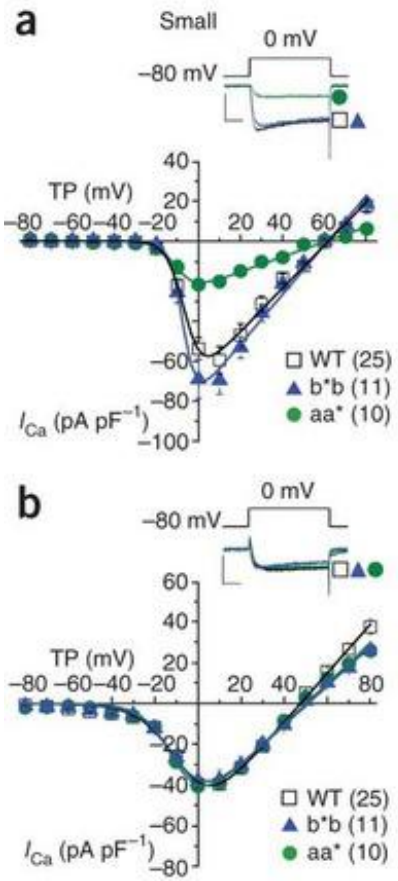
a
Small
0 mV
−80 mV
TP (mV)
−80 −60 −40 −20 20 40 60
40
20
−60
−80
−100
I_{Ca} (pA pF^{-1})
WT (25)
b*b (11)
aa* (10)
b
0 mV
−80 mV
60
40
20
TP (mV)
−80 −60 −40 −20 20 40 80
−20
−40
−60
−80
I_{Ca} (pA pF^{-1})
WT (25)
b*b (11)
aa* (10)

Figure 3.5

N-type and non–N-type current densities in sensory neurons of *Cacna1b*$^{b*b/b*b}$ mice are indistinguishable from those in wild-type mice. Average N-type **(a)** and non–N-type **(b)** calcium current–voltage relationships in small acutely dissociated DRG neurons from wild-type, *Cacna1b*$^{b*b/b*b}$ (b*b) and *Cacna1b*$^{aa*/aa*}$(aa*) mice. Representative currents shown above current voltage plots were evoked by test pulses to 0 mV from a holding potential of −80 mV and were recorded from each mouse line. Currents were elicited as described in Figure 3.3 and plotted as pA/pF to normalize for cell size. N-type currents and non–N-type currents correspond to ω-conotoxin GVIA–sensitive and ω-conotoxin GVIA–insensitive components of the whole-cell current, respectively. We isolated N-type currents in each cell by subtracting non–N-type currents (insensitive to 2 μM ω-conotoxin GVIA) from whole-cell currents. N-type current densities were significantly smaller in *Cacna1b*$^{aa*/aa*}$ mice than in wild-type mice (P = 0.0003). Individual current voltage plots were fit with one Boltzmann function using average parameters calculated from fitting individual curves. Scale bars, 500 pA and 5 ms. Data are means ± s.e.m. n values in parentheses are number of cells; data sets contain recordings from at least nine mice.

Figure 3.6

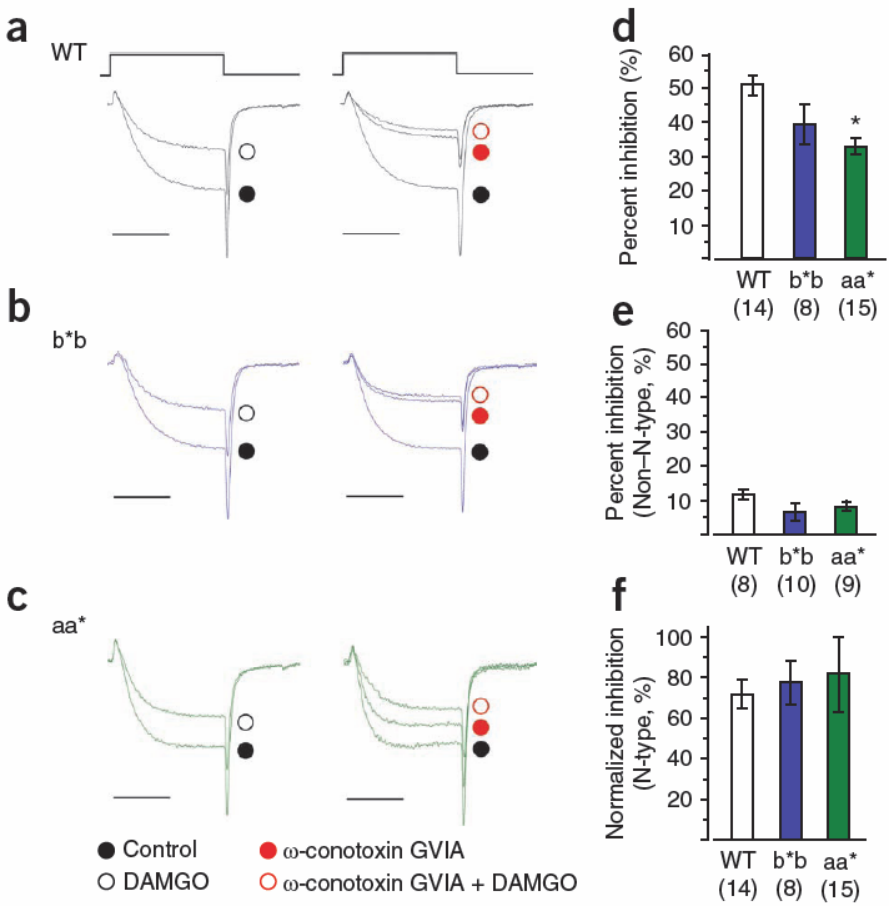
a
WT
b
b*b
c
aa*
Control
DAMGO
ω-conotoxin GVIA
ω-conotoxin GVIA + DAMGO
d
Percent inhibition (%)
60
50
40
30
20
10
*
WT (14)
b*b (8)
aa* (15)
e
Percent inhibition (Non–N-type, %)
60
50
40
30
20
10
WT (8)
b*b (10)
aa* (9)
f
Normalized inhibition (N-type, %)
100
80
60
40
20
WT (14)
b*b (8)
aa* (15)

Figure 3.6

DAMGO inhibits N-type currents similarly in nociceptors from all three genotypes.

(a–c) Representative currents from nociceptors isolated from wild-type **(a)**, *Cacna1b*$^{b*b/b*b}$ (b*b; **b**) and *Cacna1b*$^{aa*/aa*}$ (aa*; **c**) mice show the inhibitory actions of a saturating concentration of 10 μM DAMGO on calcium currents in the absence (left; whole-cell currents) or presence (right; non–N-type currents) of ω-conotoxin GVIA (2 μM). For comparison, current amplitudes are scaled relative to their respective controls. Currents were elicited by test pulses to 0 mV from a holding potential of −80 mV. Scale bar, 5 ms. (**d**,**e**) Average percent inhibition by DAMGO in nociceptors of wild-type, b*b, and aa* mice in the absence (**d**; whole-cell current) or presence (**e**; non–N-type current) of 2 μM ω-conotoxin GVIA. Values shown are means ± s.e.m. *n* values in parentheses are number of cells; all data sets contain recordings from at least nine mice. DAMGO was significantly less effective at inhibiting whole-cell currents in aa* mice than in wild-type mice (**d**; $P = 0.0432$). (**f**) DAMGO's inhibition of N-type currents in nociceptors, compared among the three genotypes. For comparison, because N-type current density was substantially smaller in nociceptors of aa* mice, percent inhibition by DAMGO was normalized to N-type current density with the following formula: $100\% \times ((I_{control} - I_{DAMGO}) - (I_{\omega\text{-conotoxin}} - I_{DAMGO}))/I_{N\text{-type}}$. $I_{control} - I_{DAMGO}$ represents whole-cell current; $I_{\omega\text{-conotoxin}} - I_{DAMGO}$ represents non–N-type current. Average values of $I_{\omega\text{-conotoxin}}$, I_{DAMGO} and $I_{N\text{-type}}$ were obtained from nociceptors of wild-type ($n = 8$), b*b ($n = 10$) and aa* ($n = 9$) mice for these calculations.

Figure 3.7

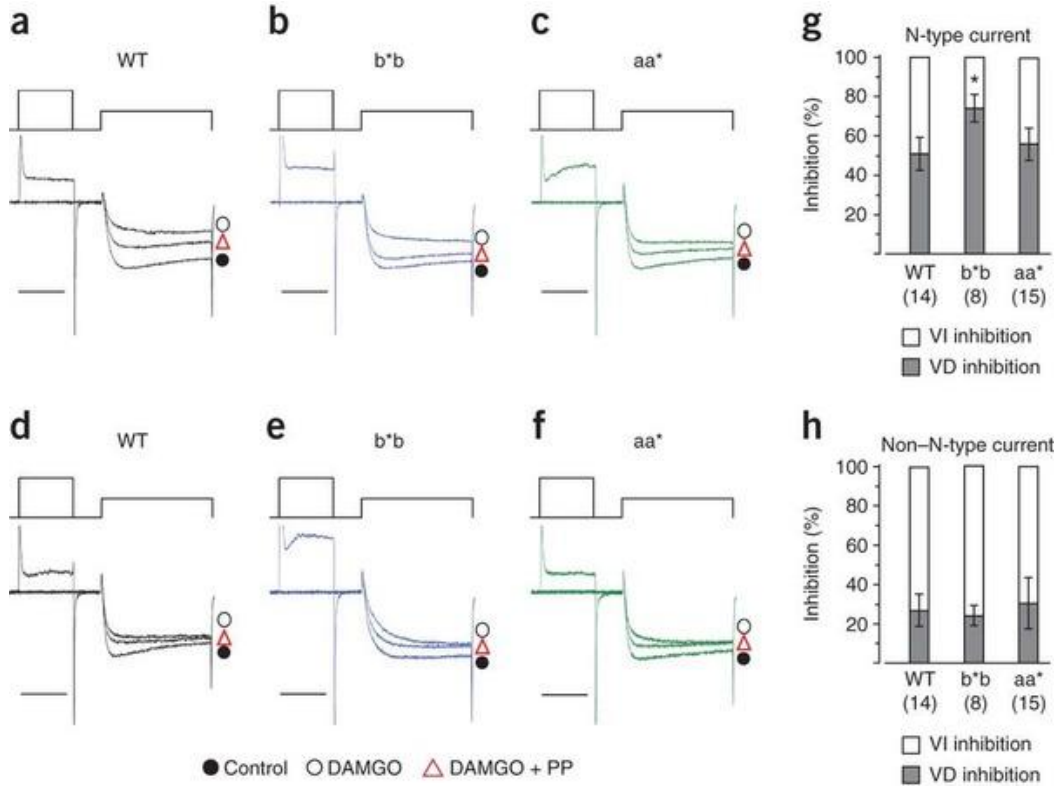
a
WT
b
b*b
c
aa*
g
N-type current
Inhibition (%)
100
80
60
40
20
*
WT (14)
b*b (8)
aa* (15)
VI inhibition
VD inhibition
d
WT
e
b*b
f
aa*
h
Non–N-type current
Inhibition (%)
100
80
60
40
20
WT (14)
b*b (8)
aa* (15)
VI inhibition
VD inhibition
Control
DAMGO
DAMGO + PP

Figure 3.7

Voltage-independent inhibition by DAMGO is reduced in nociceptors that only express e37b and not e37a**.** (**a**–**f**) Representative currents from small neurons isolated from wild-type (**a**,**d**), *Cacna1b*$^{b*b/b*b}$ (b*b; **b**,**e**) and aa* (**c**,**f**) mice show the inhibitory actions of 10 μM DAMGO on whole-cell currents in the absence (**a**–**c**; whole-cell currents) or presence (**d–f**) of ω-conotoxin GVIA (2 μM). Currents were elicited by test pulses to 0 mV from a holding potential of −80 mV without or with a strong prepulse (+ PP) to +80 mV to remove voltage-dependent inhibition. For comparison, current amplitudes are scaled relative to their respective controls. Scale bar, 5 ms. (**g**,**h**) Relative amount of voltage-dependent and voltage-independent inhibition of N-type (**g**; $P = 0.0321$) and non–N-type (**h**) currents mediated by 10 μM DAMGO in recordings from nociceptors of wild-type, b*b and aa*mice. VI, voltage-independent component of inhibition; VD, voltage-dependent component. Values shown are means ± s.e.m. *n* values shown are number of cells; all data sets contain recordings from at least nine mouse lines. Percent voltage-independent inhibition of N-type current was estimated as follows: 100% × ($VI_{whole\text{-}cell} - VI_{non–N\text{-}type}$)/total N-type inhibition.

Figure 3.8

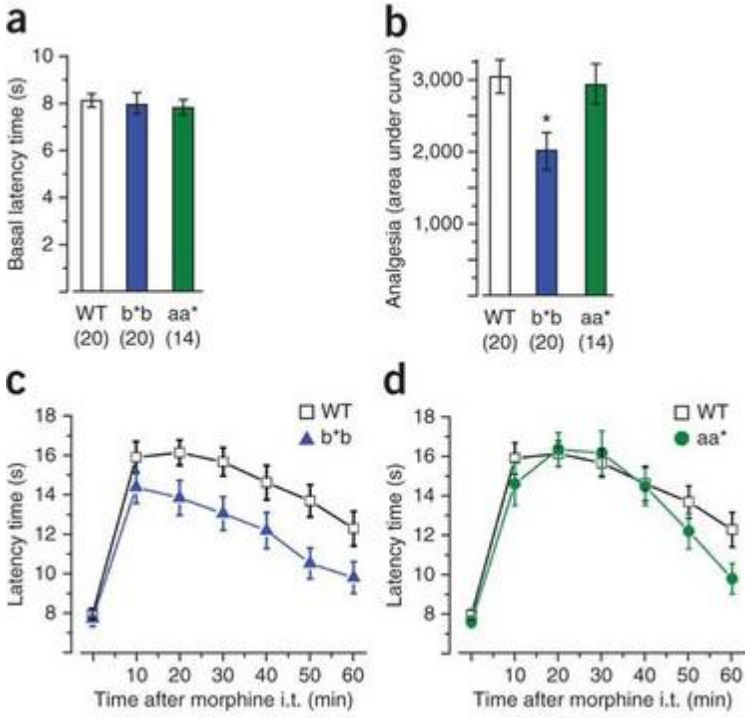
a
Basal latency time (s)
10
8
6
4
2
WT (20)
b*b (20)
aa* (14)
b
Analgesia (area under curve)
3,000
2,000
1,000
*
WT (20)
b*b (20)
aa* (14)
c
Latency time (s)
18
16
14
12
10
8
WT
b*b
10 20 30 40 50 60
Time after morphine i.t. (min)
d
Latency time (s)
18
16
14
12
10
8
WT
aa*
10 20 30 40 50 60
Time after morphine i.t. (min)

Figure 3.8

Morphine's spinal-level analgesia is reduced in mice that lack e37a. (**a**,**b**) Comparison of thermal pain thresholds in wild-type *(n* = 20), *Cacna1b*$^{b*b/b*b}$ (b*b; *n* = 20) and *Cacna1b*$^{aa*/aa*}$ (aa*; *n* = 14) mice before (**a**) and after (**b**) intrathecal morphine. Average basal paw-withdrawal latencies (PWLs; Hargreaves's test) in response to noxious thermal stimuli were not significantly different in wild-type, b*b and aa* mice (**a**; Student's *t*-test, *P* > 0.5). In **b**, to normalize for differences in baseline responsiveness among mice, intrathecal morphine analgesia was expressed as the integral (area under the curve) of the percentage of maximum possible effect (%MPE) for each group, where %MPE = $(PWL_{morphine} – PWL_{baseline})100/(20 – PWL_{baseline})$. Morphine was significantly less effective against thermal stimuli in b*b mice than in wild-type mice (Student's *t*-test, *P* = 0.004) but had similar efficacy in aa* and wild-type mice (Student's *t*-test, *P* = 0.77). (**c**,**d**) Time course of morphine analgesia after intrathecal (i.t.) injection (3 μg) at time 0 in wild-type and b*b mice (**c**) and in wild-type and aa* mice (**d**). The efficacy of morphine is reduced in b*b mice relative to wild-type mice. *P* values at 0, 10, 20, 30, 40, 50 and 60 min were 0.613, 0.190, 0.043, 0.023, 0.061, 0.008 and 0.044, respectively, comparing average responses in b*b and wild-type mice (Student's two-tailed *t*-test; **c**). Values shown are means ± s.e.m.

Figure 3.9

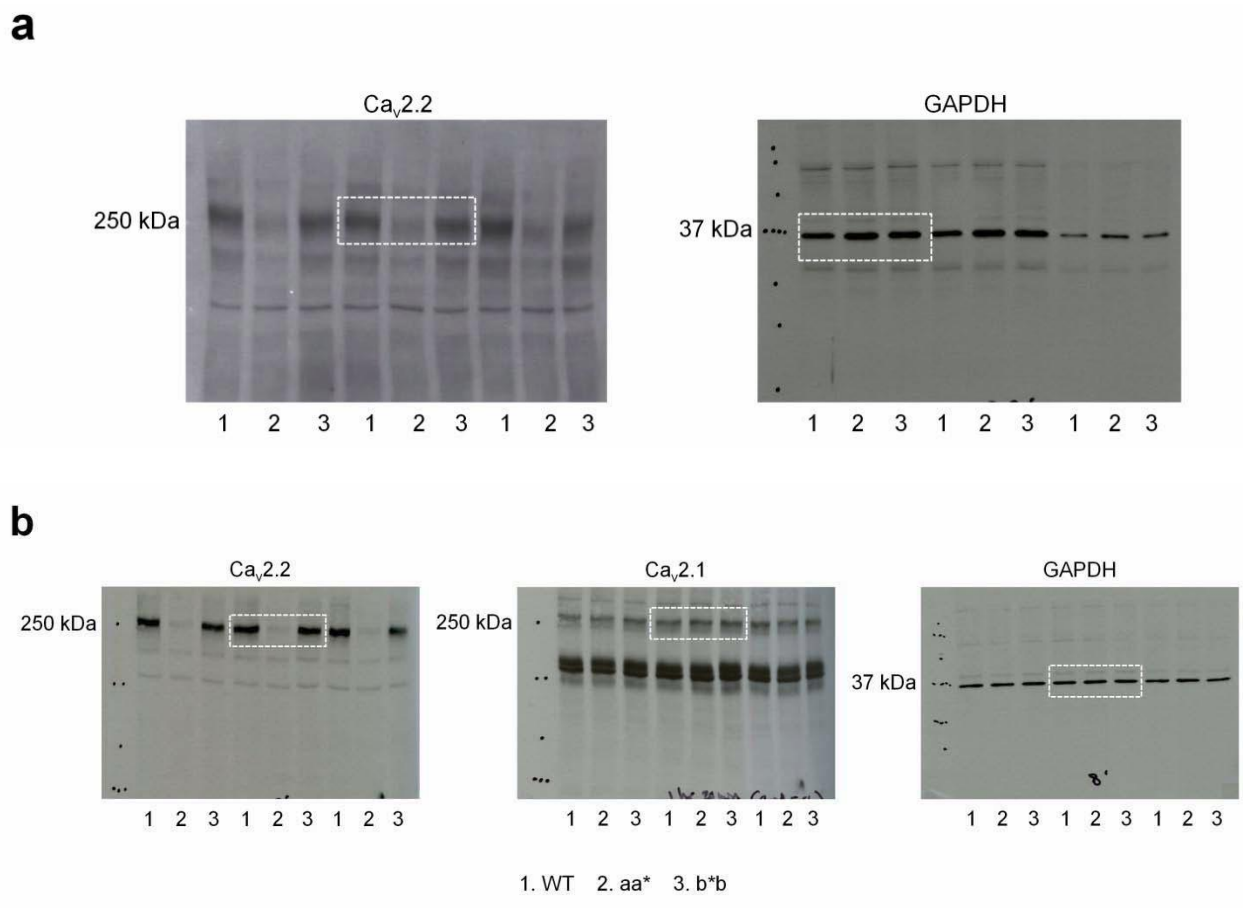
a
$Ca_v2.2$
250 kDa
1 2 3 1 2 3 1 2 3
GAPDH
37 kDa
1 2 3 1 2 3 1 2 3
b
$Ca_v2.2$
250 kDa
1 2 3 1 2 3 1 2 3
$Ca_v2.1$
250 kDa
1 2 3 1 2 3 1 2 3
GAPDH
37 kDa
1 2 3 1 2 3 1 2 3
1. WT 2. aa* 3. b*b

Figure 3.9

Complete blots for Westerns shown in Figure 3.3 and Figure 3.4.

(a) Full-length blots for $Ca_V2.2$ and GAPDH on samples derived from DRG of five different mice of the three genotypes indicated by the numbers at the bottom of blots: 1: WT, 2: aa* and 3: b*b. The last three lanes of the GAPDH blot are a 1:2 dilution of the samples used in lanes 1-6. Cropped versions of these blots appear in Figure 3.3. (**b**) Images of full-length blots for $Ca_V2.2$, $Ca_V2.1$ and GAPDH included in the quantitative analysis shown in Fig. 3.4 to determine the levels of each protein in the brain of three different mice for each genotype. In both panels, the dashed box indicates the cropped area shown in Fig. 3.3b and Fig. 3.4a. Dots are drawn on the left hand side of each gel where molecular weight markers were; pertinent sizes are indicated. For the $Ca_V2.2$ blot in (**a**), the molecular weight markings show as white dots, in all other gels they are black.

Table 3.1

Cross	ab/aa* x ab/aa*	ab/b*b x ab/b*b
# Litters	53	60
# Progeny	367	381
Avg. Litter Size	6.9	6.4
Homozygous	54	95
Heterozygous	186	190
Wildtype	115	91
# Homozygotes dead @ weaning	12	5
Ratio of Progeny Observed* (mut/mut:wt/mut:wt/wt)	0.5 : 1.6 : 1.0	1.0 : 2.1 : 1.0
*Ratio of Progeny Expected (1 : 2 : 1)		

Table 3.1

Survival of progeny from crosses of heterozygous *Cacna1b* mutant mice

CHAPTER 4

THE INHIBITION OF NEURONAL CALCIUM ION CHANNELS BY TRACE LEVELS OF YTTRIUM RELEASED FROM CARBON NANOTUBES

Lorin Jakubek and Spiro Marangoudakis contributed equally to the writing of this article

This chapter has been published as: Jakubek L, **Marangoudakis S**, Raingo J, Liu X, Lipscombe D, Hurt R.(2009). The inhibition of neuronal calcium ion channels by trace levels of yttrium released from carbon nanotubes. *Biomaterials*. Oct;30(31):6351-7.

I was responsible for all of the electrophysiology shown in Figures 4.1b-f, 4.3

Lorin Jakubek was responsible for the concept and Figures 4.1a, 4.2 and 4.5

Jesica Raingo was responsible for the early electrophysiological findings

Xinyuan Liu was responsible for the data in Figure 4.4

Acknowledgements

The authors are grateful for financial support from the National Institutes of Health (NS29967 and SBRP grant P42 ES013660), the US National Science Foundation (DMI-050661) and the US Environmental Protection Agency (RD-83386201).

Abstract

Carbon nanotubes (CNTs) are used with increasing frequency in neuroengineering applications. CNT scaffolds are used to transmit electrical stimulation to cultured neurons and to control outgrowth and branching patterns of neurites. CNTs have been reported to disrupt normal neuronal function including alterations in endocytic capability and inhibition of ion channels. Calcium ion channels regulate numerous neuronal and cellular functions including endo and exocytosis, neurite outgrowth, and gene expression. Strong CNT interactions with neuronal calcium ion channels would have profound biological implications. Here we show that physiological solutions containing CNTs inhibit neuronal voltage-gated calcium ion channels in a dose-dependent and CNT sample-dependent manner with IC_{50} as low as 1.2 μg/ml. Importantly, we demonstrate that the inhibitory activity does not involve tubular graphene as previously reported, but rather very low concentrations of soluble yttrium released from the nanotube growth catalyst. Cationic yttrium potently inhibits calcium ion channel function with an inhibitory efficacy, IC_{50}, of 0.07 ppm w/w. Because of this potency, unpurified and even some reportedly ‘‘purified’’ CNT samples contain sufficient bioavailable yttrium to inhibit channel function. Our results have important implications for emerging nano-neurotechnology and highlight the critical role that trace components can play in the biological response to complex nanomaterials.

Introduction

Carbon nanotubes show promise as scaffolds for neuronal growth (Mattson et al., 2000; Hu et al., 2004; Ni et al., 2005; Seidlits et al., 2008) and stimulation (Lovat et al., 2005; Mazzatenta et al., 2007; Schrlau et al., 2008; Cellot et al., 2009), nano-pipettes for cell delivery and sampling (Schrlau et al., 2008), and electrode coatings for enhanced recording (Keefer et al., 2008). Keefer and colleagues recently reported that metal wire electrodes can be coated with CNTs to enhance charge transfer, recording, and electrical stimulation of neurons at the brain-machine interface (Keefer et al., 2008). Intelligent design of this interface may enable the treatment of epilepsy, depression, and Parkinson's disease; and provide hope for restoration of function in paralysis (Hochberg et al., 2006; Keefer et al., 2008).

Essential to the success of CNTs in neurotechnologies is their successful integration with electrically active cells. Studies of the patterns of neurites grown upon CNT scaffolds (Mattson et al., 2000; Hu et al., 2004) have revealed altered neurite outgrowth. Additionally, neurons grown in the presence of water soluble SWNTs demonstrated similar outgrowth patterns to those grown upon CNT scaffolds (Ni et al., 2005) possibly resulting from interference of stimulated endocytosis from CNTs in the cell external solution (Malarkey et al., 2008). Each of these studies suggests that CNTs alter calcium-dependent cellular functions of growing neurons. An earlier study suggests that SWNTs can physically occlude ion channels (Park et al., 2003). The present study was therefore designed to fundamentally assess and characterize the possible effects of CNTs on voltage-gated calcium ion channels, which are present in all excitable cells

and underlie many essential cellular functions. In neurons, these channels control calcium entry that triggers transmitter release, gene expression, neuronal excitability, and growth cone extension. Dysfunctional voltage-gated calcium ion channels are implicated in a number of diseases and disorders, and are the targets of many pharmaceutical drugs and neurotransmitters.

Results

We used a human embryonic kidney cell line, tsA201, to express the cloned neuronal $Ca_V2.2$ N-type calcium ion channel chosen for its established role in regulating neurite outgrowth, transmitter release, and neuronal signaling (Raingo et al., 2007; Catterall and Few, 2008). This technique avoids current from other types of channels and thus isolates the function of the $Ca_V2.2$ N-type calcium ion channel. Calcium currents originating from synchronous activation of $Ca_V2.2$ channels were recorded using the whole-cell patch clamp recording method (Figure 4.1a, and Supplemental). We exposed cells to physiological solutions containing different concentrations of water soluble (aryl-sulfonate functionalized (Yan et al., 2006)) arc-synthesized single-walled carbon nanotubes (SWNTs) and monitored the magnitude and voltage-dependence of calcium currents.

Calcium currents were inhibited rapidly when cells were exposed to SWNT-containing solutions (Figure 4.1b; sample ‘‘A’’). Inhibition was dose-dependent (Figure 4.1c) and apparent at all voltages without altering the voltage-dependence of channel activation (Figure 4.1e). The magnitude and speed of inhibition were unexpected and indicative of

direct inhibitory effects on the calcium ion channel (Figure 4.1b). We removed the SWNTs from solution through centrifugal ultrafiltration and, surprisingly, observed an almost equivalent level of inhibitory activity (Figure 4.1d), which was similar in time course to the action of the original SWNT-containing solution (Figure 4.1c). This inhibition occurs in the absence of the original nanotubes.

The inhibitory action of the supernatant indicates a mechanism involving nanotube-induced alteration of the fluid medium, rather than direct interaction between tubular graphene and the ion channel or other cellular targets. High-surface-area SWNTs have been shown to significantly alter cell culture medium through adsorption of folic acid (Guo et al., 2007) and molecular probes (Worle-Knirsch et al., 2006) and can release soluble metal forms (Kagan et al., 2006; Liu et al., 2007; Pulskamp et al., 2007) through oxidative attack on metal catalyst residues that are not fully encapsulated by graphenic carbon shells (Liu et al., 2007; Liu et al., 2008). To assess the role of metals, we therefore tested the effects of SWNT B, a sample determined to be unusually well purified with respect to free metal (Figure 4.2c and d). Physiological solutions containing SWNT B had no detectable inhibitory activity on voltage-gated calcium channels up to 100 µg/ml (Figure 4.1f). Since the supernatant of SWNT A had similar inhibitory capability to SWNT A containing solutions, and the unusually well purified sample SWNT B did not have any inhibitory action, this strongly suggests a metals effect rather than an alteration of the buffer composition through adsorption.

The nanotubes in our studies were fabricated using a nickel–yttrium catalyst, and abundant metal nanoparticles are visible in both SWNT samples by TEM (Figure 4.2). Previous studies have reported that a small portion of CNT-imbedded metal is typically fluid accessible through defective carbon shells, and can become solubilized in physiological buffers by slow oxidation (Liu et al., 2007; Liu et al., 2008). This ‘‘bioavailable’’ metal fraction is not always eliminated by current purification protocols, and does not correlate well with total metal content (Liu et al., 2007; Liu et al., 2008). As both SWNT samples contain visible metal nanoparticles, we hypothesized that nickel and yttrium are released and solubilized into the recording solution in sufficient quantities to inhibit the channels from SWNT A but not B. We used inductively coupled plasma-atomic emission spectrometry (ICPAES) to measure levels of bioavailable nickel and yttrium (Figure 4.2c and d) in the recording solution (See Supplemental). Figure 4.2 shows that both SWNT samples contain bioavailable nickel, but only SWNT A contains detectable quantities of bioavailable yttrium.

We next tested the sensitivity of N-type calcium channels to nickel and yttrium cations in control salt solutions. Both metals inhibited calcium current rapidly, but yttrium was 300-fold more potent than nickel (nickel IC_{50} = 219 ± 40 µM; yttrium IC_{50} = 0.76 ± 0.15 µM; n = 3; Figure 4.3). Similar inhibitory effects of yttrium have been documented on native calcium channels and calcium-dependent processes (Nachshen, 1984; Mlinar and Enyeart, 1993; Beedle et al., 2002) consistent with inhibitory effects of other ions of the lanthanide series at protein calcium binding sites (Mlinar and Enyeart, 1993). Of the trivalent ions in the lanthanide series, yttrium is the most potent inhibitor of high voltage-

activated calcium channels (Beedle et al., 2002). Yttrium like cadmium, another potent inhibitor of high-voltage-activated calcium channels, is thought to inhibit calcium flow by competing for calcium-binding sites of the ion selectivity filter of the pore (Nachshen, 1984; Beedle et al., 2002; Sather and McCleskey, 2003) (see Figure 4.5).

To characterize the factors governing yttrium release from nanotubes, we included two additional SWNT samples (C and D) and studied the location, form, and behavior of CNT-associated yttrium. SWNT C has been commercially functionalized with carboxylate groups. SWNT D was included to show that significant concentrations of bioavailable metal may remain in vendor purified samples. A majority of CNT-associated metal in these samples is in the form of metal-rich nanoparticles encapsulated by thin carbon shells of variable thickness (Figure 4.4). Partial oxidation of SWNT D was carried out to simulate oxidative purification processes for removal of amorphous carbon by heating. Air oxidation attacks carbon shell structures (See Supplemental), greatly increasing the mobilization of Y and Ni into media (Figure 4.4c). The dissolved Y:Ni ratio is much higher than the initial condensed-phase Y:Ni ratio of 1:7. This indicates preferential oxidation and solution release of Y over Ni, consistent with the higher oxidation potential of Y (2.37 V (Horovitz and Birmingham, 1999)) relative to Ni (0.25 V). While SWNT D has been ‘‘purified’’ by the supplier, it nevertheless contains sufficient free Y to inhibit channel function, even before air oxidation is employed to remove carbon shells and increase metal bioavailability (~10 μM at zero carbon loss in Figure 4.4c, which by Figure 4.3f, is 13 times the IC_{50} of Y).

In samples subjected to acid purification, yttrium salt re-deposition on surface functional groups is also possible and may be an unappreciated source of bioavailable metal in nanotubes. Figure 4.4d shows that sulfonate and carboxylate functional groups introduced on CNTs can bind soluble yttrium from solution. The adsorption isotherms in panel 4.4e were used to derive fundamental equilibrium constants for yttrium binding to CNT-carboxylate (See Supplemental) and the competitive effects of Na^+ binding on yttrium adsorption from saline solutions. We report dissociation constants: Kd = 1.2 µM (for Y^{3+} /SWNT-COO^-); and Kd = 9060 µM (for Na^+/ SWNT-COO^-). The low Kd for soluble Y is consistent with the expected strong binding of the hard Lewis acid Y^{3+} to the hard carboxylate anion. This strong binding allows significant Y^{3+} adsorption to occur even in the presence of Na^+, which is the major ion in physiological saline (~1500 factor higher concentration than yttrium). The Kd for Ca^{2+} (Ca^{2+}/SWNT-COO^-) is 26.5 µM (Liu et al., 2008), which is also much higher than Kd for Y^{3+} (1.2 µM), implying that Y^{3+} has the potential to replace Ca^{2+} on carboxylic binding sites.

Discussion

Figure 4.5 summarizes our findings on the chemical pathways for yttrium responsible for SWNT-induced channel inhibition. Included in Figure 4.5 is a set of calculated curves derived from the combined data set that give quantitative estimates of the contribution of CNT derived yttrium and nickel to the overall inhibition seen in the whole nanotube sample. SWNT-derived yttrium can account for the inhibition within experimental error, while nickel is not a factor in this dose range. The slight difference between the whole nanotubes and the yttrium salt solutions may be due to differences in yttrium speciation

or cooperative (synergistic) effects of Y and Ni, which were not studied here. The difference cannot reflect a contribution from tubular graphene, because the nanotube-free supernatant shows the same behavior as the whole nanotubes (Figure 4.1d) and the nanotube sample with ultra-low-yttrium (B) shows no inhibition (Figure 4.1f) even when all the tubular graphene is present.

The potency of yttrium as a channel blocker is not unexpected, and is likely due to strong yttrium/carboxylate binding, as already discussed for the case of carboxylate groups on nanotube surfaces. The putative selectivity filter within the ion conducting pore of high-voltage-gated calcium channels contains four glutamates, one contributed by each of the four domains of the channel (Sather and McCleskey, 2003) (Figure 4.5). The carboxyl residues of the glutamate side chains are thought to coordinate two calcium ions; creating the selectively filter and supporting ion permeation (Sather and McCleskey, 2003). Yttrium is likely to compete for and displace calcium ions from their binding sites within the ion pore without permeating the membrane. The ionic radii of calcium and yttrium are similar (0.99 and 0.90 Å, respectively) consistent with the proposal that they could occupy the same narrow binding site within the ion pore. Smaller ions like Ni (0.69 Å) have lower affinity perhaps because they cannot coordinate the carboxylate side of the selectivity filter as well as calcium, yttrium, and cadmium. If the trivalent yttrium has a higher binding affinity as compared to calcium, it will occlude calcium entry (Nachshen, 1984; Mlinar and Enyeart, 1993; Beedle et al., 2002). Unlike calcium, which is present at concentrations high enough to carry charge (2 mM), Y levels are insufficient to support significant current, so the net effect is current inhibition.

Our finding that CNT-yttrium blocks calcium ion channels has important implications for nanotube-enabled drug delivery, biolabeling, and tissue engineering in bone, muscle, nerve, and other excitable cells. Channel inhibition may also follow unintended nasal inhalation and translocation across the olfactory bulb to the brain (Oberdorster et al., 2005). The Ni:Y catalyst is the most common formulation in arc synthesized SWNTs today (Plata et al., 2008), and yttrium's high potency on voltage-gated calcium ion channels (IC_{50} of 70 ppb) suggests SWNTs at levels as low as 1 µg/ml (1 ppm w/w) could disrupt normal calcium signaling in neurons and other electrically active cells.

Our results also indicate that current purification practices do not reliably reduce free yttrium content to levels below 70 ppb; therefore effects on calcium signaling in neurons and other excitable cells may be expected from many arc-synthesized tubes. Tissue engineering applications may be especially sensitive to yttrium released from CNTs because nanotubes are close-packed in scaffolds or on substrates to produce high effective local nanotube concentrations in the near-cellular space. In light of our results, it is possible that soluble metals are the underlying cause of some literature reports of calcium-dependent effects and nanotube induced ion channel blocking. We note, however, that many studies of nanotube/neuronal interactions use other nanotube types that do not contain yttrium, and thus cannot trigger the mechanism reported here (see for example (Cellot et al., 2009), which uses MWNTs grown using an Fe catalyst). In general, the influence of metal ions in CNT/ neuroengineering studies will be highly variable and dependent on the specific nanotube material and its processing history.

Future studies should carefully control for the release of metal ions, especially yttrium, to ensure proper interpretation of the observed interaction between nanotubes and electrically active cells.

Conclusions

Aqueous suspensions of arc-synthesized single-wall carbon nanotubes are observed here to inhibit neuronal calcium ion channels at low nanotube doses. The electrophysiological characterization of the nanotube suspensions combined with the control experiments using supernatant solutions and salt solutions clearly show that this inhibition is not due to tubular graphene, the primary nanotube structure, but rather bioavailable yttrium released from the nanotube catalyst. Yttrium is such a potent inhibitor of high-voltage-gated calcium ion channels (IC_{50} of 0.76 μM or 0.07 ppm w/w) that yttrium related effects on excitable cells are likely to occur for other arc synthesized SWNT samples. The present finding highlights the complexity of nanomaterial samples and the potential for secondary or trace material features to trigger adverse biological responses.

Methods

2.1 Source, processing, and characterization of SWNTs

A variety of commercial arc-synthesized SWNTs were acquired, characterized, and labeled SWNT A–D. Samples B–D were described by the vendor as ‘‘purified’’ and sample A ‘‘as-produced’’. Sample C was supplied in functionalized form with 4–6 atom-% carboxylate groups. To obtain uniform suspensions in the electrophysiology buffer,

SWNTs were rendered hydrophilic through covalent functionalization with aryl-sulfonate groups. In brief, SWNTs were immersed in 8.4 mM sulfanilic acid solution at 70°C. While maintaining constant temperature and agitation, 1.5 ml of 0.2 M sodium nitrite solution was added and allowed to incubate for 2 h. The SWNTs were subsequently washed with distilled water six times and dried at 100°C for 8 h. Aryl-sulfonated SWNTs were then suspended in external solution (see below) through mild bath sonication. Because functionalization may alter metal bioavailability, we performed the bioavailable metal assays (vida infra) after the functionalization step.

Transmission electron microscopy was carried out on JEOL 2010 high-resolution microscope at 200 kV and a Philips 420 microscope at 120 kV. Partial oxidation was carried out to simulate oxidative purification processes for removal of amorphous carbon by heating the carbon nanotubes in a TA Instrument 951 thermogravimetric analyzer at 10°C/min followed by a 60 min isothermal hold at target temperature. X-ray diffraction analysis of the TGA residues was performed on a Bruker AXS D8 Advance. To remove functional groups on the surface for selected experiments, a ceramic boat was placed in a bench-top tube furnace and purged with nitrogen for 30 min before raising the furnace temperature to 1000°C for 60 min hold time. The furnace was allowed to cool under nitrogen to room temperature.

2.2. Transient expression of $Ca_V2.2$ calcium channels in tsA201 cell line

Calcium channel subunits $Ca_V2.2$ (AF055477(Lin et al., 1997)) together with $Ca_V\beta_3$ (sequence homologous to M88751), $Ca_V\alpha_2\delta_1$ (AF286488 (Lin et al., 2004)), and

enhanced green fluorescent protein cDNAs (eGFP; BD Bioscience) were transiently expressed in tsA201 cells as described previously using Lipofectamine 2000 (Invitrogen) (Thaler et al., 2004).

2.3. Cell studies

Prior to cell exposure, SWNTs were dispersed through 2 hr bath sonication in the identical cell external solution (CES) used in the electrophysiology experiments. The solution in the electrophysiology chamber was then replaced with the external solutions containing varying doses of SWNTs. The supernatant sample was generated by transferring the sonicated suspensions to a 5000 NMWL Amicon Ultra- Centrifuge tube (Millipore, MA) and subjecting the samples to centrifugal ultrafiltration at 4500 rpm and 4^{o}C for 30 min. We have shown that this protocol removes essentially all of the nanotubes (Liu et al., 2007).

2.4. Electrophysiology

Calcium currents were recorded using the standard whole-cell patch clamp method as described previously (Thaler et al., 2004). The extracellular solution contained 1 mM $CaCl_2$, 4mM $MgCl_2$,10mM HEPES,135 mM choline chloride, pH adjusted to 7.2 with CsOH. The recording electrode solution contained 100 mM CsCl, 10mM EGTA, 1 mM EDTA, 10 mM HEPES, 4 mM MgATP, pH 7.2 with CsOH. Recording electrodes had resistances of 2–4 MΩ when filled with internal solution. Series resistances (<6 MΩ for whole-cell recording) were compensated 70–80% with a 10 μs lag time. Calcium currents were evoked by voltage-steps and currents leak subtracted on-line using a P/-4

protocol. Data were sampled at 20 kHz and filtered at 10 kHz (-3dB) using pClamp V8.1 software and the Axopatch 200A amplifier (Molecular Devices). All recordings were obtained at room temperature. Cells were typically held at -100 mV to remove closed-state inactivation before applying test pulses 20–25 ms in duration every 6 s (Thaler et al., 2004).

2.5. Assays for metal bioavailability and cation surface binding

Metal bioavailability (mobilization) assays were performed by dispersing the SWNTs in the identical cell external solution used in the electrophysiology experiments or in lysosomal simulant fluid at pH 5.5 (acetate buffer) and removing the SWNTs through centrifugal ultrafiltration (See Cell Studies). Nickel and yttrium content in the clear filtrate were measured by a Jobin Yvon JY2000 Ultrace inductively coupled plasma-atomic emission spectrometer (ICP-AES) as described previously (Liu et al., 2007). Measurements were made at a wavelength of 221.647 nm for Ni and 371.030 nm for Y and intensities were calibrated using standards ranging in concentration from 0 to 5 µg/ml for Ni and from 0 to 10 µg/ml for Y. ICP is accurate at concentrations down to 10 ppb. The interactions between yttrium cation and CNT surface functional groups were studied by adding 0.05–1.0 mg/ml SWNTs to - 0.1 mM YCl_3 aqueous solution (in DI water, saline or acetate buffer) and ultrasonicated in water bath for 1 h and rotated overnight at 60 rpm. The solids were then removed by centrifugal ultrafiltration and the filtrate analyzed for Y by ICP as above.

Figure 4.1

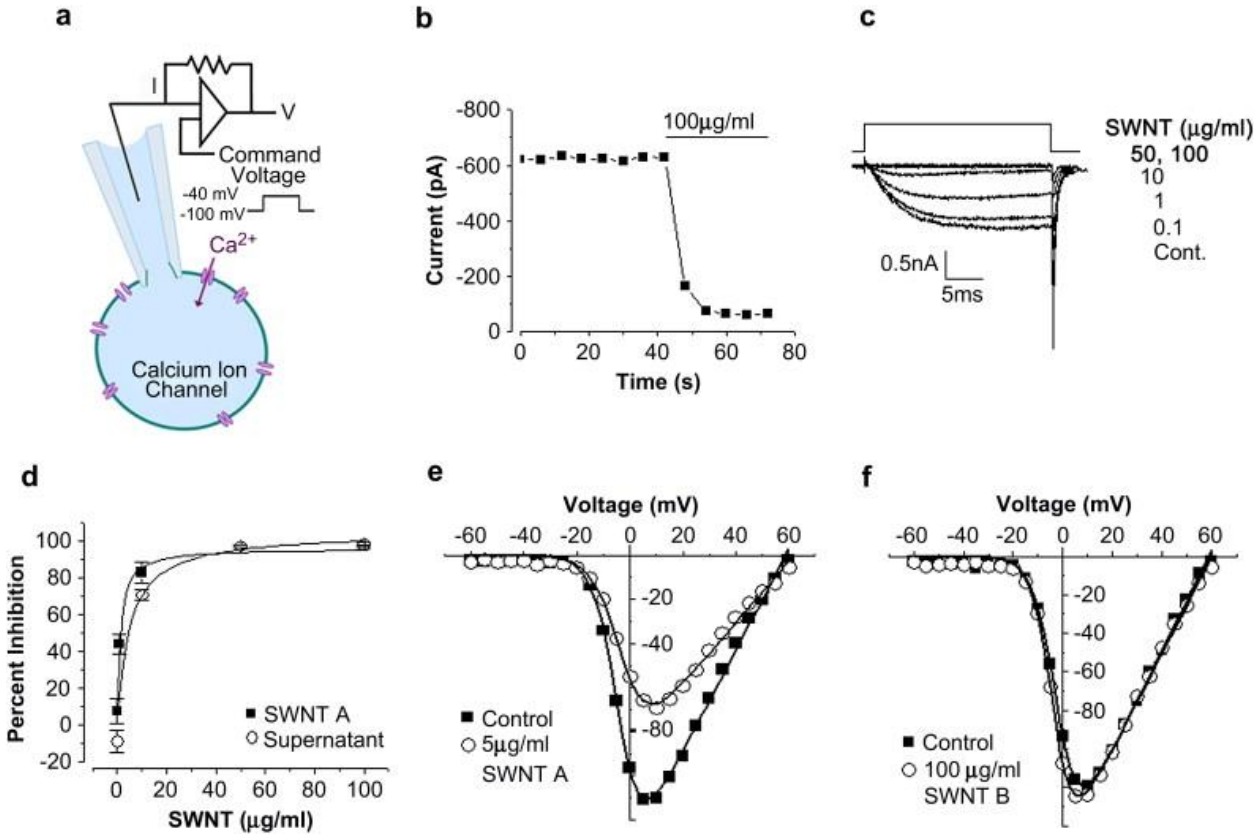
a
I
V
Command Voltage
-40 mV
-100 mV
Ca2+
Calcium Ion Channel
b
100µg/ml
Current (pA)
-800
-600
-400
-200
0
0 20 40 60 80
Time (s)
c
SWNT (µg/ml)
50, 100
10
1
0.1
Cont.
0.5nA
5ms
d
Percent Inhibition
100
80
60
40
20
0
-20
0 20 40 60 80 100
SWNT (µg/ml)
SWNT A
Supernatant
e
Voltage (mV)
-60 -40 -20 0 20 40 60
-20
-40
-80
Control
5µg/ml
SWNT A
f
Voltage (mV)
-60 -40 -20 0 20 40 60
-20
-40
-60
-80
Control
100 µg/ml
SWNT B

Figure 4.1

SWNT sample A inhibits calcium ion channels, while SWNT sample B does not. **(a)** Schematic of whole-cell patch clamp experiment. **(b)** Time course of calcium current under constant voltage step exposed to 100 µg/ml SWNT A. Horizontal bar indicates the time of nanotube application. **(c)** Calcium current traces from cell exposed to 0.1, 1, 10, 50 and 100 µg/ml SWNT A. *X* axis is time in ms and the *Y* axis is calcium current in mA. **(d)** Dose response of calcium current inhibition resulting from exposure to varying concentrations of SWNT A (solid squares) and associated supernatant (i.e. nanotube-exposed buffer solution after nanotube removal) (open circles). Strong inhibition is seen even in the CNT-free supernatant. Error bars represent standard error (n = 3). SWNT A data fit with a hyperbolic non-linear curve, $y = 96.3x/(1.22 + x)$; the IC_{50} of SWNT A is 1.22 µg/ml ± 0.13. The supernatant is fit with hyperbolic non-linear curve $y = 105x/(5.0 + x)$ and the associated IC_{50} is 5.00 µg/ml ± 2.3. **(e)** Entering calcium current as a function of command voltage over the range −60 mV–60 mV of control (solid square) and 5 µg/ml SWNT A exposed cell (open circle). The maximum current observed in the control cell occurred at 5 mV and is −111 pA/pF. The maximum current after exposure to 5 µg/ml SWNT A is at 10 mV and is −69.4 pA/pF. **(f)** Entering calcium current as a function of command voltage over the range −60 mV–60 mV of control (solid square) and 100 µg/ml SWNT B exposed cell (open circle). Maximum current of −119 pA/pF was observed at 10 mV in control and −125 pA/pF at 5 mV after exposure to SWNT B. Panel 4.1a adapted from Dunlop *et al*. Nature Reviews 2008 (Dunlop et al., 2008).

Figure 4.2

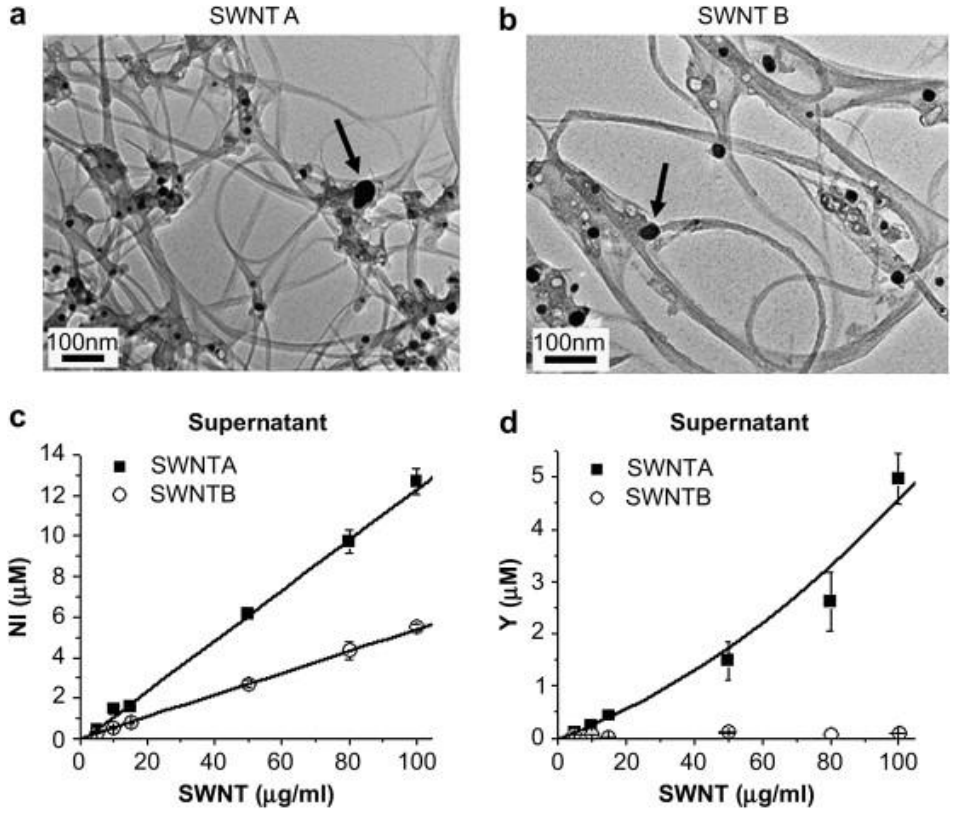
a
SWNT A
100nm
b
SWNT B
100nm
c
Supernatant
SWNTA
SWNTB
NI (μM)
SWNT (μg/ml)
d
Supernatant
SWNTA
SWNTB
Y (μM)
SWNT (μg/ml)

Figure 4.2

Bioavailable nickel and yttrium in SWNT samples. **(a, b)** Metal catalyst nanoparticles visible by TEM. Scale bar: 100 nm. Arrows point to catalytic particles. The total metal mass percentages by digestion and ICP-ES are 23.3% nickel and 5.77% yttrium for SWNT A, and 6.7% nickel and 1.3% yttrium for SWNT B. **(c, d)** Results of quantitative dose-dependent metal mobilization (bioavailability) assays. Figures give total soluble Ni and Y concentrations after SWNT samples were sonicated in CES buffer for 2 h at pH 7.2 followed by centrifugal ultrafiltration and ICP analysis of the filtrate. These were the same conditions used for electrophysiological characterization. Error bars represent standard deviation from triplicate determination.

Figure 4.3

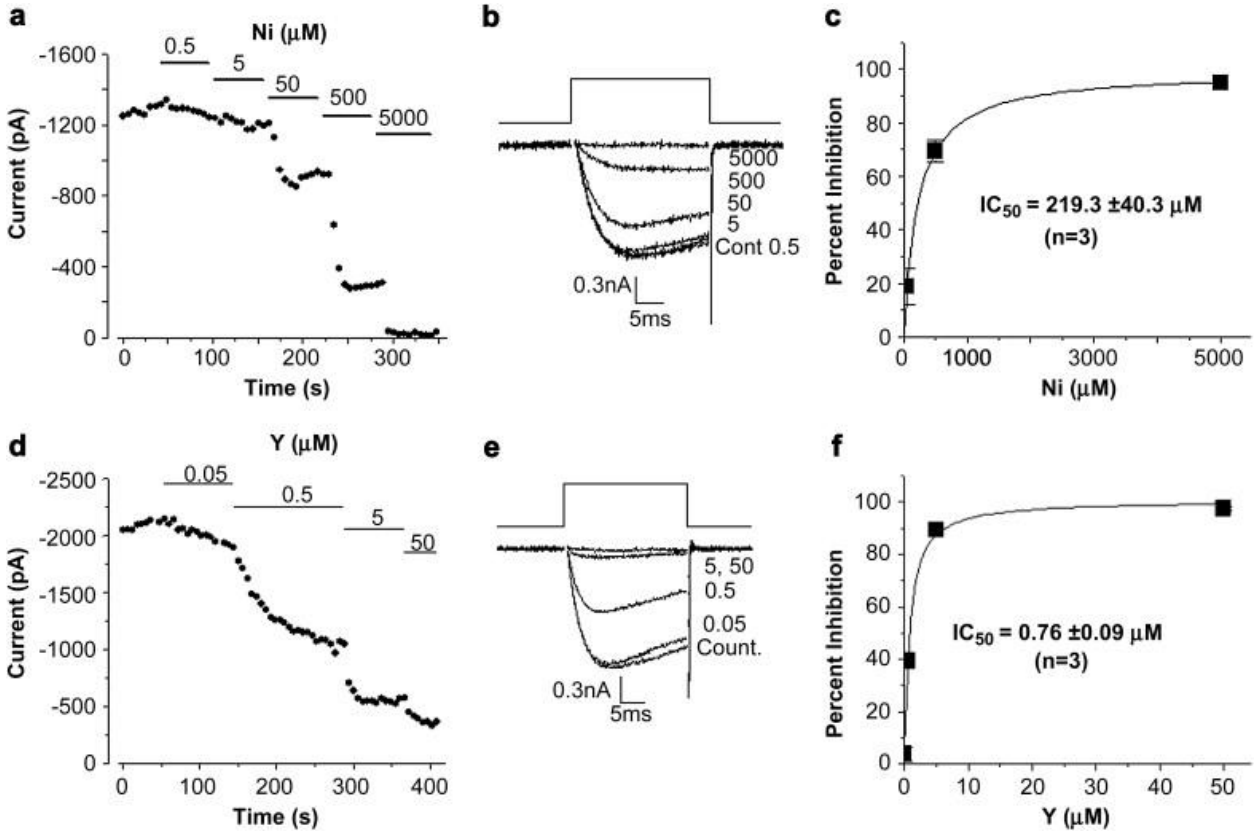
a
Ni (μM)
0.5
5
50
500
5000
Current (pA)
-1600
-1200
-800
-400
0
0
100
200
300
Time (s)
b
5000
500
50
5
Cont 0.5
0.3nA
5ms
c
Percent Inhibition
100
80
60
40
20
0
IC50 = 219.3 ±40.3 μM
(n=3)
0
1000
3000
5000
Ni (μM)
d
Y (μM)
0.05
0.5
5
50
Current (pA)
-2500
-2000
-1500
-1000
-500
0
0
100
200
300
400
Time (s)
e
5, 50
0.5
0.05
Count.
0.3nA
5ms
f
Percent Inhibition
100
80
60
40
20
0
IC50 = 0.76 ±0.09 μM
(n=3)
0
10
20
30
40
50
Y (μM)

Figure 4.3

Control experiments with soluble salts isolate the effects of Ni and Y on neuronal voltage-gated calcium ion channels. **(a–c)** Nickel effects. **(a)** Time course showing decreasing calcium current with increasing nickel dose. Solid bars represent time and dose of application. **(b)** Representative traces of nickel inhibition across the range 0.5–5000 μM. **(c)** Nickel dose response curve fit with a hyperbolic non-linear function of the equation: $y = 99.3x/(219.3 + x)$. From these results, the IC_{50} for nickel inhibition of $Ca_V2.2$-type neuronal calcium channels is 219 μM. **(d-f)** Yttrium effects. **(d)** Time course showing decreasing calcium current with increasing dose of yttrium. Solid bars represent time and dose of application. **(e)** Representative traces of yttrium inhibition across the range 0.05–50 μM. **(f)** Yttrium dose response curve fit with a hyperbolic non-linear function of equation: $y = 100.7x/(.76 + x)$. From these results, the IC_{50} for yttrium inhibition of $Ca_V2.2$-type neuronal calcium channels is 0.76 μM. Yttrium is an extremely potent calcium ion channel blocker.

Figure 4.4

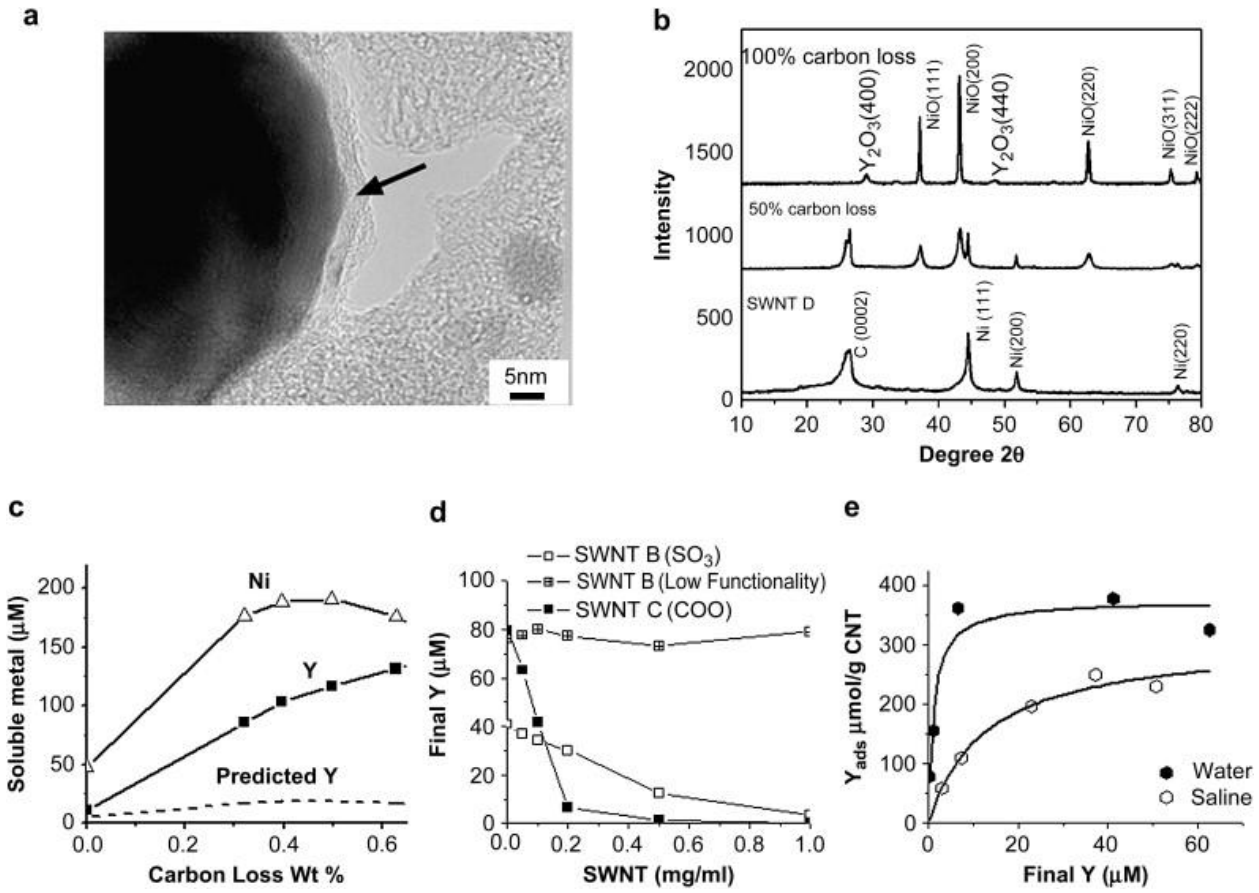
a
5nm
b
100% carbon loss
50% carbon loss
SWNT D
Intensity
Degree 2θ
c
Ni
Y
Predicted Y
Soluble metal (μM)
Carbon Loss Wt %
d
SWNT B (SO3)
SWNT B (Low Functionality)
SWNT C (COO)
Final Y (μM)
SWNT (mg/ml)
e
Water
Saline
Yads μmol/g CNT
Final Y (μM)

Figure 4.4

Yttrium phases in SWNTs and mechanisms of yttrium ion release and recapture by SWNT surface functional groups. **(a)** Typical metal catalyst morphology in arc-synthesized SWNT (sample D): Ni/Y nanoparticles are encapsulated in thin (2–10 nm) carbon shells (arrow). Previous studies on nanotube nickel and iron show that carbon shells protect most but not all metal from fluid-phase attack by dioxygen or protons that leads to oxidation and soluble ion release (Liu et al., 2007; Guo et al., 2008; Liu et al., 2008). **(b)** X-ray diffraction spectra show that most metal is in the form of zero-valent metal nanoparticles with nickel lattice spacing, which upon extensive dry air oxidation can be converted to separate NiO and Y_2O_3 phases. **(c)** Effect of controlled air oxidation of SWNT D on metal phases and ionic release into a cellular lysosomal simulant buffer at pH 5.5 (2 hr incubation at room temperature of 1.0 mg/ml SWNTs). The dashed curve gives the soluble Y concentration expected if the release were proportional to the Ni release at the initial Ni:Y ratio of 7:1 w/w. SWNT D is marketed as purified and contains a total metal content of 14.3 wt% Ni and 2.1 wt% Y by independent analysis. **(d, e)** Fundamental adsorption isotherms that characterize the interactions of soluble yttrium with nanotube surface functional groups. **(d)** sulfonated and carboxylated nanotubes remove yttrium ion from solution by surface binding, while the graphenic surfaces of unfunctionalized nanotubes have little effect. **(e)** Adsorption isotherms for yttrium ion binding on SWNT-COOH in pure water and saline. p*K*a of these COOH groups determined here to be 3.5 by mass titration. Panel E data allow estimation of the fundamental equilibrium constants for competitive Y^{3+}/Na^{+} binding (see

dashed curves and analysis in Supplemental). K_d = 1.2 μM (for Y^{3+}/SWNT-COO^-); and K_d = 9060 μM (for Na^+/SWNT-COO^-).

Figure 4.5

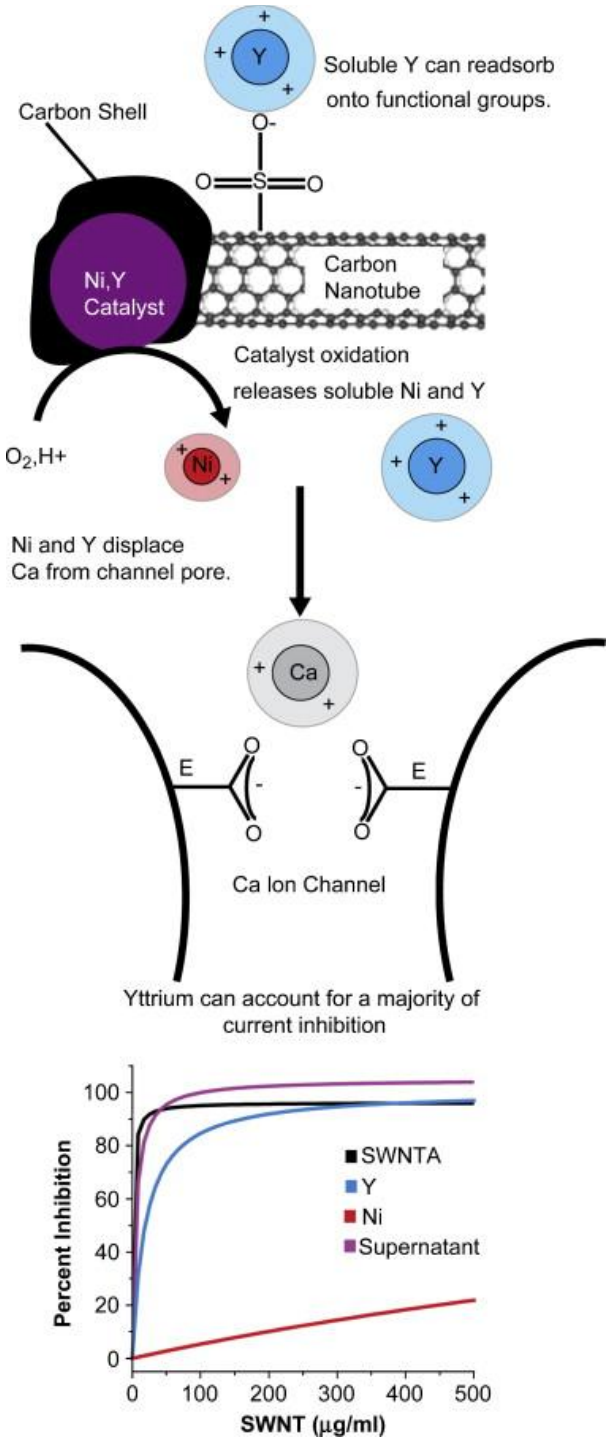
Y
Soluble Y can readsorb
onto functional groups.
Carbon Shell
O-
O=S=O
Ni,Y
Catalyst
Carbon
Nanotube
Catalyst oxidation
releases soluble Ni and Y
O2,H+
Ni
Y
Ni and Y displace
Ca from channel pore.
Ca
E
O
O
-
O
O
-
E
Ca Ion Channel
Yttrium can account for a majority of
current inhibition
Percent Inhibition
100
80
60
40
20
0
0
100
200
300
400
500
SWNT (µg/ml)
SWNTA
Y
Ni
Supernatant

Figure 4.5

Summary of proposed mechanism through which carbon nanotube suspensions inhibit neuronal calcium ion channels. Nickel–yttrium catalyst nanoparticles (Purple) are oxidatively corroded by fluid-phase attack through defects or cracks in the surrounding carbon shells leading to solubilization of nickel (Red) and yttrium (Blue) into the media. Purification protocols reduce but do not typically eliminate this bioavailable metal. For functionalized nanotubes, soluble metal can become re-associated during purification or processing by adsorption onto anionic functional groups, to become an additional source of bioavailable metal in nanotube samples (Liu et al., 2008). Nickel and especially yttrium ions in solution compete with and displace calcium ions (Gray) from the channel pore. The putative selectivity filter of the calcium ion channel consists of four glutamate residues (E). Two glutamates are shown pointing into the calcium ion pore, creating a calcium ion binding site which is predicted to be part of the ion selectively filter (Sather and McCleskey, 2003). Calcium is believed to coordinate these residues to enable both high throughput permeability and ion selectivity of the channel. Yttrium cation has a similar ionic radius to calcium, and thus exhibits a good geometric match to the selectivity filter, but is trivalent and has a higher binding coefficient for carboxyl residues than calcium, likely leading to its very high potency as a channel inhibitor. Nickel has a smaller ionic radius than calcium suggesting it is unable to coordinate the carboxyl side chains as effectively as calcium and yttrium consistent with its lower potency as an inhibitor (Nachshen, 1984). The figure (bottom) shows model curves generated from our combined data (Figure 4.1, Figure 4.2 and Figure 4.3) in order to estimate the contribution

of yttrium and nickel to the overall inhibition by the whole SWNT A sample. The SWNT A inhibition curve is forecast from our experimental data. The equation of the curve (from Figure 4.1d) is $SWNT\_A_{inh} = 96.3x/(1.22 + x)$ with IC_{50} 1.22 µg/ml SWNT A. Similarly, the equation of the supernatant curve (Figure 4.1d) is $y = 105x/(5.0 + x)$ with IC_{50} of 5.0 µg/ml SWNT A. The concentration of yttrium released from higher doses of SWNT A is given by $Y_{conc} = .04[SWNT\_A]$. These yttrium concentrations are then substituted into the inhibition curve provided in Figure 4.3f. The inhibition associated with each yttrium concentration is shown as a function of corresponding SWNT A concentration to yield the inhibition model shown by equation $Y_{inh} = 100.7x/(19.0 + x)$ with IC_{50} 19.0 µg/ml SWNT A. The concentration of nickel released from higher doses of SWNT A is given by $Ni_{conc} = .124[SWNT\_A]$. These nickel concentrations are then substituted into the inhibition curve provided in Figure 4.3c. The inhibition associated with each nickel concentration is shown as a function of corresponding SWNT A concentration to yield the inhibition model shown by equation $Ni_{inh} = 99.3x/(1768.5 + x)$ with IC_{50} of 1768.5 µg/ml SWNT A. It is evident that yttrium is responsible for a majority of the channel inhibition during nanotube exposure. We find no evidence that the tubular graphene structure is involved in channel inhibition.

Supplemental Information

for Jakubek et al., “Neuronal voltage-gated calcium ion channels are inhibited by trace yttrium released from carbon nanotubes”

Whole Cell Patch Clamp Technique

The whole cell patch recording method is used to measure currents from small cells while maintaining constant voltage (voltage-clamp). In this method inward calcium currents are activated by test voltages applied at values between -60 mV and +60 mV from a holding potential of -100 mV. Characteristic time-dependent changes in current are exemplified by current traces shown in Figure 4.1c. The maximum current vs. test voltage relationship is U-shaped (Figure 4.1e). Inward current increases with stronger test depolarization because of the steep dependence of channel open probability on voltage. However, the concomitant decrease in driving force on calcium ions with depolarization acts to decrease current flow through each individual channel. The inward current is eventually balanced by an equal and opposite outward current at the channel reversal potential of close to +60 mV (Figure 4.1e).

Analysis of competitive metal binding to CNT-carboxylate functional groups

The metal adsorption isotherms in Figure 4.4e were used to determine equilibrium constants for soluble yttrium binding to CNT-carboxylate, both in DI water and in saline where Na^+ ions compete for the same sites. The relevant reaction and binding equilibrium constant are:

$$Y^{3+} + CNT - COO^- \leftrightarrow CNT\text{-}COOY^{2+} \qquad (S1)$$

$$K_Y = \frac{[\text{CNT-COOY}^{2+}]}{[\text{CNT-COO}^-][Y^{3+}]} = \frac{N_Y}{(N_{max} - N_Y)[Y^{3+}]} \qquad \text{(S2)}$$

where N_Y is the number of bound sites, N_{max} is the total number of surface carboxylic sites, and $[Y^{3+}]$ represents here the total concentration of all soluble yttrium species at equilibrium. Relation S2 fits the experimental isotherm of Figure 4.4f well giving N_{max}=0.37 mmol/g and K_Y = 857 l/mmol. Expressed as a dissociation constant: K_d = $1/K_Y$ = 1.2 μM, which is the soluble yttrium concentration at which 50% of the available carboxylic sites will be occupied. From Figure 4.2d, yttrium mobilization into the electrophysiology buffer achieves higher concentrations than 1.2 uM, indicating that CNT-surface-bound Y^{3+} is likely another source of bioavailable Y (beyond the discrete nanoparticles), and may explain why whole SWNT suspension has a slightly stronger calcium ion channel inhibitory effect than the supernatant alone (where the CNT-surface-bound yttrium is absent).

In physiological solutions yttrium must compete with other ions for carboxylate binding sites on nanotubes and in the selectivity filter in the ion channel pore. Here simple experiments were conducted in saline solution to probe the competitive binding of yttrium and sodium on CNT-carboxylates. Figure 4.4e shows that total yttrium binding from 80 μM solutions is reduced but still significant in the presence of 154 mM Na^+, allowing a quantitative analysis of competitive binding. In Y-doped saline two equilibrium expressions must be satisfied simultaneously:

$$K_Y = \frac{[\text{CNT-COOY}^{2+}]}{[\text{CNT-COO}^-][Y^{3+}]} = \frac{N_Y}{(N_{max} - N_Y)[Y^{3+}]} \qquad \text{(S3)}$$

$$K_{Na} = \frac{[CNT\text{-}COOY^{2+}]}{[CNT\text{-}COO^{-}][Na^{+}]} = \frac{N_{Na}}{(N_{max} - N_{Na} - N_{Y})[Na^{+}]} \qquad \text{(S4)}$$

Where K_Y, N_{max} were determined previously (857 l/mmol and 0.37 mmol/g respectively). At 154 mM, $[Na^+]$ is nearly constant since it is much higher than the initial (maximum) yttrium concentration (~0.1 mM). This leaves K_{Na} as the only unknown variable. Fitting the data in Figure 3.4e yields K_{Na} = 0.11 l/mmol, or a sodium dissociation constant K_d of 9060 μM and provides a satisfactory curve shape (see Figure 4.4e bottom line). Clearly yttrium binding continues in the presence of the abundant Na^+ ion, but is reduced from the pure water case by ion-ion competition.

Our reported dissociation constants (K_d = 1.2 μM for yttrium/SWNT-COO^-) can be compared to the reciprocal binding constants for Y^{3+} and $Y(OH)^{2+}$ reported by Turkel *et al.* in experiments on salicylic acid, which range from 0.1 to 1000 μM depending on the soluble yttrium species (Horovitz and Birmingham, 1999; Turkel et al., 1999). The metal speciation diagram for yttrium indicates Y^{3+} and $Y(OH)^{2+}$ under the neutral pH conditions of the CES buffer (Zotova et al., 1998).

CHAPTER 5

DISCUSSION

Our studies suggest that nociceptors of wild type mice express largely e37a-containing $Ca_V2.2$ channels on their surface

In earlier studies, our lab determined through single-cell RT-PCR that both e37a- and e37b-containing $Ca_V2.2$ mRNAs are expressed in nociceptors of wild-type rats (Bell et al., 2004). These tests confirmed the expression of e37a, however, these tests were qualitative, and thus could not determine the abundance of e37a and e37b transcripts within a single cell. Also, lacking isoform-specific antibodies, we could not directly study the resulting channel proteins, thus we do not know the exact proportion of each isoform on the cell surface. The results of both Chapter 2 and Chapter 3 however indicate that nociceptive neurons of the DRG likely predominantly express $Ca_V2.2$e[37a] channels over $Ca_V2.2$e[37b] channels on the cell surface. Studies of our transgenic mice (Chapter 3) indicate that although overall $Ca_V2.2$ protein levels in DRG of Cacna1b$^{aa*/aa*}$ mice are only ~ 12 % of those in wild type cells, the channel surface expression in these cells is roughly 30 % that of wild type cells (Figures 3.3, 3.5). This demonstrates that e37a channels can traffic exceptionally well to the cell surface. Also, the results of the behavioral tests shown in Figure 3.8 indicate that wild type and Cacna1b$^{aa*/aa*}$ mice exhibit the same response to morphine, namely increased sensitivity and reduced ability to transmit pain. This indicates that $Ca_V2.2$e[37a] channels may outcompete $Ca_V2.2$e[37b] channels for the cell surface in these neurons.

Additional results are consistent with this hypothesis. We treated nociceptive DRG neurons of Cacna1b$^{aa*/aa*}$ mice with MG132 and compared calcium currents to control cells. The data were excluded from our manuscript (Chapter 2, Figure 2.6) because of

low $Ca_V2.2$ currents inherent in neurons of Cacna1b$^{aa*/aa*}$ mice. However, these tests exactly matched the results from wild-type neurons shown in Figure 2.6E, i.e. there was no significant difference in current densities between cells treated with MG132 and vehicle alone. These data support the hypothesis that wild-type cells highly express $Ca_V2.2e[37a]$ channels on their cell surface, to the exclusion of $Ca_V2.2e[37b]$ channels. This result is interesting and may have wider reaching implications if human DRG neurons show the same properties. In the scope of morphine treatment, it may mean that humans may naturally be optimally susceptible to morphine, likely through VII, and that tolerance may thus prove to be a process by which $Ca_V2.2e[37a]$ channels are exchanged for $Ca_V2.2e[37b]$ channels that exhibit reduced susceptibility.

What type of Ub linkage is involved in $Ca_V2.2e[37b]$ ubiquitination?

The large size of $Ca_V2.2$ channels makes their ubiquitination difficult to characterize. For smaller proteins a western blot can clearly indicate whether monoubiquitination or polyubiquitination has occurred on a substrate. The large size of $Ca_V2.2$ (~ 260 kDa), prohibits this analysis; ubiquitinated $Ca_V2.2$ appears as a smear on the top of the blot, and determination of monoubiquitination from polyubiquitination becomes impossible. There are several ways to get around this issue. One way is to express Ub clones with lysine to arginine point mutations in one or more of the critical lysine residues (eg. K48R), and to look for a change in substrate ubiquitination. Another is to immunoblot using antibodies against ubiquitin chains. Both of these methods were tested, but they were both inconclusive, mostly due to the low abundance of ubiquitinated channel.

Because $Ca_V2.2e$[37b] surface channel expression increases after MG132 treatment, it is tempting to assume that the e37b-specific ubiquitin linkage is formed through K48. However, as mentioned in the introduction, we currently know that ubiquitin chains conjugated through almost any lysine can mediate proteasomal degradation, including through lysines: 6, 11, 27, 29, and 33 (Xu et al., 2009). Thus, even if we know that e37b channels are preferentially degraded by the proteasome, the exact chain responsible would still be unclear.

Additionally, the e37b-mediated ubiquitination mechanism could promote monoubiquitination of $Ca_V2.2e$[37b]. This could then lead to internalization and sequestration in recycling endosomes, or degradation through lysosomes (Hicke, 2001). The e37b-mediated ubiquitination may even restrict surface expression through abrogation of trafficking (d'Azzo et al., 2005). In either one of these scenarios, MG132 treatment could potentially rescue internally-held channels that would normally be degraded, and could allow them to traffic to the surface where they would be active. More tests will be required to determine the precise role of e37b-dependent ubiquitination.

What is the functional importance of the UBE1 interaction in the yeast two-hybrid assay?

The UBE1 interaction with e37b baits in the yeast two-hybrid assay is difficult to explain. We do not know if the interaction exists *in vivo* and the literature suggests that it likely does not (Hershko and Ciechanover, 1998). This is also supported by the fact that we

could not co-immunoprecipitate UBE1 with $Ca_V2.2$ in our tests (Figure 2.3). However, co-immunoprecipitation has limitations, and it may not detect weak and/or transient protein-protein interactions, thus we cannot be completely certain that these proteins do not interact *in vivo*.

It is interesting that all UBE1 clones isolated in our yeast two-hybrid screen contained the ubiquitin fold domain (UFD) (Figure 2.2). This shows that the UFD is required to mediate the interaction between UBE1 and e37b. Indeed the shortest of the UBE1 clones isolated in the yeast two-hybrid screen contain only the UFD (Figure 2.2, clones B4, B18). The UFD domain of UBE1 interacts with E2 *in vivo*, helping to mediate transfer of Ub from UBE1 to E2. (Schulman and Harper, 2009). Thus, it is possible that UFD prey constructs interact with native E2 proteins endogenous to yeast. It is also possible that only truncated UBE1 proteins that contain the UFD interact with $Ca_V2.2$ sequence. For example, the absence of N-terminal domains in UBE1 could increase association of the UFD with e37b baits. Recent work has also shown that E2 has the capacity to ubiquitinate substrate proteins in the absence of E3 ligases. It is therefore possible that UBE1 interacts with e37b in yeast via an endogenous E2/E3 protein bridging complex, or via an E2 bridge alone (Hochstrasser, 2007; Hoeller et al., 2007). The high conservation of proteins in the Ub pathway among distant species including yeast and mammals increases the likelihood that endogenous E2 and E3 proteins mediate the UBE1-e37b interaction in yeast (Sharp and Li, 1987; Glickman and Ciechanover, 2002; Hochstrasser, 2009).

As discussed in Chapter 2, other yeast two-hybrid screens have shown participation of endogenous yeast proteins in exogenous protein-protein interactions (Rzymski et al., 2008). In this study for example, the authors took advantage of this kind of bridging complex. They used the endogenous interacting yeast protein to isolate a mouse homologue normally responsible for bridging this interaction (Rzymski et al., 2008). Additionally, to help interpret our results, it would be interesting to know if the e37b bait is also ubiquitinated in yeast, and if ubiquitination of the e37b$_S$ bait differs from the e37a$_S$ bait.

Do studies of Ca$_V$2.2 ubiquitination *in vitro* correlate with studies *in vivo*?

Our *in vitro* studies of Ca$_V$2.2 correlate well with *in vivo* recordings of Ca$_V$2.2 channels in nociceptive neurons of the DRG. In Figure 2.6F we showed an increase in e37b channel currents in *Cacna1b* $^{b*b/b*b}$ DRG neurons following proteasome inhibition by MG132. This increase was very similar to the increase in currents observed in cell lines expressing e37b-containing Ca$_V$2.2 channels (~40% compared to control) (Figure 2.6B). These data suggest that ubiquitination of cloned channels in cell lines and native channels in neurons use similar mechanisms. It would be interesting to know how conserved the Ca$_V$2.2 ubiquitination machinery is, specifically the E3 ligases. This conservation might seem unlikely because tsA201 cells are derived from the human embryonic kidney (HEK293, HEK) cell line. However, microarray transcriptome profiling and immunostaining show that HEK293 cells are more similar to neurons than to kidney cells (Shaw et al., 2002). Based on these results, it is suggested that during development of the HEK293 cell line, a neuron was transformed and selected for over

the kidney cells. These conclusions were drawn from both the expression profile of HEK cells, and the reported resistance to transfection of non-neuronal cells with adenoviral DNA (Shaw et al., 2002).

Tyrosine 1747 in e37a: a key residue that controls ubiquitination and $G_{i/o}$ inhibition

In 2007, Jesica Raingo and others in the lab showed that Y1747 in $Ca_V2.2e[37a]$ was essential for the large current characteristic of these channels, and for $G_{i/o}$ protein-mediated inhibition by a voltage independent mechanism (Raingo et al., 2007). As reported here, I showed that this same tyrosine occludes e37b-dependent ubiquitination of the $Ca_V2.2$ protein (Figure 2.5). Mutating Y1747 to F1747 in $Ca_V2.2e[37a]$ reduces $Ca_V2.2$ current densities, occludes VII, and promotes ubiquitination. These data suggest that G protein inhibition, current density, and ubiquitination of $Ca_V2.2$ converge on a common mechanism. These could be linked if for example F1747 of $Ca_V2.2e[37b]$ channels promotes ubiquitination which somehow inhibits VII. Alternatively, it could be possible that phosphorylation of Y1747 in $Ca_V2.2e[37a]$ channels potentiates channels for G protein-mediated VII and inhibits ubiquitination. Additional experiments would be needed to test these possibilities. Understanding how these two pathways interact could be important in the development of new drugs for the treatment of chronic pain. For example, it may be possible to enhance the efficacy of morphine, which inhibits $Ca_V2.2$ through $G_{i/o}$ receptors, by also manipulating ubiquitination of the $Ca_V2.2$ channel. We know from our studies that $Ca_V2.2e[37a]$ channels are more potently inhibited by morphine than $Ca_V2.2e[37b]$ channels (Figure 3.7, 3.8). Thus, if we can shift surface

channel expression away from $Ca_V2.2e[37b]$, toward $Ca_V2.2e[37a]$, by activating the e37b-specific ubiquitination process, this may give morphine higher efficacy (Figure 3.7) (Andrade et al., 2010). This could be especially important if tolerance to morphine is indeed mediated by increased $Ca_V2.2e[37b]$ channel surface expression.

Potential significance of exon 20a in $Ca_V2.2$

E20a is an exon I discovered that encodes a stop in its last codon. Although it is currently unclear if this transcript is stable, due to the decreased stability of large transcripts with early stop codons (through NMD), it is likely that some level of protein is expressed, due to the requirement of a pioneering translation step before a mRNA molecule can be targeted for NMD (Chang et al., 2007). Also, although a short (~ 100 kDa, predicted) $Ca_V2.2$ hemichannel protein is not detected in western blots prepared from neuronal tissue (Figure 3.9, $Ca_V2.2$ blots), low molecular weight bands are routinely detected in western blots of $Ca_V2.1$, and expression of hemichannel products containing the first two domains of $Ca_V2.1$ have been verified by others (Figure 3.9, $Ca_V2.1$ blot, lower bands) (Scott et al., 1998; Arikkath et al., 2002). This indicates that hemichannels of various types may indeed play an important role in the cell.

The laboratory of Annette Dolphin and colleagues has shown that expression of a two domain $Ca_V2.2$ hemichannel results in decreased expression levels of full-length channels through ER retention and degradation (Raghib et al., 2001; Page et al., 2004). These hemichannels were however the result of an artificial stop codon placed in a $Ca_V2.2$ clone, and not expression of e20a. Thus, although it is possible that this

mechanism is biologically relevant, due to the expression system used, it is also possible that these results are largely due to overexpression of an artificial channel construct. In any case, the construct used lacked the 27-residue sequence specific to e20a, and thus lacked a potentially important sequence in its regulation. Indeed, the position of the stop codon indicates that the protein sequence may have a biologically functional role. Presumably, if it did not, a stop codon may have evolved 5' of its current position, rather than occupying the most 3' position. Thus, it appears that this exon may not solely exist to degrade its mRNA message. A further distinct possibility, and perhaps a long-shot, is that the e20a protein isoform forms a functional channel with unique properties, potentially as a multimer with other hemichannels. The unique 27-residue sequence may thus form a potential multimerization signal. Further studies will be required to determine the actual biological relevance of e20a.

APPENDIX

A.1

Table 1a

%	#		Protein Name	Acc#	Localization
0.8%	1	‡	adaptor-related protein complex AP-3, sigma 2 subunit	NM_001115039.1	Cytoplasm
1.5%	2		S-adenosylhomocysteine hydrolase (Ahcy)	NM_017201.1	Cytoplasm
0.8%	1	‡	adenylate kinase 1 (Ak1)	NM_024349.2	Cytoplasm
1.5%	2		aldo-keto reductase family 1, member A1 (Akr1a1)	NM_031000.2	NA
2.3%	3		aldolase A	NM_001177305.1	Cytoplasm
0.8%	1		aminoacylase 1 (Acy1)	NM_001005383.1	Cytoplasm
1.5%	2		amplified in osteosarcoma (Os-9)	NM_001007265.1	ER
0.8%	1		ankyrin repeat domain 49 (Ankrd49)	NM_001126283.1	NA
1.5%	2		armadillo repeat containing 5 (Armc5)	NM_001009455.1	NA
0.8%	1		asparaginase like 1 (Asrgl1)	NM_145089.2	Cytoplasm
0.8%	1	‡	ataxin 10 (Atxn10)	NM_133313.2	Cytoplasm
1.5%	2		ATP synthase, H+ transporting, mitochondrial F0	NM_053602.1	mitochondrial
0.8%	1		ATP synthase, H+ transporting, mitochondrial F1	NM_023093.1	mitochondrial
0.8%	1		bladder cancer associated protein homolog (Blcap)	BC087661.1	NA
0.8%	1		bromodomain adjacent to zinc finger domain protein 1B	NM_001191916.1	cytoplasm
0.8%	1	‡	calmodulin-dependent protein kinase IV (CaMKIV)	X91964.1	cytoplasm
0.8%	1		chaperonin subunit 3 (gamma) (Cct3)	NM_199091.1	cytoplasm
0.8%	1		chaperonin subunit 7 (eta) (Cct7)	NM_001106603.1	cytoplasm
0.8%	1		complexin 2 (Cplx2) (MUS)	NM_009946.2	cytoplasm
0.8%	1		coronin, actin-binding protein, 1B	BC061558.1	cytoplasm
0.8%	1		cytochrome b5 domain containing 2	NM_001007671.1	mitochondria
3.8%	5		cytochrome c-1	NM_001130491.1	mitochondria
0.8%	1		cytochrome c oxidase subunit IV	NM_017202.1	mitochondria
2.3%	3		cytochrome c oxidase subunit Va (Cox5a)	NM_145783.1	mitochondria
3.8%	5		cytochrome c oxidase subunit Vb	BC083179.1	mitochondria
2.3%	3	†	eukaryotic translation elongation factor 1 alpha 1 (EEF1A1)	BC128723.1	nuc./cytoplasm
0.8%	1		glyceraldehyde-3-phosphate dehydrogenase (Gapdh)	NM_017008.3	cytoplasm
4.6%	6	‡	guanylate kinase 1 (Guk1)	NM_001013115.1	cytoplasm
0.8%	1		heat shock protein 90 (Hsp90)	BC082009.1	cytoplasm
0.8%	1	‡	similar to HECT domain containing 1 (similar to Hectd1)	XM_343060.4	cytoplasm
1.5%	2		hemoglobin alpha, adult chain 1 (Hba-a1)	BC091567.1	cytoplasm
0.8%	1		HIG1 domain family, member 2A (Higd2a)	BC166544.1	membrane
0.8%	1		hydroxyacyl-Coenzyme A dehydrogenase, alpha subunit	NM_130826.2	mitochondria
0.8%	1		hydroxysteroid (17-beta) dehydrogenase 10	BC158587.1	mitochondria
1.5%	2		insulin-like growth factor binding protein 6	BC099742.1	NA
0.8%	1		laeverin (Lvrn)	XM_001054995.1	cell surface
0.8%	1		latrophilin 1 (MUS)	BC078414.1	trans mem.
0.8%	1		macrophage erythroblast attacher (Maea)	NM_001008319.1	membrane
0.8%	1		microtubule associated protein 1A (Mtap1a)	NM_030995.1	cytoplasm
2.3%	3	†	microtubule associated protein 1B	NM_019217.1	cytoplasm
0.8%	1		minichromosome maintenance deficient 7	NM_001004203.2	nuclear
0.8%	1		mitochondrial ribosomal protein L54 (Mrpl54)	NM_001106770.1	cytoplasm
0.8%	1		mitogen activated protein kinase kinase 2 (Map2k2)	BC126084.1	cytoplasm

0.8%	1		NADH dehydrogenase (ubiquinone) Fe-S protein 2	NM_001011907.1	membrane
0.8%	1		NADH dehydrogenase (ubiquinone) flavoprotein 1	NM_001006972.1	membrane
0.8%	1		neurofilament 3, medium polypeptide (Nefm)	NM_017029.1	NA
0.8%	1		neuronal beta-catenin like protein	AJ301634.1	NA
0.8%	1		nuclear factor I/X (CCAAT-binding transcription factor; Nfix)	NM_030866.1	nucleus
0.8%	1	‡	PEF protein with a long N-terminal hydrophobic domain	NM_001007651.1	nuc./cytoplasm
0.8%	1		peptidase D	NM_001009641.1	NA
0.8%	1		peripheral myelin protein 22 (Pmp22)	NM_017037.1	integral mem.
0.8%	1		phosphoribosyl transferase domain containing 1 (Prtfdc1)	NM_001106127.1	NA
1.5%	2		procollagen, type I, alpha 2 (Col1a2)	NM_053356.1	golgi./extracell.
3.8%	5	†	prosaposin (Psap)	BC061759.1	innt. mem./secr.
0.8%	1		quaking (Qk) (MUS)	NM_001115021	nuc./cytoplasm
0.8%	1		RAN binding protein 10	NM_001135875.1	cytoplasm
0.8%	1	†	Receptor for activated protein kinase C (RACK1)	BC063809.1	cytoplasm
0.8%	1		PRED: similar to 39S ribosomal protein L28	XM_001061401.1	cytoplasm
0.8%	1		ring finger protein 123 (Rnf123)	NM_032543.1	NA
4.6%	6		signal recognition particle,72 kDa (Srp)	NM_001170601.1	cytoplasm
0.8%	1		stathmin 1	BC062234.1	nuc./cytoplasm
11.5%	15	‡	stathmin-like 2 (Stmn2)	NM_053440.2	membrane-teth.
6.9%	9	‡	stathmin-like 3 (Stmn3)	NM_024346.1	membrane-teth.
0.8%	1		steroid receptor co-activator protein SRAP (Sra1)	NM_183329.3	nuclear
0.8%	1		SWI/SNF related, matrix assoco. (Smarcc1)	NM_001106861.1	nuclear
0.8%	1		thimet oligopeptidase 1 (Thop1)	BC081706.1	NA
0.8%	1		transcobalamin 2 (Tcn2)	NM_022534.1	NA
0.8%	1		PRED: similar to Ttc15 protein	XM_001071807.2	NA
0.8%	1		tubulin, beta 2b (Tubb2b)	NM_001013886.2	cytoplasm
0.8%	1		tumor protein p53	BC081788.1	nucl./cytoplasm

Table 1b

%	#		Protein Name	Acc#	Localization
0.9%	1		aldehyde dehydrogenase 2	BC062081.1	mitochondria
1.9%	2		aldolase A, (aldoa)	BC064440.1	cytoplasm
2.8%	3	†	ancient ubiquitous protein 1 (Aup1)	NM_001079899.1	cytoplasm
0.9%	1	‡	annexin A6	BC072523.1	cytosolic/mem.
3.8%	4		bladder cancer associated protein homolog (Blcap)	BC087661.1	NA
0.9%	1		calcium/calmodulin-dependent protein kinase IV (Camk4)	NM_012727.3	cytoplasm
0.9%	1		PRED: chromodomain helicase DNA binding protein 4 (Chd4	XM_001063352.1	nuclear
0.9%	1	†	copper metabolism (Murr1) domain containing 1	NM_001115022.1	nucl./cytoplasm
4.7%	5		cytochrome c-1 (Cyc1)	NM_001130491.1	mitochondria
0.9%	1		cytochrome c oxidase, subunit Va (Cox5a)	NM_145783.1	mitochondria
2.8%	3		eukaryotic translation elongation factor 1 alpha 1	BC128723.1	nucl./cytoplasm
0.9%	1		eukaryotic translation initiation factor 2B, subunit 4 delta (Eif2	NM_053950.1	cytoplasm
0.9%	1		eukaryotic translation initiation factor 1A dom. cont. (Eif1ad)	NM_001008305.1	cytoplasm
1.9%	2	‡	fasciculation and elongation protein zeta 1 (zygin I) (Fez1)	BC087740.1	nucl./cytoplasm
4.7%	5		glyceraldehyde-3-phosphate dehydrogenase (Gapdh)	NM_017008.3	cytoplasm
0.9%	1		glycosyltransferase (Large)	NM_001108439.1	golgi
0.9%	1		glyoxalase domain containing 4 (Glod4)	NM_001014227.1	mitochondria?
0.9%	1	‡	guanylate kinase 1 (Guk1)	NM_001013115.1	cytoplasm
0.9%	1		heat shock 90kDa protein 1, beta	BC082009.1	cytoplasm
0.9%	1		histidine triad nucleotide binding protein 2 (Hint2)	NM_001107955.2	mitochondria
0.9%	1		integrator complex subunit 10	NM_001134416.1	nuclear
0.9%	1		interferon stimulated exonuclease gene 20-like 2 (Isg20l2)	NM_001007741.1	nuclear
0.9%	1		laminin, beta 2 (Lamb2)	NM_012974.1	extracellular
1.9%	2		microtubule-associated protein 1b (Map1b)	NM_019217.1	cytoplasm
0.9%	1		minichromosome maintenance deficient 7	NM_001004203.2	nuclear
0.9%	1	‡	mitogen activated protein kinase kinase 2 (Map2k2)	NM_133283.1	cytoplasm
0.9%	1		NCK-associated protein 1 (Nckap1)	NM_031618.1	transmembrane
0.9%	1		PRED: similar to neuroblastoma-amplified	XR_006781.1	nuclear
0.9%	1		nuclear transcription factor-Y gamma (Nfyc) (MUS)	NM_008692.3	nuclear
0.9%	1		nucleic acid binding protein	NM_001047112.1	NA
0.9%	1		oxysterol binding protein-like 6 (Osbpl6)	NM_001107735.1	NA
0.9%	1		peripheral myelin protein 22 (Pmp22)	NM_017037.1	integral mem.
0.9%	1	†	phosphoinositide-specific phospholipase C form-I (PI-PLC I)	X12355.1	membrane
0.9%	1		procollagen, type III, alpha 1 (Col3a1)	NM_032085.1	golgi./extracell.
0.9%	1		prolyl endopeptidase-like (Prepl)	NM_001010951.1	cytoplasm
0.9%	1		proteasome 26S subunit, non-ATPase, 12 (Psmd12)	NM_001005875.1	nucl./cytoplasm
3.8%	4		RAN binding protein 10 (Ranbp10)	NM_001135875.1	cytoplasm
0.9%	1		required for meiotic nuclear division 5 homolog B	NM_001017473.1	nuclear
0.9%	1		PRED: 39S ribosomal protein L28 (L28mt)	XM_001061401.1	cytoplasm
0.9%	1		ribosomal protein L35 (Rpl35)	NM_212511.1	cytoplasm
0.9%	1		SEC31 homolog A (Sec31a)	NM_033021.1	NA
3.8%	4		signal recognition particle,72 kDa subunit, transcript var 1	NM_001170601.1	cytoplasm
16.0%	17	‡	stathmin-like 2 (Stmn2)	NM_053440.2	membrane-teth.

3.8%	4	‡	stathmin-like 3 (Stmn3)	NM_024346.1	membrane-teth.
0.9%	1		succinate dehydrogenase complex subunit B (Sdhb)	NM_001100539.1	mitochondria
1.9%	2		suppressor of var1, 3-like 1 (S. cerevisiae) (Supv3l1)	NM_001012462.1	mitochondria
0.9%	1		tetratricopeptide repeat domain 1 (Ttc1)	NM_001005529.1	NA
1.9%	2		tetratricopeptide repeat domain 39C (Ttc39c) (MUS)	NM_028341.4	NA
1.9%	2		transforming growth factor, beta induced (Tgfbi),	NM_053802.1	NA
0.9%	1		tubulin folding cofactor C (Tbcc)	NM_001108200.2	cytoplasm
9.4%	10	‡	ubiquitin-like modifier activating enzyme 1 (Uba1)	NM_001014080.1	nucl./cytoplasm

Tables 1a and 1b

Clones isolated from yeast two-hybrid screen of a rat dorsal root ganglia cDNA library using e37a-containing (Table 1a) and e37b-containing (Table 1b) $Ca_V2.2$ baits ($37a_S$ and $37b_S$) (see Fig. 2.2). Parallel yeast two-hybrid screens yielded 130 (37a bait) and 106 (37b bait) clones. Each identified clone is shown as a percentage of the total isolated from each screen followed by the number of individual clones. For each gene marked with "‡", at least one clone was co-transformed into yeast with the naked binding domain BD (pGBKT7) and failed to interact without the C-terminus of $Ca_V2.2$ present, whereas "†" indicates that clones interacted non-specifically with the GAL4 DNA binding domain and therefore have likely been isolated independently of interaction with $Ca_V2.2$. NCBI accession number and cellular localization are listed, if known.

A.2

I. $Ca_V2.2$ Western Blot Protocol (8.0)

Contact Spiro_Marangoudakis@brown.edu with any comments/questions

Prepare samples by homogenizing in 1X RIPA buffer.

- For whole adult mouse brain preps, homogenize one whole adult mouse brain in ~20 mL cold 1X RIPA buffer, and leave on ice for 30 minutes (If using Polytron™ homogenizer, set to speed setting "5", and homogenize until the brain is completely dissociated; any tube will work provided it is large enough). After the incubation, homogenize again to finish the homogenization process of any settled material. This preparation should produce samples of ~2 µg/µL protein, depending on the size of the mouse/brain.

- For DRG, ~100 DRG (from ~5 mice) should be homogenized in ~1mL cold 1X RIPA buffer. This process should be performed the same as the one for brain tissue.

- If dealing with cell lines, wash the cells 2X with 1X PBS @ room temp., remove the PBS, and add cold 1X RIPA buffer to cells on ice. Allow these to incubate for 30 minutes on ice, and whirl to detach/lyse (usually no scraping is required). Generally no more than 0.5 mL of RIPA will be required for a single (confluent) well of a 6-well plate (scale up/down if using larger/smaller wells/plates).

To remove debris from samples, spin down samples in a microcentrifuge for 20 minutes @ 13,500 RPM @ 4°C (cold room). Aliquot the supernatant into a new tube, and discard the original tube containing the pellet. since freeze/thaw cycles can damage the samples, freeze in small single-use aliquots (25-200 µL) at -80°C.

Perform BCA assay (Pierce Cat#23227) to determine sample concentration. I use samples at around 2 µg/µL.

Denature/reduce samples 1:1 in 2X reducing buffer. Optimize your denaturation/reduction protocol for each type of sample. When dealing with channels, optimization will be required because samples with higher concentrations of channels relative to total protein may require more time/ higher temperature vs. samples with lower concentrations of calcium channels overall. (This step can be performed before the gel is prepared provided that the samples are put in ice/water slush until ready to be run.)

- For brain and DRG lysates, room temperature denaturation for 15 minutes works well, whereas transfected cell lysates (which contain more $Ca_V2.2$ than other lysates) may require some heating, or dilution of the sample lower than 2µg/µL for a sharp signal on a western. Also, $Ca_V2.1$ may require slightly different conditions than $Ca_V2.2$ for optimal results.

Prepare gel based on size and migration kinetics for your protein of interest (Appendix section II)(for $Ca_V2.2$ a 6% resolving gel is recommended and outlined below):

6% Resolving Gel (If using .75mm plates, ~3mL is required per gel):

For 10mL buffer total:
5.35 mL Milli-Q H_2O
2.50 mL 1.5M tris HCl pH 8.8
2.00 mL 30% acrylamide/bis (BIORAD #161-0158)
100 µL 10% SDS solution (sterile filtered)
Add the following components only when gel is ready to be poured (mix well afterward):
70 µL 10% ammonium persulfate solution (APS; Sigma #A-3678)*
10 µL N,N,N',N'-tetramethylethylenediamine (TEMED; Sigma #T22500)

* If storing 10% APS solution, make sure it is frozen @ -20^{o}C. Any leftover can be stored for a couple weeks at 4^{o}C, or re-frozen at -20^{o}C. Several thaws are possible without losing effectiveness
** Save any tube/pipette that has come into contact with acrylamide in a waste container, and label as "acrylamide" for a specialist to remove. Acrylamide is a hazardous waste.

Pour resolving gel solution up to 1.5cm away from the top of the plates (If using BIO-RAD mini-PROTEAN 3 system). Cover with about 2 mL n-Butyl alcohol that has been saturated with H_2O (2 phase n-butyl alcohol/water suspension, use upper phase which is n-butyl alcohol. Lower phase is water).

After about 10-15 minutes of letting the plates sit at room temp you will know when the acrylamide has cured when three phases are visible (look closely), and/or when your remaining solution has hardened. At this point pour out the upper two phases (in a waste container, acrylamide is a hazardous waste), rinse with dH_2O, and remove as much water as possible before going on to the next step.

Next prepare the Stacking Gel (4%) (If using .75mm plates, ~2mL is required per gel):

For 5mL solution total:
3.0 mL Milli-Q H_2O
1.25 mL 1M tris HCl pH 6.8
665 µL 30% acrylamide/bis
50 µL 10% SDS solution
Add the following components only when gel is ready to be poured (mix well afterward):
40 µL 10% ammonium persulfate solution (APS)
5 µL TEMED
* Save any tube/pipette that has come into contact with acrylamide in a waste container, and label as "acrylamide" for a specialist to remove. Acrylamide is a hazardous waste.

Pour the stacking gel solution over the resolving gel and put in comb. Keep the remainder of the solution nearby and add 150 µL to each side of the top of the plates. As the gel cures, it will condense and pull in air from the top of the plates, which will affect your well shape/volume. To keep this from happening, make sure that the gel has adequate solution to draw down (from the top of the plates) and keep air from being drawn in instead as the gel hardens.

Allow this gel to harden for about 15-20 minutes. When the leftover solution in your preparation tube hardens as solid as it will get, you can then use the gel.

Prepare 1X electrophoresis run buffer from 10X Stock (no more than 350mL will be required in this system).

Remove combs from gels and rinse the wells by pouring 1X run buffer over wells until they have filled and then pour out the solution in the sink. Repeat this step one or two more times. This will ensure that un-solidified stacking gel solution is removed and will not later harden in the wells and affect the samples as they are later pipetted in.

Put plate(s) into apparatus, and make sure that a tight seal is formed between the plates and the apparatus (plates should fit together snugly to reduce buffer loss once filled). Fill chamber with run buffer, and pour the rest into the bottom of the apparatus. Buffer should cover the bottom of the plates.

Reduce/denature samples if not done previously. Add 2X RSB to sample and perform reduction/denaturation as best determined for your sample. For samples with low concentrations of channels (such as brain prep), 15 minutes at room temperature may be optimal. For more concentrated samples, 5 minutes at 95^{o}C may be best. This will have to be worked out by the experimenter. Some recommend testing temperatures between 50 and 65^{o}C, and incubation times between 10 and 15 minutes if the times/temps outlined above do not work well. Put samples on ice/water slush after denaturation until ready for use. Exact conditions may have to be determined for each preparation and/or each channel type (eg. Troubleshooting in Appendix section III)

Pipette samples into wells (for large wells ~20 µL can be loaded). A protein marker/ ladder should also be used to determine the size of samples tested. I prefer “Precision Plus Kaleidoscope Standard” by BIO-RAD (Cat#161-0375). 10uL per gel works well.

Run samples at 10 mA per plate (20 mA for two), for 1:30 (hr:min), and after that switch to 20 mA per plate (40 mA for two) for another 30 minutes (or until the desired amount of protein migration). I run these until the 75 kD marker is close to the bottom of the gel.

Prepare 1X transfer buffer from the 5X Stock. For calcium channels I prepare 1L of buffer by adding: 200 mL 5X stock, 650 mL Milli-Q H_2O, and 150 mL methanol. This buffer is specifically designed to allow smaller molecular weight proteins through the membrane, while retaining larger proteins such as $Ca_V2.2$. A buffer solution can be prepared with 200 mL 5X stock, 600 mL Milli-Q H_2O, and 200 mL methanol if smaller proteins are to be analyzed. Nitrocellulose transfer membranes of .45 um are required, many brands will work (I use Whatman Ptrotan #10401196).

Transfer is performed in a large plastic autoclave tub with ice water. A stir bar should be placed in the transfer box, and placed in the autoclave tub. Both should be placed above the stir/ hotplate. The stir-plate should be turned on until you hear the stir bar whirling, then the icepack that came with the kit should be put in (make sure to NOT activate the hotplate feature!). Align electrodes and run for 1hr at 100V.

Remove membranes, and put them in small plastic containers with 1X PBS-T. Protein side (side that was in contact with gel) should be facing UP! Mark the membranes with required info, and if using a

pre-stained marker, mark the position of the bands in the marker lane with a protein blot marker ("Clearly Better Blotting" marker).

Block the membrane(s). 25 mL of 5% carnation nonfat dry milk in 1X-PBS-T per membrane for one hour (@ room temp.) while rocking works well with Alomone primary antibodies and Jackson labs secondaries. If other antibodies are used this will have to be worked out. 3-5% BSA in PBS-T can also be used. Recommendations for blocking are usually found on instructions for primary and/or secondary antibodies. Overnight incubation at 4^{o}C (cold room), with rocking, could also be performed.

Rinse the membrane(s) with ~20 mL PBS-T (2X), and wash 3 times, 3 minutes each at room temp on a rocker.

Add primary antibody solution (1:100 recommended if using Alomone Rabbit anti-Ca_V2.2, #ACC-002). I prepare 15ml 1% BSA in PBS-T with 150 µL of stock antibody solution (.425 µg/µL, resuspended in 50% glycerol) and 15uL 10% NaN_3 (for long-term storage). Incubate 1hr at room temp, or overnight at 4^{o}C. Rocking is required. After incubation, pour antibody solution back into 15 mL conical tube and store at 4^{o}C. These antibodies can be used up to 25 times (25 individual membranes) with little reduction of effectiveness.

Rinse 2X and wash 3X with PBS-T as done previously.

Add secondary abs. Determine which concentration works best. For Jackson Labs Donkey anti-Rabbit antibody (#711-036-152), a 1:7,500 dilution (2 µL/ 15mL) in 1% BSA/1X PBS-T works well (best signal/background ratio). This step takes about one hour at room temperature, and rocking.

Rinse 2X and wash 3X with PBS-T on a rocker (at least 10 minutes are required for each wash step)

Develop as required. If using an HRP secondary, ECL works well (Amersham, #RPN2209). Mix components, and layer over membrane. Allow to soak ~1 minute, then blot quickly and place between two plastic transparency sheets and develop either on film (Amersham, #28906839) or using a typhoon/storm system. Exposure time will depend on your samples and antibodies, but generally several time points are taken, starting with 30 seconds or one minute to get an understanding of what your signal looks like. Also, the developer usually takes at least 15 minutes to warm up, so I suggest turning this on during your washing steps. Make sure to run a couple of previously exposed/developed pieces of film "cleaner film" through to clean the machine out before you develop your first film.

To re-probe a given membrane for a second product, the following protocol can be followed (probe for weakest signal first, as strength of signal can decrease after stripping):

1) Rinse the membrane in 1X PBS-T, and incubate with fresh PBS-T at RT (while rocking) for 5 min
2) Make fresh volume of stripping buffer (buffer listed under "Reagents" section below)
3) Pour out PBS-T, and incubate each membrane with 10 mL stripping buffer at ~50^{o}C while rocking @ ~70 RPM
4) Rinse membrane(s) and wash twice with large volumes of PBS-T (≥20 mL), 10 min each (while rocking)
5) Re-block membrane (according to antibody), and perform antibody probing as usual

Protocol Appendix

I. Reagents:

1X RIPA buffer** (Store at 4°C):

For 10mL buffer total:	Conc. of each component:
500 µL 1M Tris HCl pH 7.5	50 mM
300 µL 5M NaCl solution (Sigma #S-3014)	150 mM
1mL 10% Igepal CA-630 solution (sterile filtered, Sigma #I3021)	1%
500 µL 10% sodium deoxycholate solution (sterile filtered) (DOC; Sigma #D6750)	.5%
100 µL 10% sodium dodecyl sulfate solution (sterile filtered) (SDS; Sigma #L4509)*	.1%
Add Milli-Q H_20 to 10 mL (~7.6mL)	

* If storing RIPA buffer at 4°C, do not add SDS until ready to use, as it may affect buffer's stability

** Before use also dissolve 1 tablet of Roche Complete mini protease inhibitor tablet (Roche #04 693 159 001, or similar cocktail of inhibitors) per 10 mL of RIPA buffer

2x reducing sample buffer (2X RSB)

(5 mL preparation; freeze in 500uL aliquots @ -20°C afterward):

For 5 mL buffer total:	Conc. of each component:
.5 mL 1M Tris-HCl, pH 6.8	100 mM
.2g sodium dodecyl sulfate (SDS)	4% (w/v)
.01 g bromophenol blue	0.2%
1 mL 100% stock liquid glycerol (Sigma #G2025)	20% (v/v)
.154 g dithiothreitol (DTT; Sigma #D9163)	200 mM
Add Milli-Q H_2O up to 5mL (~3.5 mL)	

Electrophoresis run buffer stock (10X) (Store at R.T.):

For 500 mL buffer total:	Conc. of each component:
15.14g tris base (Fisher #BP152)	250 mM
93.84g glycine (Sigma #G8898)	2500 mM
5 g SDS (w/v)	1% (w/v)

Dissolve on hot/stir-plate (use slight heat and stirring as required) and make up to .5L with Milli-Q H_2O, sterile filter

Transfer buffer stock (5X) (Store at R.T.):

For 1L buffer total:	Conc. of each component:
15.14g Tris base	125 mM
71.32g Glycine	950 mM
5g SDS (w/v)	.5% (w/v)

Dissolve on hot/stir-plate (use slight heat and stirring as required) and make up to 1L with Milli-Q H_2O, sterile filter

1X PBS-T (Store at R.T.):

For 1 L buffer total:	Conc. of each component:
100 mL of 10X PBS (Gibco #70011)	1X
Add Milli-Q H_2O to 1L (895 mL)	
5 mL of 20% Tween-20 solution (Sigma #P5927)	0.1% Tween-20

Membrane stripping buffer **(make fresh at time of use)**

For 10 mL buffer- enough for one (~9cm x 7cm) membrane	**Conc.:**
2 mL of 10% SDS solution (in H_2O)	2 %
625 µL 1M Tris-HCl pH 6.8	62.5 mM
78.1 µL 2-mercaptoethanol 14.3 M	100 mM
7.30 mL H_2O (to 10 mL)	

II. Determination of gel percentage:

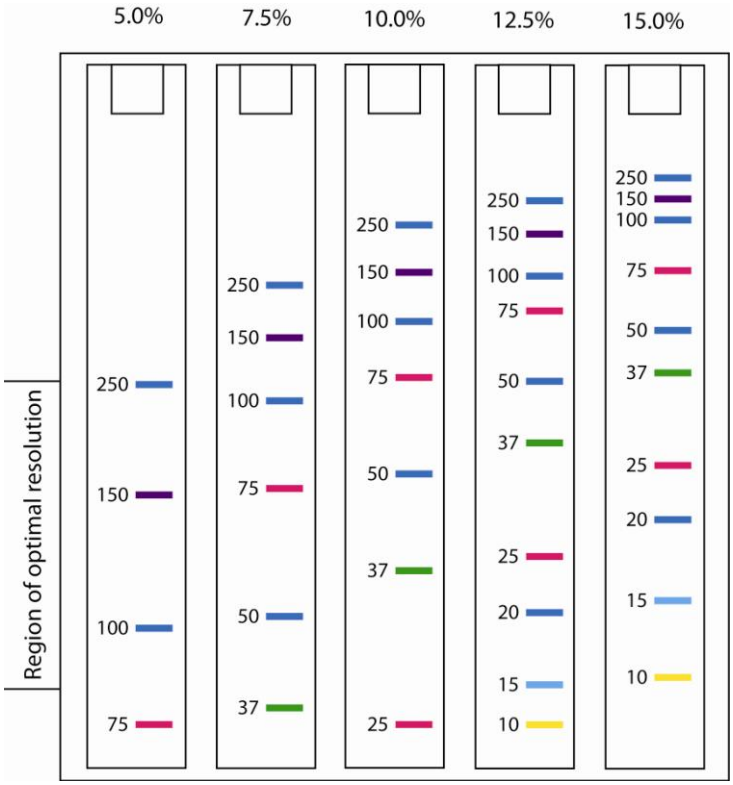

Approximate migration when I tested with BIO-RAD "Precision Plus Kaleidoscope Standard" (Cat# 161-0375) your results may vary slightly

Recipes for resolving gels (all volumes in mL):

Percentage:	4.5	5.0	6.0	7.0	7.5	8.0	9.0	10	11	11.5	15
H_2O	5.84	5.68	5.35	5.01	4.85	4.68	4.35	4.01	3.68	3.51	2.35
1.5M Tris-HCl (pH8.8)	2.50	2.50	2.50	2.50	2.50	2.50	2.50	2.50	2.50	2.50	2.50
30% Acrylamide/Bis	1.5	1.67	2.00	2.33	2.50	2.66	3.00	3.33	3.67	3.83	5
10% SDS	0.10	.100	.100	.100	.100	.100	.100	.100	.100	.100	.100
10% APS	0.07	0.07	0.07	0.07	0.07	0.07	0.07	0.07	0.07	0.07	0.07
TEMED	0.007	0.007	0.007	0.007	0.007	0.007	0.007	0.007	0.007	0.007	0.007
Total Volume:	10	10	10	10	10	10	10	10	10	10	10

III. Example of Troubleshooting Results:

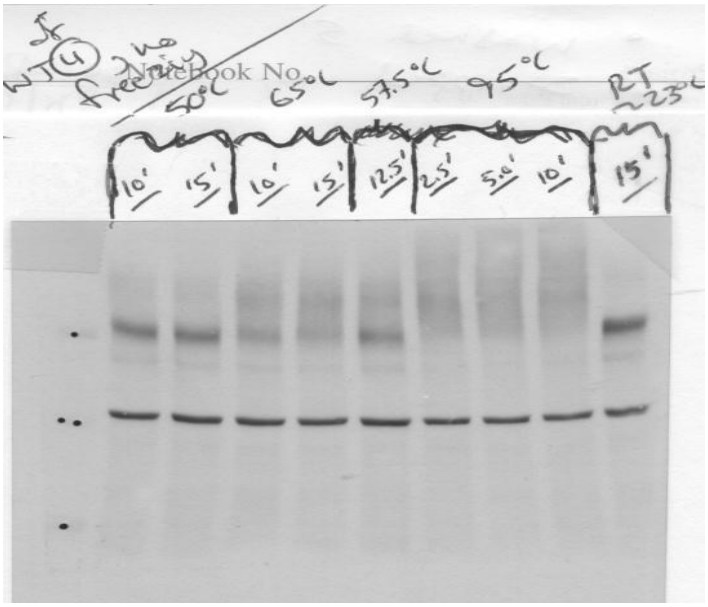

The above image is an example of an optimization of adult mouse brain lysates as explained in this protocol. This experiment showed that of the nine conditions tested for denaturation/reduction, room temp for 15 minutes worked best in terms of producing the sharpest band, and least amount of smearing at larger molecular weights (precipitated material that likely "frizzled" with heating). $Ca_V2.2$ was detected using Alomone primaries, Jackson Labs secondaries, and an ECL/film system. Your results may vary depending on the tissue used, and a similar test is advised when performing a western on $Ca_V2.2$ for the first time. Marker lane: the upper dot is 250 kD, the middle two dots are 150 kD, and the lower dot is 75 kD, marking your membrane this way before blocking can help keep track of molecular weight info as well as position.

REFERENCES

Adams PJ, Garcia E, David LS, Mulatz KJ, Spacey SD, Snutch TP (2009) Ca(V)2.1 P/Q-type calcium channel alternative splicing affects the functional impact of familial hemiplegic migraine mutations: implications for calcium channelopathies. Channels (Austin) 3:110-121.

Aggarwal SK, MacKinnon R (1996) Contribution of the S4 segment to gating charge in the Shaker K+ channel. Neuron 16:1169-1177.

Altier C, Zamponi GW (2004) Targeting Ca2+ channels to treat pain: T-type versus N-type. Trends Pharmacol Sci 25:465-470.

Altier C, Garcia-Caballero A, Simms B, You H, Chen L, Walcher J, Tedford HW, Hermosilla T, Zamponi GW (2010) The Cavbeta subunit prevents RFP2-mediated ubiquitination and proteasomal degradation of L-type channels. Nat Neurosci.

Altier C, Dale CS, Kisilevsky AE, Chapman K, Castiglioni AJ, Matthews EA, Evans RM, Dickenson AH, Lipscombe D, Vergnolle N, Zamponi GW (2007) Differential role of N-type calcium channel splice isoforms in pain. J Neurosci 27:6363-6373.

Altier C, Khosravani H, Evans RM, Hameed S, Peloquin JB, Vartian BA, Chen L, Beedle AM, Ferguson SS, Mezghrani A, Dubel SJ, Bourinet E, McRory JE, Zamponi GW (2006) ORL1 receptor-mediated internalization of N-type calcium channels. Nat Neurosci 9:31-40.

Amano K, Fujii M, Arata S, Tojima T, Ogawa M, Morita N, Shimohata A, Furuichi T, Itohara S, Kamiguchi H, Korenberg JR, Arata A, Yamakawa K (2009) DSCAM deficiency causes loss of pre-inspiratory neuron synchroneity and perinatal death. J Neurosci 29:2984-2996.

Amerik AY, Hochstrasser M (2004) Mechanism and function of deubiquitinating enzymes. Biochim Biophys Acta 1695:189-207.

Andrade A, Denome S, Jiang YQ, Marangoudakis S, Lipscombe D (2010) Opioid inhibition of N-type Ca2+ channels and spinal analgesia couple to alternative splicing. Nat Neurosci 13:1249-1256.

Arikkath J, Felix R, Ahern C, Chen CC, Mori Y, Song I, Shin HS, Coronado R, Campbell KP (2002) Molecular characterization of a two-domain form of the neuronal voltage-gated P/Q-type calcium channel alpha(1)2.1 subunit. FEBS Lett 532:300-308.

Bao J, Li JJ, Perl ER (1998) Differences in Ca2+ channels governing generation of miniature and evoked excitatory synaptic currents in spinal laminae I and II. J Neurosci 18:8740-8750.

Baranauskas G, Tkatch T, Nagata K, Yeh JZ, Surmeier DJ (2003) Kv3.4 subunits enhance the repolarizing efficiency of Kv3.1 channels in fast-spiking neurons. Nat Neurosci 6:258-266.

Barton NH (2007) Evolution. Cold Spring Harbor, N.Y.: Cold Spring Harbor Laboratory Press.

Bean BP (1989) Neurotransmitter inhibition of neuronal calcium currents by changes in channel voltage dependence. Nature 340:153-156.

Beedle AM, Hamid J, Zamponi GW (2002) Inhibition of transiently expressed low- and high-voltage-activated calcium channels by trivalent metal cations. J Membrane Biol 187:225-238.

Bell TJ, Thaler C, Castiglioni AJ, Helton TD, Lipscombe D (2004) Cell-specific alternative splicing increases calcium channel current density in the pain pathway. Neuron 41:127-138.

Bingol B, Schuman EM (2005) Synaptic protein degradation by the ubiquitin proteasome system. Curr Opin Neurobiol 15:536-541.

Bloom J, Pagano M (2005) Experimental tests to definitively determine ubiquitylation of a substrate. Methods Enzymol 399:249-266.

Bollmann JH, Sakmann B, Borst JG (2000) Calcium sensitivity of glutamate release in a calyx-type terminal. Science 289:953-957.

Bourinet E, Soong TW, Sutton K, Slaymaker S, Mathews E, Monteil A, Zamponi GW, Nargeot J, Snutch TP (1999) Splicing of alpha 1A subunit gene generates phenotypic variants of P- and Q-type calcium channels. Nat Neurosci 2:407-415
.
Boutz PL, Stoilov P, Li Q, Lin CH, Chawla G, Ostrow K, Shiue L, Ares M, Jr., Black DL (2007) A post-transcriptional regulatory switch in polypyrimidine tract-binding proteins reprograms alternative splicing in developing neurons. Genes Dev 21:1636-1652.

Bowersox SS, Gadbois T, Singh T, Pettus M, Wang YX, Luther RR (1996) Selective N-type neuronal voltage-sensitive calcium channel blocker, SNX-111, produces spinal antinociception in rat models of acute, persistent and neuropathic pain. J Pharmacol Exp Ther 279:1243-1249.

Brice NL, Berrow NS, Campbell V, Page KM, Brickley K, Tedder I, Dolphin AC (1997) Importance of the different beta subunits in the membrane expression of the alpha1A and alpha2 calcium channel subunits: studies using a depolarization-sensitive alpha1A antibody. Eur J Neurosci 9:749-759.

Brody DL, Yue DT (2000) Relief of G-protein inhibition of calcium channels and short-term synaptic facilitation in cultured hippocampal neurons. J Neurosci 20:889-898.

Brosenitsch TA, Katz DM (2001) Physiological patterns of electrical stimulation can induce neuronal gene expression by activating N-type calcium channels. J Neurosci 21:2571-2579.

Calarco JA, Superina S, O'Hanlon D, Gabut M, Raj B, Pan Q, Skalska U, Clarke L, Gelinas D, van der Kooy D, Zhen M, Ciruna B, Blencowe BJ (2009) Regulation of vertebrate nervous system alternative splicing and development by an SR-related protein. Cell 138:898-910.

Campbell V, Berrow NS, Fitzgerald EM, Brickley K, Dolphin AC (1995) Inhibition of the interaction of G protein G(o) with calcium channels by the calcium channel beta-subunit in rat neurones. J Physiol 485 (Pt 2):365-372.

Canti C, Page KM, Stephens GJ, Dolphin AC (1999) Identification of residues in the N terminus of alpha1B critical for inhibition of the voltage-dependent calcium channel by Gbeta gamma. J Neurosci 19:6855-6864.

Castiglioni AJ, Raingo J, Lipscombe D (2006) Alternative splicing in the C-terminus of CaV2.2 controls expression and gating of N-type calcium channels. J Physiol 576:119-134.

Catterall WA (1998) Structure and function of neuronal Ca2+ channels and their role in neurotransmitter release. Cell Calcium 24:307-323.

Catterall WA (2000) Structure and regulation of voltage-gated Ca2+ channels. Annu Rev Cell Dev Biol 16:521-555.

Catterall WA, Few AP (2008) Calcium channel regulation and presynaptic plasticity. Neuron 59:882-901.

Cellot G, Cilia E, Cipollone S, Rancic V, Sucapane A, Giordani S, Gambazzi L, Markram H, Grandolfo M, Scaini D, Gelain F, Casalis L, Prato M, Giugliano M, Ballerini L (2009) Carbon nanotubes might improve neuronal performance by favouring electrical shortcuts. Nat Nanotechnol 4:126-133.

Chang YF, Imam JS, Wilkinson MF (2007) The nonsense-mediated decay RNA surveillance pathway. Annu Rev Biochem 76:51-74.

Chen BS, Roche KW (2007) Regulation of NMDA receptors by phosphorylation. Neuropharmacology 53:362-368.

Chen M, Manley JL (2009) Mechanisms of alternative splicing regulation: insights from molecular and genomics approaches. Nat Rev Mol Cell Biol 10:741-754.

Chien AJ, Carr KM, Shirokov RE, Rios E, Hosey MM (1996) Identification of palmitoylation sites within the L-type calcium channel beta2a subunit and effects on channel function. J Biol Chem 271:26465-26468.

Ciechanover A (1998) The ubiquitin-proteasome pathway: on protein death and cell life. EMBO J 17:7151-7160.

Ciechanover A (2005) N-terminal ubiquitination. Methods Mol Biol 301:255-270.

Colledge M, Snyder EM, Crozier RA, Soderling JA, Jin Y, Langeberg LK, Lu H, Bear MF, Scott JD (2003) Ubiquitination regulates PSD-95 degradation and AMPA receptor surface expression. Neuron 40:595-607.

Costigan M, Scholz J, Woolf CJ (2009) Neuropathic pain: a maladaptive response of the nervous system to damage. Annu Rev Neurosci 32:1-32.

d'Azzo A, Bongiovanni A, Nastasi T (2005) E3 ubiquitin ligases as regulators of membrane protein trafficking and degradation. Traffic 6:429-441.

De Waard M, Pragnell M, Campbell KP (1994) Ca2+ channel regulation by a conserved beta subunit domain. Neuron 13:495-503.

De Waard M, Scott VE, Pragnell M, Campbell KP (1996) Identification of critical amino acids involved in alpha1-beta interaction in voltage-dependent Ca2+ channels. FEBS Lett 380:272-276.

De Waard M, Hering J, Weiss N, Feltz A (2005) How do G proteins directly control neuronal Ca2+ channel function? Trends Pharmacol Sci 26:427-436.

Deshaies RJ, Joazeiro CA (2009) RING domain E3 ubiquitin ligases. Annu Rev Biochem 78:399-434.

DiAntonio A, Hicke L (2004) Ubiquitin-dependent regulation of the synapse. Annu Rev Neurosci 27:223-246.

Diverse-Pierluissi M, Dunlap K (1993) Distinct, convergent second messenger pathways modulate neuronal calcium currents. Neuron 10:753-760.

Dolphin AC (2003a) Beta subunits of voltage-gated calcium channels. J Bioenerg Biomembr 35:599-620.

Dolphin AC (2003b) G protein modulation of voltage-gated calcium channels. Pharmacol Rev 55:607-627.

Dolphin AC (2009) Calcium channel diversity: multiple roles of calcium channel subunits. Curr Opin Neurobiol 19:237-244.

Dredge BK, Polydorides AD, Darnell RB (2001) The splice of life: alternative splicing and neurological disease. Nat Rev Neurosci 2:43-50.

Dubel SJ, Starr TV, Hell J, Ahlijanian MK, Enyeart JJ, Catterall WA, Snutch TP (1992) Molecular cloning of the alpha-1 subunit of an omega-conotoxin-sensitive calcium channel. Proc Natl Acad Sci U S A 89:5058-5062.

Dunlap K, Fischbach GD (1978) Neurotransmitters decrease the calcium ocmponent of sensory neurone action potentials. Nature 276:837-839.

Dunlap K, Luebke JI, Turner TJ (1995) Exocytotic Ca2+ Channels in Mammalian Central Neurons. Trends in Neurosciences 18:89-98.

Dunlop J, Bowlby M, Peri R, Vasilyev D, Arias R (2008) High-throughput electrophysiology: an emerging paradigm for ion-channel screening and physiology. Nature Reviews Drug Discovery 7:358-368.

Elmslie KS (2003) Neurotransmitter modulation of neuronal calcium channels. J Bioenerg Biomembr 35:477-489.

Ertel EA, Campbell KP, Harpold MM, Hofmann F, Mori Y, Perez-Reyes E, Schwartz A, Snutch TP, Tanabe T, Birnbaumer L, Tsien RW, Catterall WA (2000) Nomenclature of voltage-gated calcium channels. Neuron 25:533-535.

Fairbrother WG, Lipscombe D (2008) Repressing the neuron within. Bioessays 30:1-4.

Fang Z, Park CK, Li HY, Kim HY, Park SH, Jung SJ, Kim JS, Monteil A, Oh SB, Miller RJ (2007) Molecular basis of Ca(v)2.3 calcium channels in rat nociceptive neurons. J Biol Chem 282:4757-4764.

Fettiplace R, Fuchs PA (1999) Mechanisms of hair cell tuning. Annu Rev Physiol 61:809-834.

Frucht CS, Uduman M, Kleinstein SH, Santos-Sacchi J, Navaratnam DS (2011) Gene Expression Gradients along the Tonotopic Axis of the Chicken Auditory Epithelium. J Assoc Res Otolaryngol.

Fu AK, Hung KW, Fu WY, Shen C, Chen Y, Xia J, Lai KO, Ip NY (2011) APC(Cdh1) mediates EphA4-dependent downregulation of AMPA receptors in homeostatic plasticity. Nat Neurosci 14:181-189.

Garber K (2005) Peptide leads new class of chronic pain drugs. Nat Biotechnol 23:399.

Ghasemzadeh MB, Pierce RC, Kalivas PW (1999) The monoamine neurons of the rat brain preferentially express a splice variant of alpha1B subunit of the N-type calcium channel. J Neurochem 73:1718-1723.

Glaum SR, Miller RJ, Hammond DL (1994) Inhibitory actions of delta 1-, delta 2-, and mu-opioid receptor agonists on excitatory transmission in lamina II neurons of adult rat spinal cord. J Neurosci 14:4965-4971.

Glickman MH, Ciechanover A (2002) The ubiquitin-proteasome proteolytic pathway: destruction for the sake of construction. Physiol Rev 82:373-428.

Gray AC, Raingo J, Lipscombe D (2007) Neuronal calcium channels: splicing for optimal performance. Cell Calcium 42:409-417.

Guo L, Morris DG, Liu XY, Vaslet C, Hurt RH, Kane AB (2007) Iron bioavailability and redox activity in diverse carbon nanotube samples. Chem Mater 19:3472-3478.

Guo L, Bussche AV, Buechner M, Yan AH, Kane AB, Hurt RH (2008) Adsorption of essential micronutrients by carbon nanotubes and the implications for nanotoxicity testing. Small 4:721-727.

Hargreaves K, Dubner R, Brown F, Flores C, Joris J (1988) A new and sensitive method for measuring thermal nociception in cutaneous hyperalgesia. Pain 32:77-88.

Hatakeyama S, Wakamori M, Ino M, Miyamoto N, Takahashi E, Yoshinaga T, Sawada K, Imoto K, Tanaka I, Yoshizawa T, Nishizawa Y, Mori Y, Niidome T, Shoji S (2001) Differential nociceptive responses in mice lacking the alpha(1B) subunit of N-type Ca(2+) channels. Neuroreport 12:2423-2427.

Hattori D, Millard SS, Wojtowicz WM, Zipursky SL (2008) Dscam-mediated cell recognition regulates neural circuit formation. Annu Rev Cell Dev Biol 24:597-620.

Hershko A, Ciechanover A (1998) The ubiquitin system. Annu Rev Biochem 67:425-479.

Hibino H, Pironkova R, Onwumere O, Vologodskaia M, Hudspeth AJ, Lesage F (2002) RIM binding proteins (RBPs) couple Rab3-interacting molecules (RIMs) to voltage-gated Ca2+ channels. Neuron 34:411-423.

Hicke L (2001) Protein regulation by monoubiquitin. Nat Rev Mol Cell Biol 2:195-201.

Hille B (1994) Modulation of ion-channel function by G-protein-coupled receptors. Trends Neurosci 17:531-536.

Hille B (2001) Ion channels of excitable membranes, 3rd Edition. Sunderland, Mass.: Sinauer.

Hille B, Beech DJ, Bernheim L, Mathie A, Shapiro MS, Wollmuth LP (1995) Multiple G-protein-coupled pathways inhibit N-type Ca channels of neurons. Life Sci 56:989-992.

Hillman D, Chen S, Aung TT, Cherksey B, Sugimori M, Llinas RR (1991) Localization of P-type calcium channels in the central nervous system. Proc Natl Acad Sci U S A 88:7076-7080.

Hochberg LR, Serruya MD, Friehs GM, Mukand JA, Saleh M, Caplan AH, Branner A, Chen D, Penn RD, Donoghue JP (2006) Neuronal ensemble control of prosthetic devices by a human with tetraplegia. Nature 442:164-171.

Hochstrasser M (2007) Ubiquitin ligation without a ligase. Dev Cell 13:4-6.

Hochstrasser M (2009) Origin and function of ubiquitin-like proteins. Nature 458:422-429.

Hoeller D, Hecker CM, Wagner S, Rogov V, Dotsch V, Dikic I (2007) E3-independent monoubiquitination of ubiquitin-binding proteins. Mol Cell 26:891-898.

Holz GGt, Rane SG, Dunlap K (1986) GTP-binding proteins mediate transmitter inhibition of voltage-dependent calcium channels. Nature 319:670-672.

Horovitz CT, Birmingham SD (1999) Biochemistry of scandium and yttrium : Part 1: physical and chemical fundamentals. New York: Kluwer Academic/Plenum Publishers.

Hotton SK, Callis J (2008) Regulation of cullin RING ligases. Annu Rev Plant Biol 59:467-489.

Hu H, Ni YC, Montana V, Haddon RC, Parpura V (2004) Chemically functionalized carbon nanotubes as substrates for neuronal growth. Nano Lett 4:507-511.

Hunter T (2007) The age of crosstalk: phosphorylation, ubiquitination, and beyond. Mol Cell 28:730-738.

Hylden JL, Wilcox GL (1980) Intrathecal morphine in mice: a new technique. Eur J Pharmacol 67:313-316.

Ikeda SR (1991) Double-pulse calcium channel current facilitation in adult rat sympathetic neurones. J Physiol 439:181-214.

Ikeda SR, Dunlap K (1999) Voltage-dependent modulation of N-type calcium channels: role of G protein subunits. Adv Second Messenger Phosphoprotein Res 33:131-151.

Ikeda SR, Dunlap K (2007) Calcium channels diversify their signaling portfolio. Nat Neurosci 10:269-271.

Jensen KB, Dredge BK, Stefani G, Zhong R, Buckanovich RJ, Okano HJ, Yang YY, Darnell RB (2000) Nova-1 regulates neuron-specific alternative splicing and is essential for neuronal viability. Neuron 25:359-371.

Jones EM, Gray-Keller M, Fettiplace R (1999) The role of Ca2+-activated K+ channel spliced variants in the tonotopic organization of the turtle cochlea. J Physiol 518 (Pt 3):653-665.

Jones RB, Wang F, Luo Y, Yu C, Jin C, Suzuki T, Kan M, McKeehan WL (2001) The nonsense-mediated decay pathway and mutually exclusive expression of alternatively spliced FGFR2IIIb and -IIIc mRNAs. J Biol Chem 276:4158-4167.

Kagan VE, Tyurina YY, Tyurin VA, Konduru NV, Potapovich AI, Osipov AN, Kisin ER, Schwegler-Berry D, Mercer R, Castranova V, Shvedova AA (2006) Direct and indirect effects of single walled carbon nanotubes on RAW 264.7 macrophages: Role of iron. Toxicology Letters 165:88-100.

Kammermeier PJ, Ruiz-Velasco V, Ikeda SR (2000) A voltage-independent calcium current inhibitory pathway activated by muscarinic agonists in rat sympathetic neurons requires both Galpha q/11 and Gbeta gamma. J Neurosci 20:5623-5629.

Kaneko S, Cooper CB, Nishioka N, Yamasaki H, Suzuki A, Jarvis SE, Akaike A, Satoh M, Zamponi GW (2002) Identification and characterization of novel human Ca(v)2.2 (alpha(1B)) calcium channel variants lacking the synaptic protein interaction site. Journal of Neuroscience 22:82-92.

Kawaguchi M, Minami K, Nagashima K, Seino S (2006) Essential role of ubiquitin-proteasome system in normal regulation of insulin secretion. J Biol Chem 281:13015-13020.

Keefer EW, Botterman BR, Romero MI, Rossi AF, Gross GW (2008) Carbon nanotube coating improves neuronal recordings. Nat Nanotechnol 3:434-439.

Khanna R, Zougman A, Stanley EF (2007) A proteomic screen for presynaptic terminal N-type calcium channel (CaV2.2) binding partners. J Biochem Mol Biol 40:302-314.

Kim C, Jun K, Lee T, Kim SS, McEnery MW, Chin H, Kim HL, Park JM, Kim DK, Jung SJ, Kim J, Shin HS (2001) Altered nociceptive response in mice deficient in the alpha(1B) subunit of the voltage-dependent calcium channel. Mol Cell Neurosci 18:235-245.

Kirisako T, Kamei K, Murata S, Kato M, Fukumoto H, Kanie M, Sano S, Tokunaga F, Tanaka K, Iwai K (2006) A ubiquitin ligase complex assembles linear polyubiquitin chains. EMBO J 25:4877-4887.

Kisilevsky AE, Zamponi GW (2008) D2 dopamine receptors interact directly with N-type calcium channels and regulate channel surface expression levels. Channels (Austin) 2:269-277.

Kisilevsky AE, Mulligan SJ, Altier C, Iftinca MC, Varela D, Tai C, Chen L, Hameed S, Hamid J, Macvicar BA, Zamponi GW (2008) D1 receptors physically interact with N-type calcium channels to regulate channel distribution and dendritic calcium entry. Neuron 58:557-570.

Kondrashov FA, Koonin EV (2003) Evolution of alternative splicing: deletions, insertions and origin of functional parts of proteins from intron sequences. Trends Genet 19:115-119.

Lai MZ, Wang FS, Rohan JG, Maeno-Hikichi Y, Chen Y, Zhou Y, Gao GP, Sather WA, Zhang JF (2005) A tctex1-Ca2+ channel complex for selective surface expression of Ca2+ channels in neurons. Nature Neuroscience 8:435-442.

Lansman JB, Hess P, Tsien RW (1986) Blockade of current through single calcium channels by Cd2+, Mg2+, and Ca2+. Voltage and concentration dependence of calcium entry into the pore. J Gen Physiol 88:321-347.

Lee C, Kim N, Roy M, Graveley BR (2010) Massive expansions of Dscam splicing diversity via staggered homologous recombination during arthropod evolution. RNA 16:91-105.

Li DJ, Wang FS, Lai MZ, Chen Y, Zhang JF (2005) A protein phosphatase 2c alpha-Ca2+ channel complex for dephosphorylation of neuronal Ca2+ channels phosphorylated by protein kinase C. Journal of Neuroscience 25:1914-1923.

Li L, Chin LS (2003) The molecular machinery of synaptic vesicle exocytosis. Cellular and Molecular Life Sciences 60:942-960.

Li Q, Lee JA, Black DL (2007) Neuronal regulation of alternative pre-mRNA splicing. Nat Rev Neurosci 8:819-831.

Li Y, Wu YY, Zhou Y (2006) Modulation of inactivation properties of Ca(v)2.2 channels by 14-3-3 proteins. Neuron 51:755-771.

Liao P, Zhang HY, Soong TW (2009) Alternative splicing of voltage-gated calcium channels: from molecular biology to disease. Pflugers Arch 458:481-487.

Licatalosi DD, Mele A, Fak JJ, Ule J, Kayikci M, Chi SW, Clark TA, Schweitzer AC, Blume JE, Wang X, Darnell JC, Darnell RB (2008) HITS-CLIP yields genome-wide insights into brain alternative RNA processing. Nature 456:464-469.

Lim KL, Lim GG (2010) K63-linked ubiquitination and neurodegeneration. Neurobiol Dis.

Lin L, Shen S, Jiang P, Sato S, Davidson BL, Xing Y (2010) Evolution of alternative splicing in primate brain transcriptomes. Hum Mol Genet 19:2958-2973.

Lin Y, McDonough SI, Lipscombe D (2004) Alternative splicing in the voltage-sensing region of N-Type CaV2.2 channels modulates channel kinetics. J Neurophysiol 92:2820-2830.

Lin Z, Haus S, Edgerton J, Lipscombe D (1997) Identification of functionally distinct isoforms of the N-type Ca2+ channel in rat sympathetic ganglia and brain. Neuron 18:153-166.

Lin Z, Lin Y, Schorge S, Pan JQ, Beierlein M, Lipscombe D (1999) Alternative splicing of a short cassette exon in alpha1B generates functionally distinct N-type calcium channels in central and peripheral neurons. J Neurosci 19:5322-5331.

Lipscombe D (2005) Neuronal proteins custom designed by alternative splicing. Curr Opin Neurobiol 15:358-363.

Lipscombe D, Castiglioni AJ (2004) Alternative Splicing in Voltage Gated Calcium Channels: KluwerAcademic/Plenum Publishers.

Lipscombe D, Kongsamut S, Tsien RW (1989) Alpha-adrenergic inhibition of sympathetic neurotransmitter release mediated by modulation of N-type calcium-channel gating. Nature 340:639-642.

Lipscombe D, Pan JQ, Gray AC (2002) Functional diversity in neuronal voltage-gated calcium channels by alternative splicing of Cav alpha(1). Mol Neurobiol 26:21-44.

Lipscombe D, Allen SE, Gray AC, Marangoudakis S, Raingo J (2009) Alternative Splicing of Neuronal Cav2 Calcium Channels. In: Structure, Function and

Modulation of Neuronal Voltage-Gated Ion Channels (Kaczmarek VKGaLK, ed), p 483. Hoboken, New Jersey: John Wiley & Sons, Inc.

Liu X, Guo L, Morris D, Kane AB, Hurt RH (2008) Targeted removal of bioavailable metal as a detoxification strategy for carbon nanotubes. Carbon 46:489-500.

Liu XY, Gurel V, Morris D, Murray DW, Zhitkovich A, Kane AB, Hurt RH (2007) Bioavailability of nickel in single-wall carbon nanotubes. Adv Mater 19:2790-+.

Llinas R, Sugimori M, Lin JW, Cherksey B (1989) Blocking and Isolation of a Calcium-Channel from Neurons in Mammals and Cephalopods Utilizing a Toxin Fraction (Ftx) from Funnel-Web Spider Poison. P Natl Acad Sci USA 86:1689-1693.

Lorenzon NM, Lutz CM, Frankel WN, Beam KG (1998) Altered calcium channel currents in Purkinje cells of the neurological mutant mouse leaner. J Neurosci 18:4482-4489.

Lovat V, Pantarotto D, Lagostena L, Cacciari B, Grandolfo M, Righi M, Spalluto G, Prato M, Ballerini L (2005) Carbon nanotube substrates boost neuronal electrical signaling. Nano Lett 5:1107-1110.

Luebke JI, Dunlap K (1994) Sensory neuron N-type calcium currents are inhibited by both voltage-dependent and -independent mechanisms. Pflugers Arch 428:499-507.

Maeno-Hikichi Y, Chang SH, Matsumura K, Lai MZ, Lin H, Nakagawa N, Kuroda S, Zhang JF (2003) A PKC epsilon-ENH-channel complex specifically modulates N-type Ca2+ channels. Nature Neuroscience 6:468-475.

Makeyev EV, Zhang J, Carrasco MA, Maniatis T (2007) The MicroRNA miR-124 promotes neuronal differentiation by triggering brain-specific alternative pre-mRNA splicing. Mol Cell 27:435-448.

Malarkey EB, Reyes RC, Zhao B, Haddon RC, Parpura V (2008) Water Soluble Single-Walled Carbon Nanotubes Inhibit Stimulated Endocytosis in Neurons. Nano Lett 8:3538-3542.

Malmberg AB, Yaksh TL (1995) Effect of continuous intrathecal infusion of omega-conopeptides, N-type calcium-channel blockers, on behavior and antinociception in the formalin and hot-plate tests in rats. Pain 60:83-90.

Marker CL, Lujan R, Loh HH, Wickman K (2005) Spinal G-protein-gated potassium channels contribute in a dose-dependent manner to the analgesic effect of mu- and delta- but not kappa-opioids. J Neurosci 25:3551-3559.

Martin SW, Butcher AJ, Berrow NS, Richards MW, Paddon RE, Turner DJ, Dolphin AC, Sihra TS, Fitzgerald EM (2006) Phosphorylation sites on calcium channel alpha1 and beta subunits regulate ERK-dependent modulation of neuronal N-type calcium channels. Cell Calcium 39:275-292.

Matthews EA, Dickenson AH (2001) Effects of spinally delivered N- and P-type voltage-dependent calcium channel antagonists on dorsal horn neuronal responses in a rat model of neuropathy. Pain 92:235-246.

Mattson MP, Haddon RC, Rao AM (2000) Molecular functionalization of carbon nanotubes and use as substrates for neuronal growth. Journal of Molecular Neuroscience 14:175-182.

Maximov A, Bezprozvanny I (2002) Synaptic targeting of N-type calcium channels in hippocampal neurons. Journal of Neuroscience 22:6939-6952.

Maximov A, Sudhof TC, Bezprozvanny I (1999) Association of neuronal calcium channels with modular adaptor proteins. Journal of Biological Chemistry 274:24453-24456.

Mazzatenta A, Giugliano M, Campidelli S, Gambazzi L, Businaro L, Markram H, Prato M, Ballerini L (2007) Interfacing neurons with carbon nanotubes: Electrical signal transfer and synaptic stimulation in cultured brain circuits. Journal of Neuroscience 27:6931-6936.

McCleskey EW, Fox AP, Feldman DH, Cruz LJ, Olivera BM, Tsien RW, Yoshikami D (1987) Omega-conotoxin: direct and persistent blockade of specific types of calcium channels in neurons but not muscle. Proc Natl Acad Sci U S A 84:4327-4331.

Mich PM, Horne WA (2008) Alternative splicing of the Ca2+ channel beta4 subunit confers specificity for gabapentin inhibition of Cav2.1 trafficking. Mol Pharmacol 74:904-912.

Miller LC, Swayne LA, Kay JG, Feng ZP, Jarvis SE, Zamponi GW, Braun JEA (2003) Molecular determinants of cysteine string protein modulation of N-type calcium channels. Journal of Cell Science 116:2967-2974.

Mintz IM, Venema VJ, Swiderek KM, Lee TD, Bean BP, Adams ME (1992) P-type calcium channels blocked by the spider toxin omega-Aga-IVA. Nature 355:827-829.

Mlinar B, Enyeart JJ (1993) Block of Current through T-Type Calcium Channels by Trivalent Metal-Cations and Nickel in Neural Rat and Human-Cells. J Physiol-London 469:639-652.

Modrek B, Lee C (2002) A genomic view of alternative splicing. Nat Genet 30:13-19.

Mu Y, Otsuka T, Horton AC, Scott DB, Ehlers MD (2003) Activity-dependent mRNA splicing controls ER export and synaptic delivery of NMDA receptors. Neuron 40:581-594.

Muller CS, Haupt A, Bildl W, Schindler J, Knaus HG, Meissner M, Rammner B, Striessnig J, Flockerzi V, Fakler B, Schulte U (2010) Quantitative proteomics of the Cav2 channel nano-environments in the mammalian brain. Proc Natl Acad Sci U S A 107:14950-14957.

Nachshen DA (1984) Selectivity of the Ca Binding-Site in Synaptosome Ca Channels - Inhibition of Ca Influx by Multivalent Metal-Cations. Journal of General Physiology 83:941-967.

Nalepa G, Rolfe M, Harper JW (2006) Drug discovery in the ubiquitin-proteasome system. Nat Rev Drug Discov 5:596-613.

Nelson MT, Joksovic PM, Perez-Reyes E, Todorovic SM (2005) The endogenous redox agent L-cysteine induces T-type Ca2+ channel-dependent sensitization of a novel subpopulation of rat peripheral nociceptors. J Neurosci 25:8766-8775.

Ni YC, Hu H, Malarkey EB, Zhao B, Montana V, Haddon RC, Parpura V (2005) Chemically functionalized water soluble single-walled carbon nanotubes modulate neurite outgrowth. J Nanosci Nanotechno 5:1707-1712.

Nowycky MC, Fox AP, Tsien RW (1985) Three types of neuronal calcium channel with different calcium agonist sensitivity. Nature 316:440-443.

Oberdorster G, Oberdorster E, Oberdorster J (2005) Nanotoxicology: An emerging discipline evolving from studies of ultrafine particles. Environ Health Persp 113:823-839.

Olcese R, Neely A, Qin N, Wei X, Birnbaumer L, Stefani E (1996) Coupling between charge movement and pore opening in vertebrate neuronal alpha 1E calcium channels. J Physiol 497 (Pt 3):675-686.

Page KM, Heblich F, Davies A, Butcher AJ, Leroy J, Bertaso F, Pratt WS, Dolphin AC (2004) Dominant-negative calcium channel suppression by truncated constructs involves a kinase implicated in the unfolded protein response. J Neurosci 24:5400-5409.

Pan JQ, Lipscombe D (2000) Alternative splicing in the cytoplasmic II-III loop of the N-type Ca channel alpha 1B subunit: functional differences are beta subunit-specific. J Neurosci 20:4769-4775.

Pan Q, Shai O, Lee LJ, Frey BJ, Blencowe BJ (2008) Deep surveying of alternative splicing complexity in the human transcriptome by high-throughput sequencing. Nat Genet 40:1413-1415.

Park KH, Chhowalla M, Iqbal Z, Sesti F (2003) Single-walled carbon nanotubes are a new class of ion channel blockers. Journal of Biological Chemistry 278:50212-50216.

Patrick GN, Bingol B, Weld HA, Schuman EM (2003) Ubiquitin-mediated proteasome activity is required for agonist-induced endocytosis of GluRs. Curr Biol 13:2073-2081.

Paulo J, Brucker W, Hawrot E (2009) Proteomic Analysis of an 7 Nicotinic Acetylcholine Receptor Interactome. J Proteome Res.

Pelzer C, Kassner I, Matentzoglu K, Singh RK, Wollscheid HP, Scheffner M, Schmidtke G, Groettrup M (2007) UBE1L2, a novel E1 enzyme specific for ubiquitin. J Biol Chem 282:23010-23014.

Peng JM, Schwartz D, Elias JE, Thoreen CC, Cheng DM, Marsischky G, Roelofs J, Finley D, Gygi SP (2003) A proteomics approach to understanding protein ubiquitination. Nature Biotechnology 21:921-926.

Pickart CM (2001) Mechanisms underlying ubiquitination. Annu Rev Biochem 70:503-533.

Plata DL, Gschwend PM, Reddy CM (2008) Industrially synthesized single-walled carbon nanotubes: compositional data for users, environmental risk assessments, and source apportionment. Nanotechnology 19:-.

Polo-Parada L, Pilar G (1999) kappa- and mu-opioids reverse the somatostatin inhibition of Ca2+ currents in ciliary and dorsal root ganglion neurons. J Neurosci 19:5213-5227.

Pragnell M, Dewaard M, Mori Y, Tanabe T, Snutch TP, Campbell KP (1994) Calcium-Channel Beta-Subunit Binds to a Conserved Motif in the I-Ii Cytoplasmic Linker of the Alpha(1)-Subunit. Nature 368:67-70.

Puckerin A, Liu LY, Permaul N, Carman P, Lee J, Diverse-Pierluissi MA (2006) Arrestin is required for agonist-induced trafficking of voltage-dependent calcium channels. Journal of Biological Chemistry 281:31131-31141.

Pulskamp K, Diabate S, Krug HF (2007) Carbon nanotubes show no sign of acute toxicity but induce intracellular reactive oxygen species in dependence on contaminants. Toxicology Letters 168:58-74.

Raghib A, Bertaso F, Davies A, Page KM, Meir A, Bogdanov Y, Dolphin AC (2001) Dominant-negative synthesis suppression of voltage-gated calcium channel Cav2.2 induced by truncated constructs. J Neurosci 21:8495-8504.

Raingo J, Castiglioni AJ, Lipscombe D (2007) Alternative splicing controls G protein-dependent inhibition of N-type calcium channels in nociceptors. Nat Neurosci 10:285-292.

Randall A, Tsien RW (1995) Pharmacological Dissection of Multiple Types of Ca2+ Channel Currents in Rat Cerebellar Granule Neurons. Journal of Neuroscience 15:2995-3012.

Richards KS, Swensen AM, Lipscombe D, Bommert K (2007) Novel CaV2.1 clone replicates many properties of Purkinje cell CaV2.1 current. Eur J Neurosci 26:2950-2961.

Richman RW, Strock J, Hains MD, Cabanilla NJ, Lau KK, Siderovski DP, Diverse-Pierluissi M (2005) RGS12 interacts with the SNARE-binding region of the Ca(v)2.2 calcium channel. Journal of Biological Chemistry 280:1521-1528.

Rinetti GV, Schweizer FE (2010) Ubiquitination acutely regulates presynaptic neurotransmitter release in mammalian neurons. J Neurosci 30:3157-3166.

Rizzoli SO, Betz WJ (2005) Synaptic vesicle pools. Nature Reviews Neuroscience 6:57-69.

Rotin D, Kumar S (2009) Physiological functions of the HECT family of ubiquitin ligases. Nat Rev Mol Cell Biol 10:398-409.

Rotin D, Staub O (2010) Role of the ubiquitin system in regulating ion transport. Pflugers Arch.

Rzymski T, Grzmil P, Meinhardt A, Wolf S, Burfeind P (2008) PHF5A represents a bridge protein between splicing proteins and ATP-dependent helicases and is differentially expressed during mouse spermatogenesis. Cytogenet Genome Res 121:232-244.

Saegusa H, Matsuda Y, Tanabe T (2002) Effects of ablation of N- and R-type Ca(2+) channels on pain transmission. Neurosci Res 43:1-7.

Sather WA, McCleskey EW (2003) Permeation and selectivity in calcium channels. Annu Rev Physiol 65:133-159.

Sather WA, Tanabe T, Zhang JF, Mori Y, Adams ME, Tsien RW (1993) Distinctive biophysical and pharmacological properties of class A (BI) calcium channel alpha 1 subunits. Neuron 11:291-303.

Scherrer G, Imamachi N, Cao YQ, Contet C, Mennicken F, O'Donnell D, Kieffer BL, Basbaum AI (2009) Dissociation of the opioid receptor mechanisms that control mechanical and heat pain. Cell 137:1148-1159.

Schiff ML, Siderovski DP, Jordan JD, Brothers G, Snow B, De Vries L, Ortiz DF, Diverse-Pierluissi M (2000) Tyrosine-kinase-dependent recruitment of RGS12 to the N-type calcium channel. Nature 408:723-727.

Schneggenburger R, Neher E (2000) Intracellular calcium dependence of transmitter release rates at a fast central synapse. Nature 406:889-893.

Schneggenburger R, Neher E (2005) Presynaptic calcium and control of vesicle fusion. Curr Opin Neurobiol 15:266-274.

Schorge S, Gupta S, Lin Z, McEnery MW, Lipscombe D (1999) Calcium channel activation stabilizes a neuronal calcium channel mRNA. Nat Neurosci 2:785-790.

Schrlau MG, Falls EM, Ziober BL, Bau HH (2008) Carbon nanopipettes for cell probes and intracellular injection. Nanotechnology 19:-.

Schulman BA, Harper JW (2009) Ubiquitin-like protein activation by E1 enzymes: the apex for downstream signalling pathways. Nat Rev Mol Cell Biol 10:319-331.

Scott DA, Wright CE, Angus JA (2002) Actions of intrathecal omega-conotoxins CVID, GVIA, MVIIA, and morphine in acute and neuropathic pain in the rat. Eur J Pharmacol 451:279-286.

Scott VE, Felix R, Arikkath J, Campbell KP (1998) Evidence for a 95 kDa short form of the alpha1A subunit associated with the omega-conotoxin MVIIC receptor of the P/Q-type Ca2+ channels. J Neurosci 18:641-647.

Seidlits SK, Lee JY, Schmidt CE (2008) Nanostructured scaffolds for neural applications. Nanomedicine (Lond) 3:183-199.

Shapiro MS, Hille B (1993) Substance P and somatostatin inhibit calcium channels in rat sympathetic neurons via different G protein pathways. Neuron 10:11-20.

Sharp PM, Li WH (1987) Molecular evolution of ubiquitin genes. Trends Ecol Evol 2:328-332.

Shaw G, Morse S, Ararat M, Graham FL (2002) Preferential transformation of human neuronal cells by human adenoviruses and the origin of HEK 293 cells. FASEB J 16:869-871.

Shen L, Xiao Z, Pan Y, Fang M, Li C, Chen D, Wang L, Xi Z, Xiao F, Wang X (2011) Altered expression of Dscam in temporal lobe tissue from human and experimental animals. Synapse.

Sheng J, Kumagai A, Dunphy WG, Varshavsky A (2002) Dissection of c-MOS degron. EMBO J 21:6061-6071.

Sheng ZH, Yokoyama CT, Catterall WA (1997) Interaction of the synprint site of N-type Ca2+ channels with the C2B domain of synaptotagmin I. P Natl Acad Sci USA 94:5405-5410.

Sheng ZH, Rettig J, Takahashi M, Catterall WA (1994) Identification of a syntaxin-binding site on N-type calcium channels. Neuron 13:1303-1313.

Shenoy SK, McDonald PH, Kohout TA, Lefkowitz RJ (2001) Regulation of receptor fate by ubiquitination of activated beta 2-adrenergic receptor and beta-arrestin. Science 294:1307-1313.

Shukla AK, Kim J, Ahn S, Xiao K, Shenoy SK, Liedtke W, Lefkowitz RJ (2010) Arresting a transient receptor potential (TRP) channel: beta-arrestin 1 mediates ubiquitination and functional down-regulation of TRPV4. J Biol Chem 285:30115-30125.

Simen AA, Lee CC, Simen BB, Bindokas VP, Miller RJ (2001) The C terminus of the Ca channel alpha(1B) subunit mediates selective inhibition by G-protein-coupled receptors. Journal of Neuroscience 21:7587-7597.

Singer D, Biel M, Lotan I, Flockerzi V, Hofmann F, Dascal N (1991) The roles of the subunits in the function of the calcium channel. Science 253:1553-1557.

Soong TW, DeMaria CD, Alvania RS, Zweifel LS, Liang MC, Mittman S, Agnew WS, Yue DT (2002) Systematic identification of splice variants in human P/Q-type channel alpha1(2.1) subunits: implications for current density and Ca2+-dependent inactivation. J Neurosci 22:10142-10152.

Speese SD, Trotta N, Rodesch CK, Aravamudan B, Broadie K (2003) The ubiquitin proteasome system acutely regulates presynaptic protein turnover and synaptic efficacy. Curr Biol 13:899-910.

Spellman R, Llorian M, Smith CW (2007) Crossregulation and functional redundancy between the splicing regulator PTB and its paralogs nPTB and ROD1. Mol Cell 27:420-434.

Staats PS, Yearwood T, Charapata SG, Presley RW, Wallace MS, Byas-Smith M, Fisher R, Bryce DA, Mangieri EA, Luther RR, Mayo M, McGuire D, Ellis D (2004)

Intrathecal ziconotide in the treatment of refractory pain in patients with cancer or AIDS: a randomized controlled trial. JAMA 291:63-70.

Stanley EF, Atrakchi AH (1990) Calcium currents recorded from a vertebrate presynaptic nerve terminal are resistant to the dihydropyridine nifedipine. Proc Natl Acad Sci U S A 87:9683-9687.

Stea A, Tomlinson WJ, Soong TW, Bourinet E, Dubel SJ, Vincent SR, Snutch TP (1994) Localization and functional properties of a rat brain alpha 1A calcium channel reflect similarities to neuronal Q- and P-type channels. Proc Natl Acad Sci U S A 91:10576-10580.

Surmeier DJ, Bargas J, Hemmings HC, Jr., Nairn AC, Greengard P (1995) Modulation of calcium currents by a D1 dopaminergic protein kinase/phosphatase cascade in rat neostriatal neurons. Neuron 14:385-397.

Swayne LA, Chen L, Hameed S, Barr W, Charlesworth E, Colicos MA, Zamponi GW, Braun JEA (2005) Crosstalk between huntingtin and syntaxin 1A regulates N-type calcium channels. Molecular and Cellular Neuroscience 30:339-351.

Taddese A, Nah SY, McCleskey EW (1995) Selective opioid inhibition of small nociceptive neurons. Science 270:1366-1369.

Taft RJ, Pheasant M, Mattick JS (2007) The relationship between non-protein-coding DNA and eukaryotic complexity. Bioessays 29:288-299.

Tai HC, Schuman EM (2008) Ubiquitin, the proteasome and protein degradation in neuronal function and dysfunction. Nat Rev Neurosci 9:826-838.

Takahashi M, Seagar MJ, Jones JF, Reber BF, Catterall WA (1987) Subunit structure of dihydropyridine-sensitive calcium channels from skeletal muscle. Proc Natl Acad Sci U S A 84:5478-5482.

Tedford HW, Zamponi GW (2006) Direct G protein modulation of Cav2 calcium channels. Pharmacol Rev 58:837-862.

Thaler C, Gray AC, Lipscombe D (2004) Cumulative inactivation of N-type CaV2.2 calcium channels modified by alternative splicing. Proc Natl Acad Sci U S A 101:5675-5679.

Turkel N, Aydin R, Ozer U (1999) Stabilities of complexes of Scandium(III) and Yttrium(III) with salicylic acid. Turk J Chem 23:249-256.

Ule J, Darnell RB (2006) RNA binding proteins and the regulation of neuronal synaptic plasticity. Curr Opin Neurobiol 16:102-110.

Voges D, Zwickl P, Baumeister W (1999) The 26S proteasome: A molecular machine designed for controlled proteolysis. Annual Review of Biochemistry 68:1015-1068.

von Zastrow M, Svingos A, Haberstock-Debic H, Evans C (2003) Regulated endocytosis of opioid receptors: cellular mechanisms and proposed roles in physiological adaptation to opiate drugs. Curr Opin Neurobiol 13:348-353.

Wahl MC, Will CL, Luhrmann R (2009) The spliceosome: design principles of a dynamic RNP machine. Cell 136:701-718.

Waithe D, Ferron L, Page KM, Chaggar K, Dolphin AC (2011) {beta}-subunits promote the expression of Cav2.2 channels by reducing their proteasomal degradation. J Biol Chem.

Waldhoer M, Bartlett SE, Whistler JL (2004) Opioid receptors. Annu Rev Biochem 73:953-990.

Wang YX, Pettus M, Gao D, Phillips C, Scott Bowersox S (2000) Effects of intrathecal administration of ziconotide, a selective neuronal N-type calcium channel blocker, on mechanical allodynia and heat hyperalgesia in a rat model of postoperative pain. Pain 84:151-158.

Williams JT, Christie MJ, Manzoni O (2001) Cellular and synaptic adaptations mediating opioid dependence. Physiol Rev 81:299-343.

Wilson SG, Mogil JS (2001) Measuring pain in the (knockout) mouse: big challenges in a small mammal. Behav Brain Res 125:65-73.

Worle-Knirsch JM, Pulskamp K, Krug HF (2006) Oops they did it again! Carbon nanotubes hoax scientists in viability assays. Nano Lett 6:1261-1268.

Xie J, Black DL (2001) A CaMK IV responsive RNA element mediates depolarization-induced alternative splicing of ion channels. Nature 410:936-939.

Xu P, Duong DM, Seyfried NT, Cheng D, Xie Y, Robert J, Rush J, Hochstrasser M, Finley D, Peng J (2009) Quantitative proteomics reveals the function of unconventional ubiquitin chains in proteasomal degradation. Cell 137:133-145.

Xu W, Lipscombe D (2001) Neuronal Ca(V)1.3alpha(1) L-type channels activate at relatively hyperpolarized membrane potentials and are incompletely inhibited by dihydropyridines. J Neurosci 21:5944-5951.

Yan AH, Xiao XC, Kulaots I, Sheldon BW, Hurt RH (2006) Controlling water contact angle on carbon surfaces from 5 degrees to 167 degrees. Carbon 44:3116-3120.

Yi JJ, Ehlers MD (2005) Ubiquitin and protein turnover in synapse function. Neuron 47:629-632.

Yi JJ, Ehlers MD (2007) Emerging roles for ubiquitin and protein degradation in neuronal function. Pharmacol Rev 59:14-39.

Yokoyama CT, Myers SJ, Fu J, Mockus SM, Scheuer T, Catterall WA (2005) Mechanism of SNARE protein binding and regulation of Cav2 channels by phosphorylation of the synaptic protein interaction site. Mol Cell Neurosci 28:1-17.

Zhang C, Zhang Z, Castle J, Sun S, Johnson J, Krainer AR, Zhang MQ (2008) Defining the regulatory network of the tissue-specific splicing factors Fox-1 and Fox-2. Genes Dev 22:2550-2563.

Zhong X, Liu JR, Kyle JW, Hanck DA, Agnew WS (2006) A profile of alternative RNA splicing and transcript variation of CACNA1H, a human T-channel gene candidate for idiopathic generalized epilepsies. Hum Mol Genet 15:1497-1512.

Zhu Y, Ikeda SR (1994) VIP inhibits N-type Ca2+ channels of sympathetic neurons via a pertussis toxin-insensitive but cholera toxin-sensitive pathway. Neuron 13:657-669.

Zotova TV, Arslanov VV, Gagina IA (1998) Monolayers and Langmuir-Blodgett films of yttrium stearate. Thin Solid Films 326:223-226.